NANOSCALE PROPERTIES OF COMPLEX OXIDE FILMS

Cover: two x-ray photoemission diffraction figures. The filled contour plot is a simulation of the Cu $2p_{\frac{3}{2}}$ intensity variation as a function of the angle between the sample surface normal and the electron detector of a tetragonal CuO thin film. The contour lines behind the first figure are of a measurement of such a sample. More information on these figures can be found in chapter 5.

Committee members:

Chairman:	prof. dr. W.H.M. Zijm	University of Twente
Supervisors:	prof. dr. ing. D.H.A. Blank	University of Twente
	prof. dr. M.R. Beasley	Stanford University
Assistant-supervisor:	dr. ir. G. Koster	University of Twente
Members:	prof. dr. T.H. Geballe	Stanford University
	prof. dr. T. Claeson	Chalmers University
	prof. dr. T.T.M. Palstra	University of Groningen
	prof. dr. ir. H.J.W. Zandvliet	University of Twente
	prof. dr. ir. H. Hilgenkamp	University of Twente

The work described in this thesis was performed at the Geballe Laboratory for Advanced Materials at Stanford University, Stanford, CA, United States of America.

Funding for this work was provided by NanoNed, EPRI, and DOE BES.

Nanoscale properties of complex oxide films

PhD Thesis, University of Twente
ISBN/EAN: 978-90-365-2639-5
Printed by PrintPartners Ipskamp, Enschede

NANOSCALE PROPERTIES OF COMPLEX OXIDE FILMS

PROEFSCHRIFT

ter verkrijging van
de graad van doctor aan de Universiteit Twente,
op gezag van de rector magnificus,
prof. dr. W.H.M. Zijm,
volgerns besluit van het College voor Promoties
in het openbaar te verdedigen
op donderdag 17 april 2008 om 13.15 uur

door

Wolter Siemons

geboren op 28 april 1980
te Sneek

Dit proefschrift is goedgekeurd door:

Promotoren:	prof. dr. ing. D.H.A. Blank
	prof. dr. M.R. Beasley
Assistent-promotor:	dr. ir. G. Koster

For Charles, Reini, Arnout, and Liseth

We shall not cease from exploration and the end of all our exploring will be to arrive where we started... and know the place for the first time. — T.S. Eliot

Abstract

As miniaturization continues, layers in devices are made thinner and their properties become increasingly difficult to measure. There are techniques available to measure a wide range of properties of materials at nanometer length scales and measure the extremely small signals that they produce. This thesis focusses on the use of such techniques to measure structural, stoichiometric, and magnetic properties of samples. Three different material systems will be presented, each of which zooms in on a different aspect of analysis. Their commonality is that they are oxide materials and are all in thin film form deposited on an oxide substrate.

The first system is the hetero-interface between two nominal insulators, $SrTiO_3$ and $LaAlO_3$. At this interface a conducting electron layer exists. The TiO_2/LaO interface between $SrTiO_3$ and $LaAlO_3$ has a sheet carrier density of $\sim 10^{17}$ electrons/cm^2 and a mobility of 10^4 cm^2 V^{-1} s^{-1}, as inferred from conductivity and Hall-effect measurements; each of these is strikingly large. The origin of the conductivity is not clear, but is suggestive of a very interesting charge transfer system due to valence mismatch of insulators.

We show the magnitude of the sheet density and the mobility of the electrons are sensitive functions of the deposition conditions in ways that suggest that the origin of this large sheet charge density is oxygen vacancies (donating electrons) in the $SrTiO_3$ substrate. Further, we argue that these vacancies are introduced by the pulsed laser deposition (PLD) process, which is used to create the interface.

Ultraviolet photoelectron spectroscopy (UPS) spectra show states at the Fermi level, indicating a conducting interface. The number of these states is lowered when the sample is oxidized, insinuating oxygen vacancies play an essential role in supplying the charge carriers. This is further confirmed by near edge x-ray absorption spectroscopy (NEXAS) and visible to vacuum UV-spectroscopic ellipsometry (vis-VUV-SE) measurements which show more Ti^{3+} for samples made at lower pressures. We argue that the vacancies are created by the PLD process itself where relatively high energy particles sputter off oxygen. To reduce the number of vacancies we have annealed samples in atomic oxygen, which reduces the number of carriers, but keeps their mobility the same.

The location of the charge carriers changes dramatically as a function of temperature. We calculate the potential and the carrier density in the $SrTiO_3$ to determine where the electrons are located as a function of distance from the interface. We also calculate the electrons move into the pristine $SrTiO_3$ over large distances mainly due

to the high dielectric constant of $SrTiO_3$ at low temperatures.

Besides this interface we also examined the interface between $LaTiO_3$ and $SrTiO_3$ where in addition to conductivity magnetic effects have been predicted. The magnetic measurements prove the interaction between the two materials is less than would be expected based on some of the theoretical predictions. On the contrary, the $LaTiO_3$ seems to retain its antiferromagnetism even though it is just one monolayer thick. The transition temperature is suppressed for such thin layers, probably due to a finite size effect.

The second system consists of $SrRuO_3$ thin films. We study the crystal structure of the material at elevated temperatures to determine the symmetry of the unit cell during epitaxial growth on a $SrTiO_3$ substrate in order to explain the existence of untwinned $SrRuO_3$ films. The results of the high temperature x-ray diffraction (XRD) measurements unambiguously demonstrate that a $SrRuO_3$ (110) layer grown coherently on $SrTiO_3$ (001) substrate does not undergo a tetragonal to cubic transition and remains tetragonal at temperatures up to 730 °C. The tetragonal unit cell allows us to explain single domain growth of $SrRuO_3$ films on miscut $SrTiO_3$ substrates. In step flow growth mode, growing species tend to attach to the steps due to the larger diffusion length as compared to the terrace length of the substrate. For a tetragonal unit cell where $c > a = b$, $SrRuO_3$ will tend to align its c-axis along the steps. If the step edges run only along $SrTiO_3$ [100] or [010] directions then a single domain $SrRuO_3$ layer is formed. On the other hand, if the step edges run along a direction rotated by some angle from [100] or [010] directions, $SrRuO_3$ will attach to steps with its longer unit cell axis parallel to the steps resulting in twinned structure due to the serrated nature of the step edge. $SrRuO_3$ layers on substrates with low miscut angles exhibit twinned structures due to large length of the substrate terraces as compared to the diffusion length of $SrRuO_3$, which results in island growth. In this regime $SrRuO_3$ tetragonal unit cell tends to align randomly along [100] and [010] directions of the $SrTiO_3$ substrate.

We further show that we can grow $SrRuO_3$ thin films on $SrTiO_3$ under various conditions and that this material exhibits a range of properties, due to a subtle change in stoichiometry on the ruthenium site, related to the oxidation conditions during deposition. Resistivity, XRD, UPS and x-ray photoemission spectroscopy (XPS) experiments all seem to indicate that this change in behavior is due to a changing electron-electron correlation, although we also point out that contributions from inelastic processes at vacancy sites as well as surface states cannot be ignored. These results shed light on the well-known sensitivity of the properties of $SrRuO_3$ to its synthesis conditions. Equally important, they suggest a clear path to more quantitative comparisons with theory.

We have analyzed magnetism in ultrathin films of $SrRuO_3$ as well and show that itinerancy and ferromagnetism disappear at a critical film thickness between 3 and 4 monolayers. While a metal-insulator transition could also happen if there are subtle rotations of the oxygen octahedra rendering the unit cell symmetry tetragonal or even cubic for extremely thin films, this cannot be the case for our fully strained films since the observed MIT is abrupt while strained films will relieve the strain gradually with increasing thickness. A strong deviation from thick films behavior that onsets around 9 unit cells may either indicate a 2D to 3D transition, or a change in the order of the

transition to the ferromagnetic state. At that thickness transport is 2D dominated with a weak localization increase in the resistance at low temperatures.

The third and final system is CuO. Because of its relative simplicity, CuO is a candidate compound to study electron correlation effects and the influence of correlation on the electronic structure of transition metal compounds, in particular high temperature cuprate superconductors. To create such a model system CuO needs to be grown in a rock salt structure, which is not a stable structure in bulk copper oxide (normally CuO forms a monoclinic structure).

We grow CuO with a higher degree of symmetry by using epitaxial stabilization on a $SrTiO_3$ substrate. The in-plane lattice parameters are determined by reflection high energy electron diffraction (RHEED). After taking forbidden reflections into account the CuO is found to grow cube-on-cube on the $SrTiO_3$, which results in an in-plane lattice parameter of 3.905 Å for CuO. The out-of-plane lattice parameter is measured with x-ray photoemission diffraction (XPD) and decided to be about 5.3 Å after comparing to simulated data. The unit cell on $SrTiO_3$ is highly strained and for this reason the tetragonal CuO cannot grow coherently for more than a few nm.

The electronic structure of the tetragonal phase of CuO is found to be different from the monoclinic phase by examining the Cu $2p$ core level structure. The main peak becomes broader and the satellite peak sharper when the tetragonal phase is formed. The intensity distribution in the satellite peak shifts more to lower binding energies. Our measurements suggest that the screening electrons are more delocalized in the tetragonal structure. Using models from literature we can conclude the degree of hybridization is weaker in the tetragonal structure than in tenorite. In other words, the ionicity is stronger in the tetragonal structure than in the monoclinic one. The UPS valence band spectrum of tetragonal CuO is very similar to that measured for tenorite.

The magnetic properties are studied by measuring the exchange bias effect on a very limited number of samples with an interface of CuO and $SrRuO_3$. Instead of increased coercivity and a shifted hysteresis loop, we observe a decrease in coercivity for part of the spins, no shift in the hysteresis loop, and a reduction in magnetic signal in general after deposition of the CuO.

We attempt to dope the tetragonal CuO by depositing alkali metals on top, which might transfer an electron to the CuO. Li and Cs were tried and showed similar results. In both cases the Cu $2p$ XPS spectrum changed from Cu^{2+} to a Cu^{1+}, suggesting either a direct doping of electrons by the alkali metal or oxygen reduction in the CuO due to the metal. In both cases the CuO would be electron doped. The question remains whether the doped electrons are localized or mobile.

Samenvatting

Wanneer lagen extreem dun zijn, is het lastig om de eigenschappen nauwkeurig te meten. Er zijn echter technieken beschikbaar om een breed scala aan eigenschappen te meten op de nanometerschaal die gevoelig genoeg zijn om de extreem kleine signalen te meten. Dit proefschrift richt zich op het gebruik van zulke technieken om structurele, stoichiometrische en magnetische eigenschappen van extreem dunne lagen te bepalen. Drie verschillende materiaal systemen worden beschouwd en elk systeem belicht verschillende technieken. Alle drie de systemen hebben als gemeenschappelijk kenmerk dat het oxidische materialen betreft die in dunne film vorm gedeponeerd worden op een oxidisch substraat.

Het eerste systeem bestaat uit het grensvlak tussen twee materialen die van nature isolerend zijn, $SrTiO_3$ en $LaAlO_3$. Wanneer de twee materialen met elkaar in contact worden gebracht ontstaat er een geleidende laag aan dit grensvlak. Het TiO_2/LaO grensvlak tussen $SrTiO_3$ en $LaAlO_3$ heeft een 2D ladingsdragerdichtheid van $\sim 10^{17}$ electronen/cm^2 en een electron mobiliteit van 10^4 cm^2 V^{-1} s^{-1}, berekend uit weerstand en Hall metingen; beide waardes zijn opmerkelijk hoog. De oorsprong van de geleiding is niet duidelijk, maar suggereert dat een interessant ladingsoverdracht systeem aanwezig is doordat de valenties van de twee materialen niet overeenkomt.

Wij laten zien dat de grootte van de 2D ladingsdragerdichtheid en de mobiliteit van de elektronen een functie is van de depositie condities en dat dit er op wijst dat zuurstof vacatures (elk missend zuurstof atoom doneert 2 elektronen) de oorzaak zijn van de geleiding in het $SrTiO_3$ substraat. Verder beargumenteren wij dat deze vacatures geïntroduceerd worden door het gepulste laser depositie proces (PLD) dat gebruikt wordt om de lagen te maken.

Ultraviolet foto-emissie spectroscopie (UPS) laat zien dat er toestanden zijn aan het Fermi niveau, wat er op duidt dat het grensvlak geleidend is. Het aantal toestanden wordt minder als het grensvlak wordt blootgesteld aan zuurstof, wat insinueert dat zuurstof vacatures een belangrijke rol spelen bij het ontstaan van de ladingsdragers. Dit wordt bevestigd door röntgen absorptie spectroscopie (NEXAS) en spectroscopische ellipsometrie (vis-VUV-SE) metingen die laten zien dat er meer Ti^{3+} aanwezig is voor grensvlakken gemaakt bij lagere zuurstof drukken. Wij stellen dat de vacatures veroorzaakt worden door het PLD proces zelf doordat hoog energetische deeltjes zuurstof uit het substraat sputteren. Om het aantal zuurstof vacatures te verminderen hebben wij de grensvlakken aan atomair zuurstof blootgesteld, wat het aantal ladingsdragers vermindert, maar hun mobiliteit hetzelfde houdt.

De locatie van de ladingsdragers is zeer afhankelijk van de temperatuur. Wij berekenen de potentiaal en de ladingsdragerdichtheid in het $SrTiO_3$, om te bepalen waar de elektronen zich bevinden, als functie van de afstand van het grensvlak. Wij vinden dat de elektronen zich over grote afstanden verplaatsen in het $SrTiO_3$ en dat dit vooral veroorzaakt wordt door de hoge dielektrische constante van $SrTiO_3$ bij lage temperaturen.

Naast dit grensvlak hebben wij ook het grensvlak tussen $LaTiO_3$ en $SrTiO_3$ bestudeerd, waar naast geleiding ook magnetische effecten zijn voorspeld. De magnetische metingen tonen aan dat de interactie tussen de twee materialen minder groot is dan verwacht gebaseerd op theoretische voorspellingen. In tegendeel, het $LaTiO_3$ blijft antiferromagnetisch zelfs als het slechts één eenheidscel dik is, hoewel de transitietemperatuur wel onderdrukt wordt.

Het tweede materiaal systeem bestaat uit dunne lagen van $SrRuO_3$. Wij bestuderen de kristal structuur van het materiaal bij hoge temperaturen, om zo de symmetrie van de eenheidscel te bepalen tijdens de epitaxiale groei van $SrRuO_3$ op een substraat van $SrTiO_3$ en daarmee te verklaren hoe $SrRuO_3$ films geen tweelingkristal vormen. De resultaten van de röntgen diffractie experimenten bij hoge temperatuur laten zien dat een $SrRuO_3$ (110) laag gegroeid op $SrTiO_3$ niet een structurele fase overgang ondergaat van een tetragonale naar een kubische structuur bij een temperatuur lager dan 730 °C. De tetragonale eenheidscel verklaart de groei in een enkel domein op $SrTiO_3$, afhankelijk van de terrasgrootte op het $SrTiO_3$ oppervlak. In *step flow* groei zullen de atomen, die aan het oppervlak komen tijdens de groei zich hechten aan de stapranden, omdat de diffusie lengte groter is dan de lengte van de terrassen. Voor een tetragonale eenheidscel waarbij $c > a = b$, zal zich zo oriënteren dat de langere c-as parallel ligt aan de stapranden. Als de stapranden alleen langs de $SrTiO_3$ [100] of [010] richtingen lopen dan zal een $SrRuO_3$ laag gevormd worden met een enkele oriëntatie. Wanneer echter de stapranden in een willekeurige richting lopen dan zal een tweelingkristal ontstaan doordat de staprand gekarteld is. Aan de andere kant, als de terrassen groter zijn dan de diffusielengte van $SrRuO_3$ dan zal de groei plaatsvinden in de vorm van eilanden. Tijdens de groei kan de $SrRuO_3$ eenheidscel zich willekeurig oriënteren langs de [100] of [010] richtingen op het substraat en dit resulteert in de formatie van een tweelingkristal.

Verder laten wij zien dat wij dunne lagen van $SrRuO_3$ op $SrTiO_3$ kunnen groeien onder verschillende omstandigheden en dat wij de eigenschappen van het materiaal kunnen beïnvloeden door de oxidatie condities tijdens depositie te veranderen, wat resulteert een subtiele verandering van de ruthenium stoichiometrie in de lagen. Röntgen diffractie, foto-emissie spectroscopie en weerstandsmetingen wijzen er allemaal op dat de veranderingen in de eigenschappen te maken hebben met veranderende correlatie tussen de elektronen. Wij wijzen er echter op dat inelastische processen op de plaats van de ruthenium vacatures ook een belangrijke rol kunnen spelen. Deze resultaten verklaren waarom de eigenschappen van $SrRuO_3$ zo afhankelijk zijn van de groeiomstandigheden. Ook suggereren ze een manier om experimentele resultaten op een meer kwantitatieve wijze met theoretische berekeningen te vergelijken.

Ook hebben wij magnetisme in ultradunne lagen van $SrRuO_3$ geanalyseerd en wij laten zien dat ferromagnetisme en transport verdwijnt bij een kritische filmdikte tussen

3 en 4 eenheidscellen. Een sterke afwijking van het gedrag van dikke lagen treedt op bij een dikte van 9 eehheidscellen, wat er op kan duiden dat een transitie van 2D naar 3D plaats vindt of een verandering in de orde van de transitie naar de ferromagnetische toestand. Bij die dikte zijn de elektrische transport eigenschappen 2D met een toename van de weerstand bij lage temperaturen door zwakke localisatie.

Het derde en laatste systeem is CuO. Omdat dit een relatief eenvoudig systeem is, is CuO een goed materiaal om elektron correlatie in te bestuderen, evenals de invloed van deze correlatie op de elektronische eigenschappen van transitie metaal verbindingen, in het bijzonder hoge temperatuur supergeleiders. Om CuO te gebruiken als een model systeem, is het van belang om het in een NaCl structuur te groeien, wat een structuur is die in de natuur niet voorkomt (CuO vormt normaal een monokliene eenheidscel).

Wij groeien CuO met een tetragonale eenheidscel door gebruik te maken van epitaxiale stabilisatie op een $SrTiO_3$ substraat. De roosterconstanten van de nieuwe fase in het vlak van het substraat zijn bepaald met reflectie hoge energie elektronen diffractie (RHEED) en, nadat verboden reflecties in beschouwing zijn genomen, blijkt dat het rooster van CuO precies samenvalt met dat van $SrTiO_3$ en dus zijn roosterconstanten van de a en b richtingen 3.905 Å. Om de roosterconstante te bepalen in de richting loodrecht op het substraat is er gebruik gemaakt van röntgen foto-emissie diffractie (XPD) en door te vergelijken met gesimuleerde data is vastgesteld dat deze ongeveer 5.3 Å is. De eenheidscel op $SrTiO_3$ staat onder grote spanning en hierdoor kunnen lagen van de tetragonale fase slechts gegroeid worden tot een dikte van enkele nanometers.

Wij vinden dat de elektronische structuur van het tetragonale CuO verschilt van die van de monokliene structuur door het spectrum van het Cu $2p$ niveau te meten. De hoofdpiek is breder en de satellietpiek scherper voor de tetragonale fase. De distributie van de intensiteit in de satellietpiek schuift naar lagere energieën. Onze metingen suggereren dat de elektronen die de lading op de Cu afschermen minder gelokaliseerd zijn in de tetragonale structuur. Door gebruik te maken van modellen kunnen wij concluderen dat hybridisatie een minder belangrijke rol speelt in tetragonaal CuO. Met andere woorden, de tetragonale structuur gedraagt zich meer ionisch. Het valentie spectrum van de tetragonale fase, zoals gemeten met UPS, lijkt wel zeer sterk op het spectrum van de monokliene fase.

De magnetische eigenschappen worden gemeten door te kijken naar de interactie aan het grensvlak van het waarschijnlijk antiferromagnetische CuO en het ferromagnetische $SrRuO_3$. In plaats van een toename van het coërcitieveld en een verschuiving in de hystereselus, nemen wij een afname van het coërcitieveld voor een gedeelte van de spins, geen verschuiving in de hystereselus en een afname van magnetisch signaal in het algemeen, waar.

Wij proberen het tetragonale CuO te dopen door alkalimetalen te deponeren op het oppervlak, welke mogelijk een elektron zullen overdragen aan het CuO. Li en Cs zijn beide gebruikt en laten gelijke resultaten zien. In beide gevallen verandert het Cu $2p$ XPS spectrum van Cu^{2+} naar Cu^{1+}, wat kan duiden op directe doping van elektronen of de creatie van zuurstof vacatures in het CuO. Beide scenario's leiden tot elektron doping van het CuO, maar het is niet bekend of de elektronen mobiel of gelokaliseerd zijn.

Preface

In 2004 I was awarded the opportunity to conduct the research towards a PhD at Stanford University in Palo Alto, California. I had completed my internship at Stanford in 2002–2003. I welcomed this opportunity to return and as I look back I see I made the right decision. My dissertation, the product of my three years of research at the Geballe Laboratory for Advanced Materials at Stanford University, will be submitted to the University of Twente in order to receive my Doctor of Philosophy in Materials Science.

This thesis is a collection of topics that gives an impression of the processes to measure material properties on very small length scales and with very small signals. This is done by looking at different materials systems of which structural, magnetic, and electronic properties are determined through a range of techniques.

This is not by far the only thesis to focus on this subject. But instead of focussing on one subject or one piece of equipment, this thesis offers a wider range of techniques and approaches the challenges from the point of view of the sample grower. I hope those who read this thesis get a better understanding of the possibilities to measure films at the nanoscale.

Wolter Siemons, March 24, 2008

Acknowledgements

No work of this magnitude is completed without support and a great number of people deserve my gratitude. I cannot thank everyone who has crossed my path in the last years, instead I will focus on those people who have had the greatest impact on the contents and completion of this thesis.

First of all I need to thank Gertjan Koster who contributed significantly to the research for this thesis both through help with experiments, as well as writing the results in the form of papers, and he has kindly read the manuscript for the thesis. Besides the scientific side he, his wife Mirije, and their daughter Jenna have made my stay in the Bay Area truly worthwhile.

Next I need to thank my advisors: Mac Beasley and Dave Blank. Mac has been invaluable as my day-to-day advisor to steer the work in the right direction and placing it in a broader context. Further, he has been a big help in the writing of this thesis due to his uncanny ability to transform scientific writing into beautiful prose. Dave deserves credit for providing me the opportunity to go abroad for my PhD work and for the valuable discussions of the work.

I have also had the benefit of considerable discussion and interaction with Ted Geballe and Guus Rijnders. Ted's knowledge of materials and his continuous stream of new ideas stimulate any researcher. The discussions I have had with Guus over the years have been valuable and I would like to thank him for supporting my stay at Stanford.

Further, I need to thank all the people who have contributed to the publication of the work: Robert Hammond for all the help he has provided in the lab; Hideki Yamamoto who worked in the laboratory as a visiting researcher when I arrived and whose expertise of MBE has been a great help; Gerry Lucovsky and Hyungtak Seo from North Carolina State University for the NEXAS and ellipsometry measurements he performed on the $LaAlO_3/SrTiO_3$ interfaces; Aharon Kapitulnik and Jing Xia for performing magneto-optical Kerr effect measurements on various samples with their Sagnac interferometer; Myles Steiner for his low temperature measurements on MgB_2; Jim Reiner for the samples he left behind; Arturas Vailionis for the XRD measurements on the ruthenates; Walter Harrison for pontificating about electronic structures at the right moments.

I should like to express my gratitude to Mike Kelly and Chuck Hitzman for providing me the opportunity to help out at the surface science laboratory at the Stanford Nanocharacterization Laboratory. I have enjoyed working with you and all the students

that have passed through during the last years and have learned a lot about teaching and maintaining equipment.

None of this work is possible without the support of a good administrative staff. I specifically wish to thank Cyndi, Angela, Larry, Droni, and Mark at Stanford and Marion at Twente.

I am grateful for the support I have received from the students within the KGB group either in the form of help with experiments or equipment or simply because of their contribution to the good atmosphere in the group.

Outside of academia I owe much to Joni Reid who has shared her home with me and has been my friend and source of entertainment. She has contributed to this thesis by proof reading all the text.

Finally, I need to thank my family for their relentless support during the years I was halfway across the planet: Charles, Reini, Arnout, and Liseth, thank you!

Contents

Chapter 1

Micro gone, going nano

Remember the time when everything was micro? It was not that long ago that our detergents, facial creams, food, and practically everything else was infested with micro this and that. And now we have apparently advanced another three orders of magnitude in scaling things, because the nano-age is upon us.

The word *micro* comes from micrometer (μm), which is a millionth of a meter, and *nano* comes from nanometer (nm), which is a billionth of a meter. For comparison, a human hair is about 100 μm in diameter and it grows at a rate of about 5 nm/sec. A nm is the distance of about 10 hydrogen atoms in a row. Manufacturers have figured out that nano has a nice ring to it and are now prolifically applying it left and right. The Woodrow Wilson Center's Project on Emerging Nanotechnologies[1] keeps a list of products that claim to use nanotechnology. The list is becoming quite substantial and contains lots of products which might surprise you. It ranges from the Corsa Nanotech Ice Axe (with Nanoflex steel) to the well-known iPod Nano, which uses semiconductor manufacturing methods with precision below 100 nm, all the way to Zelens' Fullerene C-60 Day Cream, which encourages us to smear buckyballs (60 carbon atoms arranged in a spherical shape, often compared to a soccer ball) onto our face every morning.

It may seem a lot like a hype, but this is hardly the first of such hyped industries: in the early 1960's a lot of companies put -tron or -tronic in their names, which guaranteed success with investors at Wall Street. Most of those companies no longer exist and many people lost a lot of money when that bubble burst. This thesis of course does not deal with the economic impact of such bubbles, but during this time money flows to research in nanotechnology since nobody wants to be left behind. Governments steer a lot of funds toward universities in the form of nano-initiatives such as NanoNed, a Dutch initiative which supports the research described in this thesis. The aim of this chapter is to show how this work fits in the realm of nanotechnology.

The idea of nanotechnology goes back to a talk given by physicist Richard Feynman in 1959 at a meeting of the American Physical Society at Caltech. The title of the talk was *There's plenty of room at the bottom*,[2] in which he described how the manipulation of single atoms or molecules might be accomplished. The term nanotechnology was

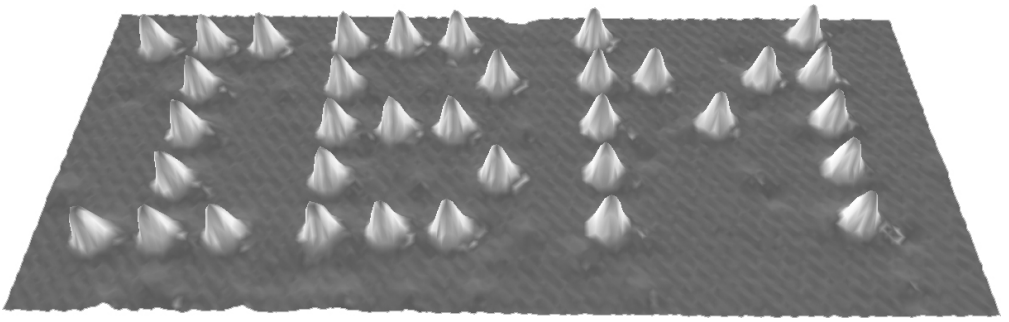

Figure 1.1: *The arrangement of xenon atoms on a nickel surface by Eigler and Schweizer*[4] *at IBM in 1989 demonstrating control over single atoms.*

coined later by Nario Taniguchi in a 1974 paper titled *On the basic concept of nano-technology.*[3] Even though Feynman presented a clear roadmap, it would not be until the late 80's before his vision was realized: in 1989 scientists at IBM spelled out the name of the company with xenon atoms on nickel,[4] as shown in figure 1.1. This was a major accomplishment. Even now this form of nanotechnology requires a great investment of both money and time to make even the simplest devices.

The generally accepted definition of nanotechnology is only that the sample or device requires control of matter on a scale smaller than 1 μm. This is surprising, because it means nanotechnology has been used for a long time, but has never been recognized as such. For example, the vulcanization of rubber in the 19$^{\text{th}}$ century, where sulfur bonds the individual polymer molecules to form a harder, more durable compound demonstrated very small links and should, by all means, count as nanotechnology; but have never been identified as such. If we go back even further we find that we have been able to make layers thinner than 1 μm for a very long time, such as the craft of gold beating, which has been practiced since the age of the Egyptians as is evident from the beautiful art created during that period. Moreover, there are written records dating back to Greek and Roman times containing precise recipes for making the best leafs of gold.[5,6,7] In those days the limit to which the gold could be thinned was about 0.3 μm (or 300 nm), which would be counted as nanotechnology today. Currently, gold can be machine beaten to about 100 nm and very skilled craftsmen can beat it to 50 nm. Art was not the only beneficiary of the advancement of gold beating technology, it fueled the measurement of new physics as well. One of the most famous of these experiments is by Rutherford with Geiger and Marsden in 1909,[8,9] where a very thin gold foil was used to determine the structure of an atom. To this end they bombarded the gold foil with α particles and expected the particles would not be affected much by the gold foil, since they viewed atoms as a homogeneous cloud. What they measured was that indeed most of the particles were not deflected, but some were deflected significantly and a very small fraction even bounced back in the direction of the incoming beam. This was how they disproved the Thomson model of the atom and laid the groundwork for what was going to be the Bohr model of the atom.[10,11,12]

Since the 1940's we have had vacuum technology and thin film deposition techniques that can deposit layers which are even thinner than the gold foil in a very accurate way. In addition tools are available that can monitor the growth of these layers as they happen, such as reflection high energy electron diffraction, and materials systems can therefore be constructed on the scale of nanometers as if we were playing with Lego blocks of only a few atoms in size. This perfect control to create clean materials systems has led to the discovery of new effects. For example Norton *et al.*[13] stabilized $SrCuO_2$ and $BaCuO_2$ superlattices and found superconductivity in the new compounds at temperatures up to 70 K.

Since we have been able to make features in a controlled way smaller than 100 nm and to manipulate the properties of materials at small length scales for such a long time, what makes this the nano-age? The answer lies in measuring such materials, rather than fabricating them. For the first time in history there are techniques available to measure the properties of materials at nanometer length scales and measure the extremely small signals that they produce. In this thesis we will use such techniques to measure structural, stoichiometric, and magnetic properties of samples. Three different material systems will be presented, each of which zooms in on a different aspect of analysis. Their commonality is that they are oxide materials and are all in thin film form deposited on an oxide substrate.

In chapter 3 on page 27 we study the interface between different oxide compounds. First we look at the interface between $LaAlO_3$ and $SrTiO_3$, two materials that are bulk insulators, but form a conducting layer at the interface between them.[14,15] We show that the deposition method itself contributes to the creation of charge carriers at the interface by investigating the properties of the interface with a wide range of techniques, most importantly transport measurements and photoemission spectroscopy of the interface. We then turn to an interface between two other materials: $LaTiO_3$ and $SrTiO_3$, for which ferromagnetic effects are predicted in literature even though neither of them is ferromagnetic. We determine the magnetic properties of the interfaces by measuring the Kerr effect as in chapter 4 for $SrRuO_3$ layers.

In chapter 4 on page 49 we discuss $SrRuO_3$. The first part of that chapter deals with the crystal structure of $SrRuO_3$ at high temperatures and offers clear explanation of the twinning behavior in such films, which is determined in the first few monolayers of growth. In the second part we look at how slight off-stoichiometries on the ruthenium site influence the electron correlation in this material and how this correlates with photoemission spectroscopy and transport measurements. The third and final part of chapter 4 is about magnetic measurements on very thin layers (below 10 monolayers) of $SrRuO_3$. Due to recent advances in magneto-optical Kerr effect measurements[16] we are now able to measure the magnetic properties of such layers and show that the magnetic behavior is very much a function of the layer thickness.

Chapter 5 on page 77 contains our efforts to grow CuO with a higher degree of symmetry. CuO normally forms a monoclinic unit cell. We have however succeeded in stabilizing CuO in a tetragonal form by using epitaxial strain by growing on a $SrTiO_3$ substrate. Much of the chapter describes how we were able to determine, with the use of reflection high energy electron diffraction and x-ray photoemission diffraction, that the new phase indeed has a higher degree of symmetry. This was made difficult because

the tetragonal CuO layer was not stable when grown thicker than a few nm and had to be performed *in situ* due to degradation of the sample outside of vacuum. Subsequently the magnetic properties are studied and the attempts to dope the material discussed.

Before we turn to these chapters the experimental details are presented in the next chapter. It contains an overview of the deposition and analysis techniques that were used and a discussion of the substrate treatment that was used for $SrTiO_3$.

Bibliography

1. *Project on emerging nanotechnologies*, Woodrow Wilson International Center for Scholars (2007), URL `http://www.nanotechproject.org`.
2. R. P. Feynman, *There's plenty of room at the bottom*, Lecture at the Meeting of the American Physical Society (1959), URL `http://www.its.caltech.edu/~feynman/plenty.html`.
3. N. Taniguchi, in *Proceedings of the International Conference on Production Engineering* (Japan Society of Precision Engineering, 1974), vol. 2.
4. D. M. Eigler and E. K. Schweizer, Nature **344**, 524 (1990).
5. L. B. Hunt, Gold Bulletin **9**, 24 (1976).
6. O. Vittori, Gold Bulletin **12**, 35 (1979).
7. E. D. Nicholson, Gold Bulletin **12**, 161 (1979).
8. H. Geiger and E. Marsden, Proceedings of the Royal Society A **82**, 495 (1909).
9. E. Rutherford, Philosophical Magazine **21**, 669 (1911).
10. N. Bohr, Philosophical Magazine **26**, 1 (1913).
11. N. Bohr, Philosophical Magazine **26**, 476 (1913).
12. N. Bohr, Philosophical Magazine **26**, 857 (1913).
13. D. P. Norton, B. C. Chakoumakos, J. D. Budai, D. H. Lowndes, B. C. Sales, J. R. Thompson, and D. K. Christen, Science **265**, 2074 (1994).
14. A. Ohtomo and H. Y. Hwang, Nature **427**, 423 (2004).
15. A. Ohtomo and H. Y. Hwang, Nature **441**, 120 (2006).
16. J. Xia, P. T. Beyersdorf, M. M. Fejer, and A. Kapitulnik, Applied Physics Letters **89**, 062508 (2006).

Chapter 2

Sample deposition and characterization

2.1 Introduction

To create and experiment with well-defined thin films three ingredients are needed. First we need a technique to deposit the material; this will be discussed in the first section of this chapter. Second we need a substrate to deposit on and grow the film; for almost all the samples that are discussed in this thesis $SrTiO_3$ was used. It is useful to spend some time going over the details of this material, since its properties are a major influence on the properties of our very thin films. As a matter of fact in many cases we rely on its properties, especially its structural ones, to grow the films in a well defined way. The substrate material is detailed in the second section of this chapter. The third ingredient is measurement techniques that can be used to characterize and determine the physical properties of the film once it is grown. These often serve as a feedback mechanism for the deposition parameters. The last section of this chapter will focus on the different ways such analysis was done.

2.2 Sample deposition

All the samples in this thesis have been grown by either of two deposition techniques: molecular beam epitaxy (MBE) or pulsed laser deposition (PLD). Each of these techniques has its strengths and weaknesses, which are summarized in the sections that follow, together with an overview of the deposition system in general. Both techniques can be used in the deposition system that was used in this work. There is also a second, smaller system in which PLD can be done and which was used to grow the remaining films. An overview of the entire setup is provided in figure 2.1 on the following page. Through the availability of both deposition techniques a wider range of material systems is accessible than with each of the techniques by itself. As we will see in subsequent chapters it also offers more possibilities in single material systems. Not

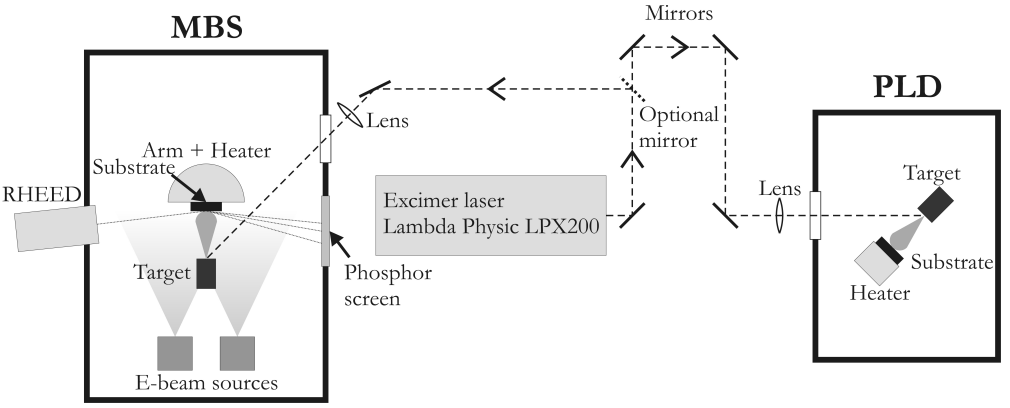

Figure 2.1: *A schematic overview of the entire setup showing how the laser is shared between the two systems.*

all materials are accessible though, such as the alkali metals, and for those elements another technique is presented.

To form oxides with these techniques at low background pressures a special oxygen source is mounted on the system, which has been used for many oxide samples in this thesis, and is addressed separately. This section is concluded by an overview of the deposition conditions used to create the samples that will be discussed in the remaining chapters.

2.2.1 Deposition system

The deposition system, which is schematically presented in figure 2.2 on the next page and called the molecular beam synthesis (MBS) system, consists of three vacuum chambers: the load lock, the deposition chamber, and the analysis chamber. The load lock and the deposition chamber are each pumped with a cryo pump, the analysis chamber is pumped by an ion getter pump. The deposition chamber (base pressure 10^{-9} Torr) is where the samples are made by either MBE or PLD, two techniques that will be discussed in the following sections.

In the main chamber gasses — such as oxygen, argon or nitrogen — can be introduced during the deposition process. Because the system is used for both MBE as well as PLD it is only possible to introduce gasses up to a certain pressure to keep the MBE sources from deteriorating. Typical pressures range from 10^{-6} to 10^{-4} Torr. In order to provide more oxidation power, which is often necessary when working with oxides to ensure a good stoichiometry, an atomic oxygen source is mounted on the system. This provides the opportunity to grow materials that would normally require much higher oxygen pressures to be stable. During growth the film structure and surface morphology are closely monitored with RHEED (see section 2.4.1 on page 17). A residual gas analyzer (RGA) is available to keep a close eye on the composition of the background pressure and outgassing of components.

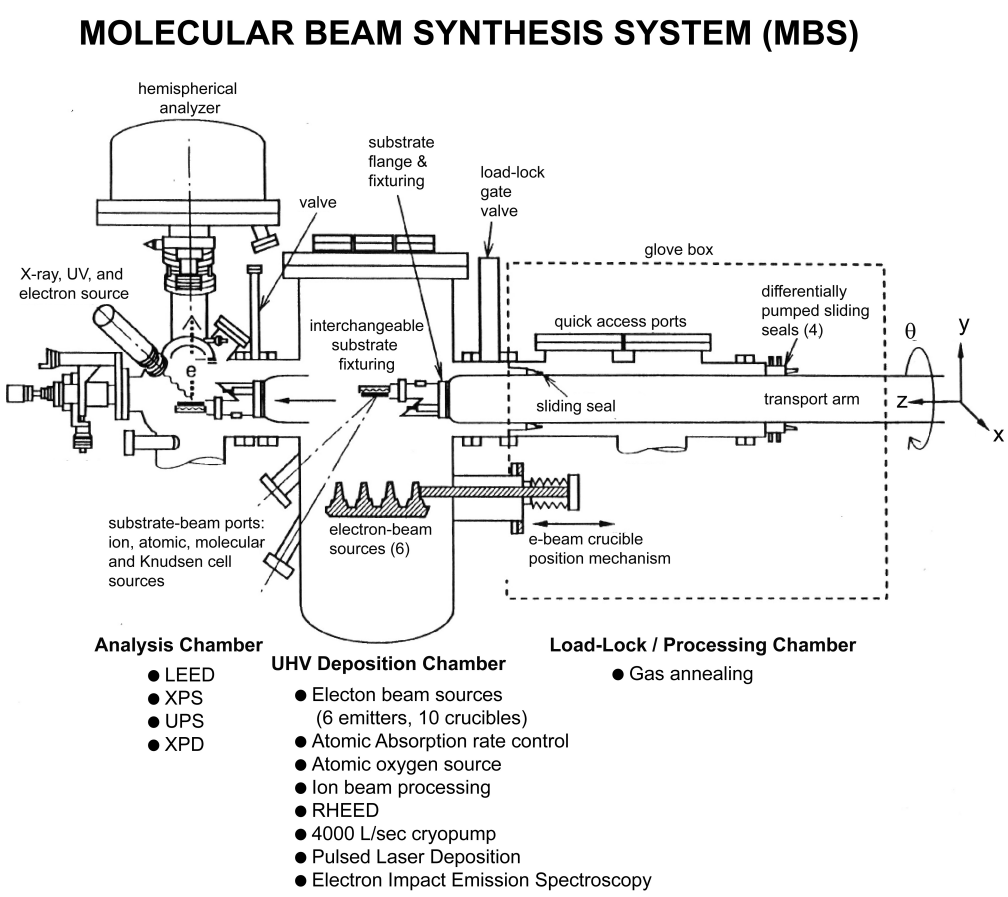

Figure 2.2: *A schematic overview of the deposition system including the main features of every part of the system.*

The analysis chamber (base pressure 10^{-10} Torr) is separated from the deposition chamber in order to maintain as good a vacuum as possible. This is necessary for surface sensitive analysis techniques (such as photoemission spectroscopy, see section 2.4.1 on page 18), which are performed in the analysis chamber.

The sample is moved from chamber to chamber on a long arm. Seals are placed where the arm slides into the load lock. They are differentially pumped to provide minimum leakage at that point. At the end of the arm the sample is gold pasted onto a stainless steal heater block that is heated by two quartz lamps. The arm can be translated in three dimensions and rotated around its long axis (θ). The heater block can be rotated around the axis perpendicular to the surface (φ) so that the sample can be moved into any desired position and orientation. On the arm are also two quartz crystal monitors for MBE rate monitoring. The quartz lamp and quartz crystal housings are water cooled to prevent overheating.

2.2.2 Molecular beam epitaxy

Molecular beam epitaxy (MBE) refers to a deposition technique that uses thermal sources (in our case an electron beam) to evaporate a source material and is the most widely used evaporation technique for making highly pure films. The use of an electron beam allows almost all materials to be evaporated. The material to be evaporated is put into in a crucible, which is then placed in a water cooled copper hearth. Only a small portion of the material is heated to temperatures high enough for the material to evaporate, and the purity of the resulting vapor is therefore only dependent on the purity of the source material and is free of contamination from the crucible or hearth. Our MBS system has 6 electron guns and 10 crucibles to provide enough redundancy when an emitter fails or a crucible is empty. High voltages are provided by a Thermionics SEB-15 power supply, and the current is delivered by Thermionics transformers. For more details regarding MBE consult the book edited by Hill. [1]

In the case of compounds multiple elements are evaporated simultaneously by multiple sources. This offers total control of the stoichiometry within a single compound provided the rate of each element can be controlled accurately. To this end the following rate monitoring techniques were applied for the work described in this thesis: quartz crystal monitors (QCM) and electron impact emission spectroscopy (EIES). QCMs are very easy to use. They measure the mass change on a quartz crystal by monitoring changes in oscillation frequency of the crystal when material is deposited onto it. Complications arise when multiple sources are used at the same time since the QCM cannot distinguish between different elements. In this work QCMs were used only for calibration purposes. For the actual depositions a technique called EIES was used, which is the subject of the next section.

Electron impact emission spectroscopy

For this work the feedback technique that was used for the MBE grown samples deserves a little more attention, since it is different from much-used techniques like atomic absorption or quartz crystal monitor measurements. In electron impact emission spectroscopy the deposition rate is controlled by monitoring the emission of light from the vapor as follows. [2] The vapor flux of materials that are being deposited enters the sensor, which is positioned as close to the sample as possible. In the sensor there is a filament that emits electrons that collide with the vapor flux. The atoms in the vapor flux are brought into an excited state and emit light as they fall back into their ground state. This process is schematically presented in figure 2.3 on the facing page. The wavelength of the light is characteristic of the material that is being deposited. Instead of studying the complete spectrum a strong peak is selected using a band pass filter. The signal is amplified by a photomultiplier and sent to the controller. The controller adjusts the deposition rate with a PID control loop until the desired signal strength is achieved. The signal strength is directly proportional to the flux and is calibrated by comparing to the deposition rate as measured by a QCM on the sample position. The difference between the flux and the deposition rate is determined by the sticking coefficient of the cations. Multiple sources can be monitored with just one sensor by

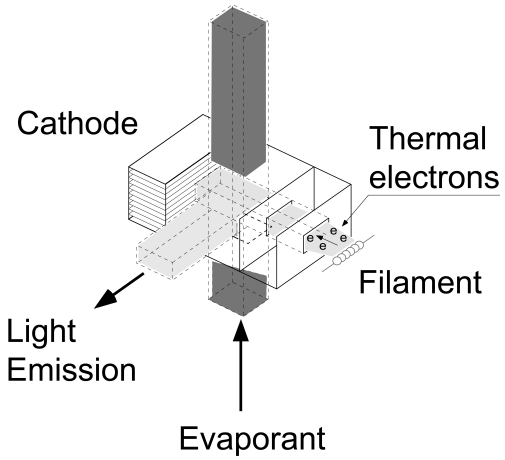

Figure 2.3: *The EIES rate monitoring system consists of a filament (anode), which emits electrons, which in turn excite the atoms in the vapor going by. The light that the excited atoms emit is send to a photomultiplier and translated into a deposition rate. After Lu, Lightner, and Gogol.*[2]

selecting different wavelengths and using multiple photomultipliers to analyze the signals. When using a background gas one of the photomultipliers should be set up to measure the signal coming from the gas, which can be used to eliminate contributions from the background gas to the other photomultipliers. The filters that were available in our system are listed in table 2.1 on the next page.

2.2.3 Pulsed laser deposition (PLD)

Pulsed laser deposition is a thin film deposition technique using a pulsed laser to ablate material from a target. The ablated particles are deposited on a substrate positioned directly across from the target. There are several reasons why PLD is better suited for some applications than MBE. The first is that stoichiometric transfer of a compound target material is relatively easy; the second is the useability in high oxygen background pressures (up to 1 Torr). For example, these are the reasons PLD became popular after the discovery of high-T_c materials, such as $La_{2-x}Sr_xCuO_4$ and $YBa_2Cu_3O_7$,[3,4] where it was paramount to get the ratio of the three cations correctly and to provide enough oxygen during growth at the same time.

Due to the use of a pulsed laser the deposition and growth are not continuous as with MBE; rather the deposition takes place in a couple of stages. When the laser pulse hits the target a dense layer of vapor is formed close to the surface of the target. This vapor is heated by the remainder of the pulse causing a buildup of pressure and partial ionization of the vapor. These first two steps take place in about 20-30 ns, the pulse duration. The pressure and ionization energy are then converted into kinetic energy, which results in an explosive expansion of the vapor and becomes visible as a *plasma*

Element	Center wavelength(nm)	Bandwidth fwhm (nm)	Peak transmission (%)
Al	395	10	48
Ba	551	9	56
Bi	473	10	65
Ca/La	419	10	42
Ca/La	421	10	40
Cu	326	11	20
O	261	6	19
Pr	500	11	23
Ru	371	9	34
Sr	460	8	52

Table 2.1: *An overview of the different filters that were used for various elements. Some elements that are listed were not used for work presented in this thesis, but are listed for completeness. Sometimes extra high or low pass filters (not listed) were inserted to limit noise.*

plume. The kinetic energy of these particles can be as high as several hundred eV,[5] much higher than when MBE is used. If these particles are not moderated before they reach the substrate they can cause sputter damage, which is why PLD is often used in conjunction with high background pressures (0.1 – 1 Torr) to thermalize the particles before they reach the substrate. The pressure that is needed to accomplish this is also dependent on the target-substrate distance, and the two need to be considered together. In the MBS system such high pressures are not achievable due to technical limitations, but there are ways to increase oxidation power (at low pressure) and minimize influence from sputtering. These issues will be discussed in more detail in section 2.2.5.

Also due to the nature of the pulsed laser the deposition rate will be very high temporarily, followed by a period of no deposition. The deposition time ranges from a few μs to hundreds of μs,[6] resulting in a deposition rate of 10^2 to 10^5 nm/sec for a short time.[7] The consequence is a separation between the deposition and growth phases of a material, which makes PLD an excellent tool to study surface mobility of atoms or initial nucleation for example.[8,9]

In the setup used, a Lambda Physik LPX 210 KrF excimer laser produces a 248 nm wavelength beam with typical pulse lengths of 20-30 ns. A rectangular mask shapes the beam selecting only the homogeneous part, and a variable attenuator permits variation of the pulse energy. The variable attenuator also offers the possibility to run the laser at the same voltage every run, which ensures the same pulse shape every time and therefore the best reproducibility. A lens makes an image of the mask on the target resulting in a well defined illuminated area. The target holder is designed to hold four targets and is mounted on an arm that can be introduced via its own load lock. One target position though is used for the alkali metal vapor sources discussed in the next section. Switching between targets is computer controlled, and when ablating the targets are rotating to prevent the creation of holes.

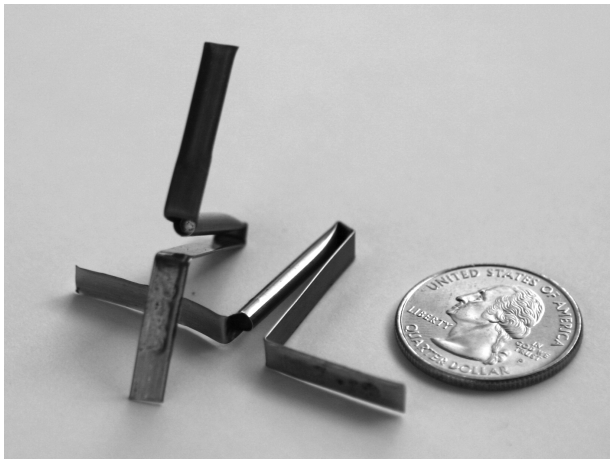

Figure 2.4: *Two Alvatec alkali metal vapor sources with a United States quarter dollar coin for size comparison.*

2.2.4 Alkali metal vapor sources

The two techniques described above can deposit a wide range of elements and compounds, but pure alkali metals are a problem. This is primarily because they are highly reactive, and sources of these elements would quickly oxidize when an oxygen atmosphere is used during deposition. To solve these problems we have used alkali metal vapor sources made by Alvatec, two of which are shown in figure 2.4. These sources were mounted on a PLD target position and are resistively heated with a constant current source. To prevent the alkali metal from oxidizing when still in air these tube are sealed with indium by the vendor. The indium melts readily at a current of about 3 A and a puff of argon can be observed with the residual gas analyzer (the sources are sealed under an argon atmosphere). The current that is needed to evaporate the alkali metal varies from element to element: for Li 9–11 A are needed, whereas Cs requires 4–8 A, where a higher current results in a higher deposition rate. The evaporation rate can be determined with a QCM at the sample position and is found to be very constant over time (deposition rates of 1 ML/min are attainable with this method). Deposition is performed by opening the shutter for the number of seconds required to grow the desired layer thickness.

2.2.5 Atomic oxygen

Besides the evaporated cations we need to supply enough oxygen to the sample during growth to create oxide thin films. MBE can only be used at low pressures and the MBS system is not set up to perform PLD at high pressures ($\sim$100 mTorr), where the technique is commonly used. A disadvantage of growing oxide thin films at such low oxygen pressures is the presence of oxygen vacancies. These defects not only diminish the crystallinity of the samples, they can also unintentionally dope the sample with

electrons. The unintentional doping is very much the case with PLD in the MBS system where the particles arriving at the surface have much higher kinetic energy (more than 100 eV in vacuum)[5] compared to MBE. These high energy particles then begin to function as a "sputter gun" and can cause selective sputtering of lighter elements, in particular oxygen. The sputter damage caused by PLD is hard to prevent in the MBS system since the oxygen pressure needs to be raised to the 0.1 Torr range to slow the particles down enough to prevent sputtering. It is possible to keep the background pressure low but provide ample oxidation power to the sample by using an atomic oxygen source. Therefore, for both MBE and PLD (in a UHV environment) a source of highly reactive, activated oxygen is necessary.

A microwave plasma source (Astex SXRHA) dissociates the oxygen molecules, at a cost of 5.1 eV per molecule,[10] which makes the resulting plasma highly reactive. By adjusting oxygen flow and generator wattage (200-600 W), the amount of atomic oxygen can be controlled.[11] The supplied flux of atomic oxygen ranges from 4×10^{16} atoms cm^{-2} s^{-1} for 200 W and 6 sccm flow to more than 1.4×10^{18} atoms cm^{-2} s^{-1} for 600 W and greater than 100 sccm flow. Sometimes compounds are not stable at high temperatures under strong oxidation conditions (for example $LaTiO_3$, which forms $La_2Ti_2O_7$ at high oxygen pressures) in which case it is better to deposit at low pressure and post-anneal the sample in atomic oxygen to fill the oxygen vacancies. Atomic oxygen is more reactive, and usually that means it diffuses more readily into a material. The most studied example of this is SiO_2 where a thicker oxide layer is formed when exposed to atomic oxygen,[12] even though it has been shown that oxygen transport in the material is in molecular oxygen form.[13]

2.2.6 Deposition conditions

To conclude this section an overview of the deposition conditions that were used to create the samples is given. The parameters for the samples grown by PLD are given in table 2.2 on the next page. The target type is mentioned because it is important to have targets that are as dense as possible to prevent the ablation of large particles. When these large clusters reach the substrate they disrupt the epitaxial growth of the material and cause large height variations. The same happens when the target material is not a good heat conductor, such as boron nitride. In the ideal case a single crystal target should be used. Not only because it is the densest available target; it is also very pure material. The $LaAlO_3$ target was a single crystal target (SurfaceNet GmbH); all other targets are dense sintered pellets (Praxair Specialty Ceramics). Before each run the rotating targets are ablated for two minutes at a laser frequency of 4 Hertz (pre-ablation) to clean the surface of the target.

In the case of $SrRuO_3$ numerous samples were grown by MBE. For these samples the deposition conditions were the same as for the PLD films. The deposition rates were ∼0.3 Å/s for Ru and ∼1.0 Å/s for Sr, which results in a near stoichiometric $SrRuO_3$ film.

A third type $SrRuO_3$ films were grown in a different deposition system with PLD. In this system PLD can be performed at high pressures (∼300 mTorr) in which case the particles coming from the target are thermalized before they reach the substrate

Material	Target type	O_2 pressure (mTorr)	T (°C)	E_d (J/cm^2)	O* (W)
$SrRuO_3$	Sintered	10^{-5}	700	2.1	0 – 600
CuO	Sintered	10^{-5}	600	1.2	600
$LaAlO_3$	Single crystal	10^{-6}–10^{-4}	815	1.2	0
$LaTiO_3$	Sintered	10^{-5}	700	1.2	0
$SrTiO_3$	Sintered	10^{-5}	700	1.2	0

Table 2.2: *An overview of the PLD deposition conditions used in the MBS system for creating the samples that this thesis deals with. From left to right the oxygen pressure, the substrate heater set point temperature, the laser density on the target, and the atomic oxygen wattage of the microwave source are given. Conditions for samples made with a different deposition method (MBE) or in a different deposition system are given in the text.*

and no atomic oxygen is needed to oxidize the samples. This system is not equipped with RHEED to monitor sample morphology during growth. The thickness of samples made on this system is determined by calibrating the deposition rate per laser pulse by measuring the thickness of a thick sample with XRD. The same deposition settings were used as in the MBS system, with the exception of the pressure which was 320 mTorr in total, made up of 50% argon and 50% oxygen.

2.3 $SrTiO_3$ substrates

For all the samples discussed in this thesis $SrTiO_3$ was used as the substrate material. $SrTiO_3$ has a cubic perovskite unit cell that has a lattice parameter of 3.905 Å. It is often chosen as a substrate material for oxides because of its good lattice match with most other oxides. Cleaning the surface of the substrate is important and can be done by cleaning with solvent and annealing the sample in oxygen at an elevated temperature, but as it turns out the terminating layer of the substrate often has a large influence on the initial growth.[14] For this reason it is important to have excellent control over this terminating layer. The following paragraphs will address this issue briefly after which some of the basic properties of $SrTiO_3$ will be described.

2.3.1 Surface treatment

$SrTiO_3$ is built up out of alternating SrO and TiO_2 layers, which are individually charge neutral. The top layer can be either one and when substrates are received from the vendor the surface is a mixture of the two. The vendor cuts the substrates along the crystal axes and polishes the surface. However, an atomically perfect cut is never obtained, which results in the formation of steps of either a half or a full unit cell high. When these samples are annealed at 950 °C the SrO tends to move to the step edges and forms an easily recognizable morphology with a lot of sharp angles at the step edges, which can be easily observed with AFM (see section 2.4.2 on page 22). This results in steps of half a unit cell every time one goes from the TiO_2 terminated surface to a SrO terminated surface or vice versa.

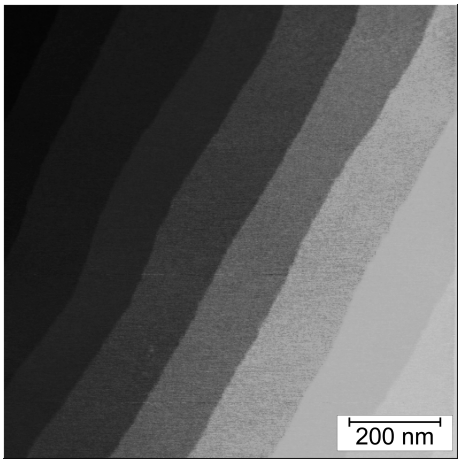

Figure 2.5: *A typical AFM scan of an HF treated $SrTiO_3$ substrate. The surface after chemical etching is TiO_2 terminated and one unit cell high steps are formed.*

Having single terminated surfaces (either SrO or TiO_2) offer a much better defined starting surface, and a method has been found to make the surface of $SrTiO_3$ single terminated. Through a chemical treatment with HF [15] the SrO (which is transformed into $Sr(OH)_2$ by reacting with water) can be selectively etched away with a relatively weak acid without damaging the rest of the surface, which occurs when water is not used. [16] The result is a surface with only TiO_2 on it, which after annealing at 950 °C form very nice straight step edges as can be observed in figure 2.5.

The following describes the treatment for the substrates in this thesis. First the as-received substrates are cleaned with solvents in an ultrasonic bath: chloroform, acetone, and methanol are used in that order for 30 minutes each. Substrates are blown dry with nitrogen after the methanol cleaning and placed on a Teflon holder. The holder is placed in water in the ultrasonic bath for 30 minutes. The Teflon holder is then taken directly out of the water and placed in the NH_4F (87.5%) buffered HF (12.5%) solution (manufactured by Riedel-deHaan), which has a pH of 5.5. The holder is left in the ultrasonic bath for 30 seconds. The holder is then dipped in three beakers of water to get rid of all the acid and finally placed in a beaker containing methanol. The substrates are then taken of the holder, blown dry with nitrogen and placed in a quartz boat in a furnace. Quartz boats were found to be superior to alumina boats, which tend so contain a lot of contaminants that are hard to remove. The substrates are heated in flowing oxygen to 950 °C and kept there for one hour. This procedure results in surfaces of the quality shown in figure 2.5. Great care needs to be taken to avoid contaminants that can come from the solvents, water, or the furnace since they will all deteriorate the surface quality.

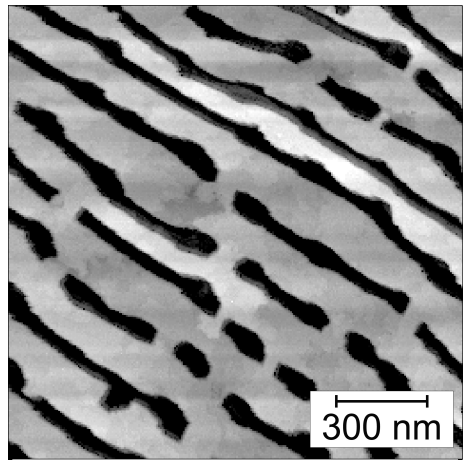

Figure 2.6: *A scanning tunneling microscopy scan of a 30 nm thick $SrRuO_3$ film on $SrTiO_3$. Although termination of the substrate was TiO_2, as shown in fig 2.5 on the facing page, before the sample was heated in the deposition system, Sr diffused to the surface and moved to the step edges. On the SrO terminated areas $SrRuO_3$ did not grow as fast as on the TiO_2 terminated areas resulting in the trenches. On the flat areas though unit cell high steps can be observed.*

The creation of such perfect surfaces in a 1 bar oxygen atmosphere does not guarantee that they are also stable in a vacuum environment when heated up.[17] Analysis done by others[18] seems to suggest that Sr sometimes migrates to the surface and forms small patches of SrO there. Whether or not this happens seems to vary from batch to batch of the substrates, which suggests that the stoichiometry of the substrates has an influence on this process. This effect was not observed when Nb doped $SrTiO_3$ substrates were used, which tend to have better stoichiometry. Chances are that all the substrates tend to be slightly Sr rich, which will promote the diffusion of Sr to the surface. A double surface treatment method is suggested by some[18] to solve this problem, but has not been performed on samples discussed in this thesis.

Whenever the Sr diffuses to the surface it results in double termination, which is not beneficial to the growth of a material. The material might, for example, have a preference for one or the other and grow faster some places then others. Such non uniform growth results in many defects in the film, and for very thin films these might dominate the properties that are measured. An extreme example is given in figure 2.6 where $SrRuO_3$ has been grown on $SrTiO_3$ with some SrO at the steps. Big trenches have formed, which obviously influence for example the transport properties of the sample.

2.3.2 Oxygen stoichiometry

The ratio of Sr to Ti matters a lot to the surface properties of the substrates, but the oxygen stoichiometry actually has more influence on most of the bulk properties.

When oxygen is taken out the electrons, which are freed up, can either form an F-center and be localized or be delocalized and go into the Ti $3d$ conduction band.[19,20] $SrTiO_3$ starts to conduct at doping levels of 10^{17} electrons cm^{-3}) where the observed mobility of the electrons is very high[21] (10^4 cm^2 V^{-1} s^{-1}). The mobility decreases as more oxygen vacancies and therefore electrons are created. At high doping levels (10^{19} electrons cm^{-3}) $SrTiO_3$ even becomes superconducting,[22,23] with a maximum T_c of 0.3 K with oxygen doping for a carrier concentration of 10^{20} cm^{-3}. As was mentioned in section 2.2.5 on page 11 the particles coming from the target, in the case of laser ablation, have high kinetic energies and therefore have the potential to sputter light elements from the substrate, which will result in the measurement of conductivity or even superconductivity in the case of $SrTiO_3$. Therefore, great care needs to be taken when analyzing thin films grown on $SrTiO_3$ at low pressures to exclude any contributions from the substrate.

Apart from the oxygen doping issue $SrTiO_3$ also exhibits a structural phase transition at low temperature (110 K) where it becomes tetragonal rather than cubic.[24,25,26] This change is small and is usually not relevant to the properties of the film on top of the substrate. Stashans and Vargas show,[27] however, with calculations such a small change in the structure can have a profound impact on how oxygen vacancies behave in the lattice.

2.4 Sample analysis

There is an abundance of analysis techniques and the ones that are relevant to understand the results presented in this thesis, are described in this section. An important distinction is made between *in situ* and *ex situ* analysis: *in situ* analysis means that the samples have not been taken out of the vacuum system; *ex situ* analysis requires the samples to be taken out and thereby be exposed to air. Keeping the samples under vacuum offers the possibility to look at the samples without contamination, which is especially important when dealing with such surface sensitive techniques like RHEED and PES. Sometimes it is the only way to study a material if exposing it to air has detrimental effects on its properties. If the sample is stable in air, *ex situ* techniques can be applied, but one should always keep in mind when dealing with very thin films and/or with surface sensitive techniques that contributions from the surface might dominate the measurements.

First the *in situ* techniques and subsequently the *ex situ* techniques are discussed.

2.4.1 *In situ* techniques

As can be seen in figure 2.2 on page 7 there are several analysis tools on the deposition system. In this section we will only discuss the two that were used extensively and are essential to understanding the results in subsequent chapters. The first technique that will be discussed is RHEED, an electron diffraction technique that can be used during film growth and gives structural information. The second is Photoemission Spectroscopy (PES), which is a collection of slightly different techniques, and yields

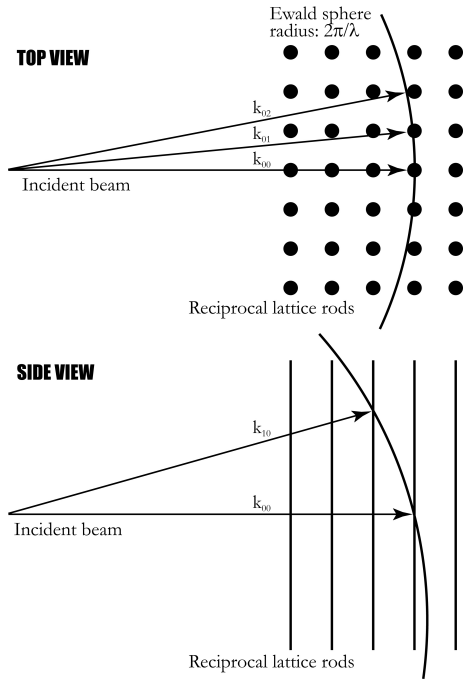

Figure 2.7: *Ewald sphere construction for RHEED. The film plane is horizontal and the reciprocal lattice rods are represented either like dots (top view) or rods (side view). The k_{xy} vectors are the diffracted beam directions. The incident beam coincides with the k_{00} diffracted beam. After Ohring.*[28]

information on material composition, chemical states of atoms, valence band structure, degree of correlation, and even structural information.

Reflection high energy electron diffraction

Reflection high energy electron diffraction (RHEED) is an indispensable tool to track the structural properties of materials during growth. In RHEED an electron beam comes in at a grazing angle of less than few degrees. The beam with an energy of 30 keV in our setup (Staib Instruments) diffracts of the surface of the sample and hits a phosphor screen on the other side. The diffraction pattern is caused only by the first couple of angstroms of the sample, because the beam comes in at such a low angle, making this a very surface sensitive technique. A great advantage of this technique — especially compared to the related technique low energy electron diffraction (LEED) — is that the geometry of the setup does not interfere with the deposition and therefore the growth can be monitored in real-time.

To get a feel for what the diffraction pattern will look like one needs to approach the problem in reciprocal space. A 2D (i.e. surface) array of real points will transform into a rod in reciprocal space. The incoming electron wave will have a wave vector

of magnitude $2\pi/\lambda$ in reciprocal space. By drawing a so-called Ewald sphere with radius $2\pi/\lambda$ (very large in the case of RHEED since $\lambda \approx 7$ pm) with its center on the incident beam path so that the sphere terminates at the reciprocal lattice origin, it can be shown that the only possible directions of the diffracted rays are those where the sphere intersects with the reciprocal lattice rods, which is graphically presented in figure 2.7 on the previous page. This condition can be mathematically reduced to Bragg's law. The diffraction pattern can consist of spots or streaks. If the lattice is nearly perfect (the reciprocal lattice rods are as narrow as possible), thermal vibrations are low, and the energy of the incoming electrons is well defined we will see spots. This is called a 2D diffraction pattern. In the case of such a high quality sample Kikuchi lines, which are caused by inelastic scattering processes, also become visible. When some imperfections exist, for example some minor height changes, the spots will become streaks (due to the broadening of the reciprocal lattice rods). When the height differences become larger the electron beam starts to pass through these features and cause a 3D diffraction pattern (since it now also carries information of the direction perpendicular to the surface). The 3D pattern also consists of sharp spots, but can be easily distinguished from the 2D spots because the 3D spots do not move when the incident angle is changed, whereas the 2D spots do. Since the diffraction is governed by Bragg's law the spacing of the spots or streaks on the phosphor screen is related to a repeating feature on the surface of the sample, in the best case this would be the unit cell of the material. In-plane lattice parameters of an unknown material can be determined by comparing to a diffraction pattern of a well know material as we shall see in the chapter on CuO.

Besides the diffracted spots there is the specular or reflected spot. The intensity of the specular RHEED spot is a function of step density on the sample surface. This information can also be extracted from the intensity of the diffracted spots, but there might be a phase difference. Maximum intensity is observed when the step density is lowest, i.e. an atomically smooth surface. When material is deposited it usually forms islands at elevated temperatures, thereby increasing the step density and reducing the specular spot intensity. In the case of the layer-by-layer growth mode, where a layer is first completely formed before the start of a new one, this means that the specular spot intensity will go through a minimum when the step density is highest (around 40% of one unit cell) [29] and then climb back up to its original value when a complete monolayer is formed. If the layer-by-layer growth mode persists until very large thicknesses, this gives the most accurate measure of thickness since every oscillation represents the growth of exactly one unit cell and the dimension of the unit cell are usually well known. If the growth mode changes, for instance to step-flow, this is no longer possible, but the first couple of unit cells should still give enough oscillations to extrapolate from, if the growth speed is kept constant.

Photoemission spectroscopy

In this section three different photoemission spectroscopy (PES) techniques will be discussed, all of which are performed in the analysis chamber of the MBS system: x-ray photoemission spectroscopy (XPS), ultraviolet photoemission spectroscopy (UPS), and

X-ray Photoemission Diffraction (XPD).[30,31,32] The first two are well known techniques to get information about the chemical composition of samples, the third however is a much less used technique to get 3D structural information and will therefore be discussed in much more detail.

XPS is based on the well known photoelectric effect, observed late 19^{th} century and first described by Albert Einstein in 1905.[33] An incoming photon gets absorbed by an atom and emits an electron. In this case AlKα x-rays are used with an energy of 1486.7 eV. To eject an electron from its atom a very well defined energy is required, which is known as the binding energy, E_B. Since the energy of the incoming photon is known and the kinetic energy, E_K, of the emitted electron can be measured, the binding energy of the electron can be calculated as follows:

$$E_B = \mathrm{h}\nu - E_K$$

The use of photoelectrons to determine material properties seemed severely limited because of inelastic scattering within the sample: electrons lose energy escaping form the solid, and hence do not carry with them information that would help determine their origin with any precision. In the 1950's and 60's, a group at Uppsala University in Sweden greatly improved the spectrometers available to observe photoelectrons and made a systematic study of the process.[34] By analyzing the kinetic energy of the electrons and calculating the binding energy, they could identify the elements that are in the material since each element has a unique fingerprint of binding energies. By measuring the areas under the peaks and applying the correct sensitivity factor for each element one can estimate the ratio of the elements relative to one another. This gives results that are accurate within a few percent.

A very useful feature of XPS is that the binding energies for many elements vary with the valence of the atom. This permits the determination of chemical bonding in the near-surface region. While this shift does not occur for all elements, it is often extremely valuable in determining the chemical structure of the surface region of a solid. When an atom is in an environment in which the electron density around it is lowered, its nucleus is less screened, and its binding energies tend to increase. The inverse is true for an increase in electron density. A lot of the XPS work done in this thesis makes use of this effect.

XPS measurements were performed *in situ* with a VG Scientific ESCAlab Mark II system. X-rays were generated with a twin anode (Mg or Al) and were non-monochromatic.

Ultraviolet photoelectron spectroscopy (UPS) is closely related to XPS. The difference in the setup is the excitation source, which is now replaced by a helium lamp. The helium lamp emits photons with a much lower energy, either HeI (21.2 eV) or HeII (40.8 eV). This makes it much easier to study the valence band levels of a material. UPS measurements were performed *in situ* with the same system as for XPS (also non-monochromatic).

XPS and UPS are very surface sensitive techniques because of the electron escape depth that is in the order of 20 Å. By tilting the sample with respect to the detector, the amount of signal that comes from nearer the surface is enhanced due to the greater

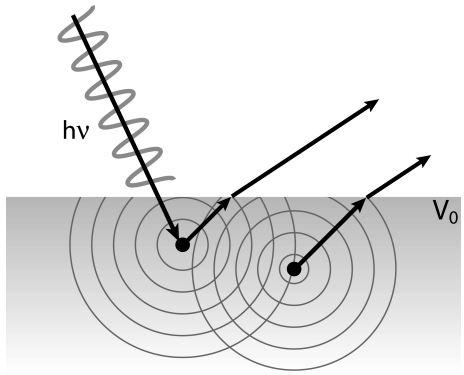

Figure 2.8: *The basic principle of XPD is shown. The primary electron wave coming from the first atom interferes with the secondary electron wave from a nearby atom, which results in an angular dependence of the electrons coming out of the sample. The surface potential V_0 changes the direction of the electrons as they exit the material.*

distance the electron has to travel through the material. For amorphous materials this technique works ideally. However, when some order exists in the studied sample, because it is crystalline for example, the intensity has an angular distribution that is related to the ordering in the sample. This is called X-ray Photoemission Diffraction (XPD) and was first observed in 1970 by Siegbahn *et al.*[35] when they investigated the angular distribution of core level and Auger electrons from Na and Cl atoms in NaCl. They found that diffraction of the photoelectrons of the crystal lattice caused the angular distribution and when atoms line up along a certain direction the intensity was greatly enhanced. An illustration of this phenomenon is given in figure 2.8 where two atoms are shown that constructively interfere along a certain direction. The primary electron wave coming from the first atom interferes with the secondary electron wave from a nearby atom, which results in an angular dependence of the electrons escaping from the sample. These diffraction peaks are dependent on the wavelength of the electron waves, as opposed to the diffraction peaks along the direction of some lattice points, which are subject to what is most commonly called *forward focusing*. The strongest diffraction peaks are therefore to be expected when most atoms line up. Note that the surface potential, V_0 in figure 2.8, will refract the electrons by a minor amount, which could be relevant when studying very small changes. The great advantage of this technique is that you can measure element specifically by looking at the angular distribution of electrons with a specific kinetic energy, which means that a substrate (containing different elements) is not interfering with the measurement of a thin film even when it is grown epitaxially.

In the early 1970's this technique promised significant results, but its application has remained limited. For the most part, it has been used for studies of adsorbed gas layer, for instance CO on Ni(100).[36,37] In that system the study is done with HeI radiation (21.2 eV) and depending on whether the CO molecule stands up perpendicular to the surface (which is the case on Ni(100)) or lies parallel to the surface the intensity

changes. When layers are thicker and are crystalline though the usefulness of XPD is greatly reduced, because it is much easier to use a technique like x-ray diffraction (XRD, see section 2.4.2), which will give unit cell dimensions with greater accuracy and results that are much easier to interpret. In order to interpret the results one needs to simulate the diffraction pattern, although the angles at which the forward scattering will take place can be easily calculated when the crystal structure is known. The niche for this technique lies in the regime where the layer thickness is less than 20 Å, as we will see for the CuO in chapter 5. At that point it becomes hard for XRD to resolve the unit cell. The layer thickness limit is even a little higher when films are grown epitaxially on a substrate material, because of the overlap of the strong substrate peaks and weak film peaks with XRD (such thin films are usually measured at grazing incoming angles).

The analysis of the spectra is not very straightforward and requires simulation.[38] Before simulation though the forward scattering peaks can be calculated based on an assumed structure and compared to measurements. The strongest measured peaks should lie very close to the calculated angles. Simulating the data is the only way to reproduce the more intricate diffraction features which can help to resolve the structure. The software used for the simulations in this thesis is written by Abajo *et al.*[39] and calculates the diffraction pattern based on a large set of parameters, which include the unit cell, the electron energy, the inelastic mean free path, the Debye temperature, etc. These parameters will be given together with the simulations later in this thesis.

2.4.2 *Ex situ* techniques

Once the sample is taken out of the system and if it is stable in air there is a wide range of analysis equipment available. Most of this equipment is available at the Stanford Nanocharacterization Laboratory, which is housed in the McCullough building on Stanford Campus. The following tools that will be discussed are: XRD, AFM, SEM, XPS, and AES. Electrical transport measurements will be explained next and this section will be concluded with a discussion of the equipment that was used to perform the magnetic measurements, which was done in collaboration with Jing Xia and Aharon Kapitulnik at Stanford University.

X-ray diffraction

X-ray diffraction (XRD)[40] was used to obtain crystal structure information on the samples that were grown. This technique has the advantage of being non-destructive and yields high precision results without elaborate sample preparation. Unfortunately, when films become too thin there is not enough material to produce high intensity diffracted beams, of which the CuO films (discussed in chapter 5 on page 77) are a good example. To increase the diffracted signal strength it is possible to increase the intensity of the incoming beam by going to a synchrotron facility. This can also be used to look at very weak reflections, as we will show in chapter 4 about $SrRuO_3$. Our routine XRD experiments were performed on a Philips X'Pert thin film diffractometer with Bragg-Brentano geometry, which uses Cu Kα_1 radiation with an energy of 8048

eV or equivalently a wavelength of 1.54051 Å. Measurements done with synchrotron radiation were performed at beam line 7-2 at the Stanford Synchrotron Radiation Laboratory (SSRL). For temperature dependent structural analysis an Anton-Paar hot stage was used.

Atomic force microscopy

To get high resolution topography information of the sample, atomic force microscopy (AFM) was performed on a Multimode Scanning Probe Microscope (Veeco, Cambridge, United Kingdom) with a Nanoscope IV controller. The microscope was used in contact mode with a scanner with a maximum scan range of $100 \times 100\ \mu m^2$. More information on AFM can be found in the review article of Giessibl.[41]

Scanning electron microscopy

In a scanning electron microscope (SEM),[42] a fine beam of electrons is scanned across the surface of a specimen. A detector monitors the intensity of a chosen secondary signal from the specimen (for example, secondary electrons). If, for any reason, the intensity of the emitted secondary signal changes across the specimen then contrast will be seen in the image on the display screen. The resulting image is strikingly similar to what would be seen through an optical microscope: the illumination and shadowing show a natural-seeming topography. The instrument used for the SEM images in this thesis is an FEI XL30 Sirion SEM.

Photoemission spectroscopy

For *ex situ* XPS an SSI S-Probe Monochromatized XPS Spectrometer, which uses Al Kα radiation (1486 eV) as a probe, was utilized. This instrument permits the analysis of areas as small as 100 microns in diameter and offers a full width at half maximum line width of 1.0 eV for the gold $4f_{\frac{7}{2}}$ line. For a more elaborate description of XPS as a technique see section 2.4.1 on page 18 or one of the reference works.[30,31,32]

Auger electron spectroscopy

Auger electron spectroscopy (AES)[30,31,32] is a technique that is very much related to XPS. Like XPS it is extremely sensitive and only compositional information from the top 10 Å is obtained. The same kind of spectrometer is used as for XPS, but now the excitation source is a focussed electron beam. The electron beam can be scanned as in an SEM and the region of interest can therefore be imaged. This offers the possibility of getting compositional information from very small areas of about 10 nm in diameter. By taking spectra of an array of points within an image a map can be made of the chemical composition on the surface that can be compared to the SEM picture taken. This way physical structure and chemical surface information can be linked. For the AES data in this thesis a Phi 700 Auger Nanoprobe was used.

Electrical transport

To measure electrical transport properties, such as the resistivity, the number of charge carriers, and the mobility, a Quantum Design physical property measurement system (PPMS) was used. Normally one would have to pattern the sample in order to measure such quantities, but Van der Pauw devised a way to measure these properties in thin films of any dimension.[43] He originally did this work on semiconducting films, but it works equally well for oxide thin films. Consider a uniform square sample with contacts in each of the corners that are numbered clockwise 1 through 4. These contacts are usually made by wire-bonding aluminum wires to the sample. Now we can measure the resistances R_A and R_B, which are defined as follows:

$$R_A = \frac{V_{43}}{I_{12}} \text{ and } R_B = \frac{V_{14}}{I_{23}}$$

The sheet resistance, R_S, can be calculated by numerically solving the Van der Pauw equation:

$$\mathrm{e}^{(-\pi \frac{R_A}{R_S})} + \mathrm{e}^{(-\pi \frac{R_B}{R_S})} = 1$$

This value for R_S can be related to the resistivity, ϱ, if the thickness of the conducting layer is known by $\varrho = R_S d$.

To determine the number of charge carriers the Hall effect needs to be measured. In the same Van der Pauw geometry this is done by measuring the voltage between contacts 2 and 4 (V_H), while sending a current from contact 1 to 3 (I_H). This hall voltage is related to the sheet carrier density, n_S, as follows:

$$n_S = \frac{I_H B}{\mathrm{q}|V_H|}$$

B is the applied magnetic field parallel to the surface normal. The bulk carrier density, n, can be determined if the film thickness is known by $n = n_S/d$.

When both R_S and n_S are known the mobility of the electrons can be calculated even if the film thickness is unknown. This calculation is:

$$\mu = \frac{|V_H|}{R_S I B} = \frac{1}{\mathrm{q} n_S R_S}$$

All of the calculations above only give the correct results when contacts are ohmic and sample uniformity is high. Special care needs to be taken in case the sample is susceptible to photo induced carriers, which can be minimized by keeping the sample before and during the measurement in a dark environment.

Kerr effect measurement

Magnetic measurements on thin films often offer a challenge due to the very small signal that is available. Even with SQUID setups it is difficult to get magnetic information from layers that are only several MLs thick. A better method is to measure the magnetization optically by using magneto-optic effects. Magneto-optic effects result

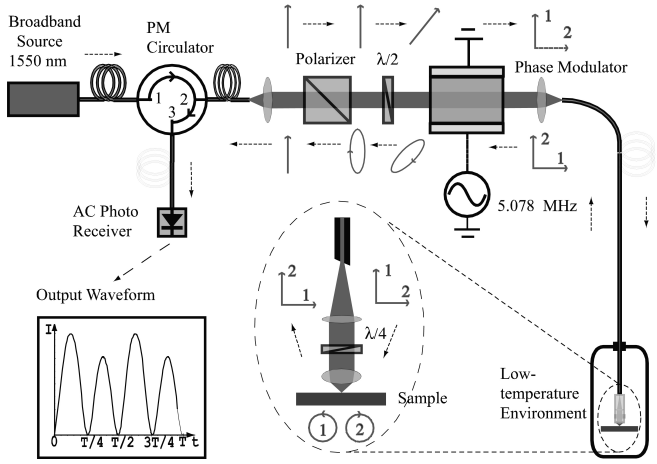

Figure 2.9: *A schematic overview of the Sagnac interferometer that measures the Kerr effect in samples.*

from the interaction of photons with spins, mediated through spin-orbit coupling, and provide a broad variety of tools for investigation of magnetic and electronic properties of materials. Linearly polarized light that interacts with magnetized media can exhibit both ellipticity and a rotation of the polarization state.[44] These effects are generally categorized into two primary phenomena, the Faraday effect, which occurs when electromagnetic radiation is transmitted through a magnetized medium, and the Kerr effect, which describes the state of the light reflected from the magnetized medium. This second phenomenon, also called the magneto-optic Kerr effect (MOKE),[45] is further categorized by the direction of the magnetization vector with respect to the reflection surface and the plane of incidence. In magnetic materials the size of MOKE signals is large enough to be detected with simple crossed-polarizer techniques. When the layer thickness gets to be on the order of a couple of unit cells, more sensitivity is needed. To achieve higher sensitivity, modulation schemes are required. The optimized design used for the measurements in this thesis uses fiber Sagnac interferometry and offers a sensitivity of 10^{-7} rad/$\sqrt{\text{Hz}}$ with only 10 μW optical power. Since a fiber is used to reach the sample it can be conveniently placed in a He-3 cryostat which enables measuring magneto-optic effects to temperatures of 0.5 K. A magnet present in the cryostat offers the possibility to measure in magnetic fields up to 4 T. Figure 2.9 shows a schematic of the design. For more information about the Sagnac interferometer see the article by Xia *et al.*[46] Note that only the out-of-plane component of the magnetic moment is measured with this setup.

Bibliography

1. T. J. Hill, ed., *Physical Vapor Deposition* (Temescal, 1986), 2nd ed.

2. C. Lu, M. J. Lightner, and C. A. Gogol, Journal of Vacuum Science and Technology **14**, 103 (1977).

3. J. G. Bednorz and K. A. Müller, Zeitschrift für Physik B **64**, 189 (1986).

4. M. K. Wu, J. R. Ashburn, C. J. Torng, P. H. Hor, R. L. Meng, L. Gao, Z. J. Huang, Y. Q. Wang, and C. W. Chu, Physical Review Letters **58**, 908 (1987).

5. Y. Yamagata, A. Sharma, J. Narayan, R. M. Mayo, J. W. Newman, and K. Ebihara, Journal of Applied Physics **86**, 4154 (1999).

6. T. Okada, Y. Nakata, M. Maeda, and W. K. A. Kumuduni, Journal of Applied Physics **82**, 3543 (1997).

7. D. B. Geohegan and A. A. Puretzky, Applied Physics Letters **67**, 197 (1995).

8. H. Jenniches, M. Klaua, H. Hoche, and J. Kirschner, Applied Physics Letters **69**, 3339 (1996).

9. G. Rijnders, D. H. A. Blank, J. Choi, and C.-B. Eom, Applied Physics Letters **84**, 505 (2004).

10. D. R. Lide, ed., *CRC Handbook of Chemistry and Physics* (CRC Press, 2006), 87th ed.

11. N. J. C. Ingle, R. H. Hammond, M. R. Beasley, and D. H. A. Blank, Applied Physics Letters **75**, 4162 (1999).

12. J. R. Engstrom, D. J. Bonser, and T. Engel, Surface Science **268**, 238 (1992).

13. M. A. Lamkin, F. L. Riley, and R. J. Fordham, Journal of the European Ceramic Society **10**, 347 (1992).

14. J. Choi, C. B. Eom, G. Rijnders, H. Rogalla, and D. H. A. Blank, Applied Physics Letters **79**, 1447 (2001).

15. G. Koster, B. L. Kropman, G. J. H. M. Rijnders, D. H. A. Blank, and H. Rogalla, Applied Physics Letters **73**, 2920 (1998).

16. M. Kawasaki, K. Takahashi, T. Maeda, R. Tsuchiya, M. Shinohara, O. Ishiyama, T. Yonezawa, M. Yoshimoto, and H. Koinuma, Science **266**, 1540 (1994).

17. T. Nishimura, A. Ikeda, H. Namba, T. Morishita, and Y. Kido, Surface Science **421**, 273 (1999).

18. T. Ohnishi, K. Shibuya, M. Lippmaa, D. Kobayashi, H. Kumigashira, M. Oshima, and H. Koinuma, Applied Physics Letters **85**, 272 (2004).

19. V. E. Henrich, G. Dresselhaus, and H. J. Zeiger, Physical Review B **17**, 4908 (1978).

20. M. Cardona, Physical Review **140**, A651 (1965).

21. H. P. R. Frederikse and W. R. Hosler, Physical Review **161**, 822 (1967).

22. C. S. Koonce, M. L. Cohen, J. F. Schooley, W. R. Hosler, and E. R. Pfeiffer, Physical Review **163**, 380 (1967).

23. J. F. Schooley, W. R. Hosler, E. Ambler, J. H. Becker, M. L. Cohen, and C. S. Koonce, Physical Review Letters **14**, 305 (1965).

24. L. Rimai and G. A. deMars, Physical Review **127**, 702 (1962).

25. G. Rupprecht and R. O. Bell, Physical Review **125**, 1915 (1962).

26. G. Shirane and Y. Yamada, Physical Review **177**, 858 (1969).

27. A. Stashans and F. Vargas, Materials Letters **50**, 145 (2001).

28. M. Ohring, *The Materials Science of Thin Films* (Academic Press, 1991).

29. A. J. H. M. Rijnders, Ph.D. thesis, University of Twente (2001).

30. D. Briggs and J. T. Grant, eds., *Surface Analysis by Auger and X-Ray Photoelectron Spectroscopy* (IM Publications and SurfaceSpectra Limited, 2003).

31. J. Berkowitz, *Photoabsorption, Photoionization, and Photoelectron Spectroscopy* (Academic Press, 1979).

32. J. C. Vickerman, ed., *Surface Analysis, The Principal Techniques* (Wiley, 1997).

33. A. Einstein, Annalen der Physik **17**, 132 (1905).

34. C. Nordling, E. Sokolowski, and K. Siegbahn, Physical Review **105**, 1676 (1957).

35. K. Siegbahn, U. Gelius, H. Siegbahn, and E. Olson, Physics Letters A **32**, 221 (1970).

36. S. Kono, S. M. Goldberg, N. F. T. Hall, and C. S. Fadley, Physical Review Letters **41**, 1831 (1978).

37. L. G. Petersson, S. Kono, N. F. T. Hall, C. S. Fadley, and J. B. Pendry, Physical Review Letters **42**, 1545 (1979).

38. S. A. Chambers, Advances in Physics **40**, 357 (1991).

39. F. J. García de Abajo, M. A. Van Hove, and C. S. Fadley, Physical Review B **63**, 075404 (2001).

40. M. Birkholz, *Thin Film Analysis by X-Ray Scattering* (Wiley, 2006).

41. F. J. Giessibl, Reviews of Modern Physics **75**, 949 (2003).

42. J. I. Goldstein, D. E. Newbury, P. Echlin, D. C. Joy, A. D. Romig, C. E. Lyman, C. Fiori, and E. Lifshin, *Scanning Electron Microscopy and X-Ray Microanalysis* (Plenum, 1994), 2nd ed.

43. L. J. van der Pauw, Philips Technical Review **20**, 220 (1958).

44. Z. Q. Qiu and S. D. Bader, Review of Scientific Instruments **71**, 1243 (2000).

45. P. N. Argyres, Physical Review **97**, 334 (1955).

46. J. Xia, P. T. Beyersdorf, M. M. Fejer, and A. Kapitulnik, Applied Physics Letters **89**, 062508 (2006).

Chapter 3

Oxide interface effects

3.1 Introduction

In 2004 Ohtomo and Hwang[1,2] reported the existence of a conducting electron layer at the hetero-interface between two nominal insulators, $SrTiO_3$ and $LaAlO_3$. This remarkable result has intrigued many researchers in the field.[3,4,5] Equally remarkably, Ohtomo and Hwang[1,2] found that the TiO_2/LaO interface between $SrTiO_3$ and $LaAlO_3$ has a sheet carrier density of $\sim 10^{17}$ electrons/cm^2 and a mobility of 10^4 cm^2 V^{-1} s^{-1}, as inferred from conductivity and Hall-effect measurements; each of these is strikingly large. The origin of the conductivity is not clear, but is suggestive of a very interesting charge transfer system due to valence mismatch of insulators.

This chapter contains a full account of our findings on this system. The growth of the material is discussed briefly and then we will present results from transport measurements, photoemission spectroscopy, near edge x-ray absorption spectroscopy (NEXAS), visible to vacuum UV-spectroscopic ellipsometry (vis-VUV-SE), and oxygen annealing experiments. We will show that the magnitude of the sheet density and the mobility of the electrons are sensitive functions of the deposition conditions in ways that suggest that the origin of this large sheet charge density is oxygen vacancies (donating electrons) in the $SrTiO_3$ substrate. Further, we argue that these vacancies are introduced by the pulsed laser deposition (PLD) process used by us and all previous authors to grow these hetero-structures. Besides this system we will also examine the interface between $LaTiO_3$ and $SrTiO_3$ where in addition to conductivity magnetic effects have been predicted.[6] Before turning to the growth and properties of the $LaAlO_3/SrTiO_3$ interfaces, the different proposed doping mechanisms are introduced.

This work was published in Physical Review Letters and Physical Review B.[7,8]

3.1.1 Doping models

Some insight into the possible sheet charge densities at a $SrTiO_3/LaAlO_3$ interface can be seen from the following considerations, which relate to an *intrinsic* doping mechanism. $SrTiO_3$ consists of charge neutral SrO and TiO_2 layers, whereas the AlO_2^- and

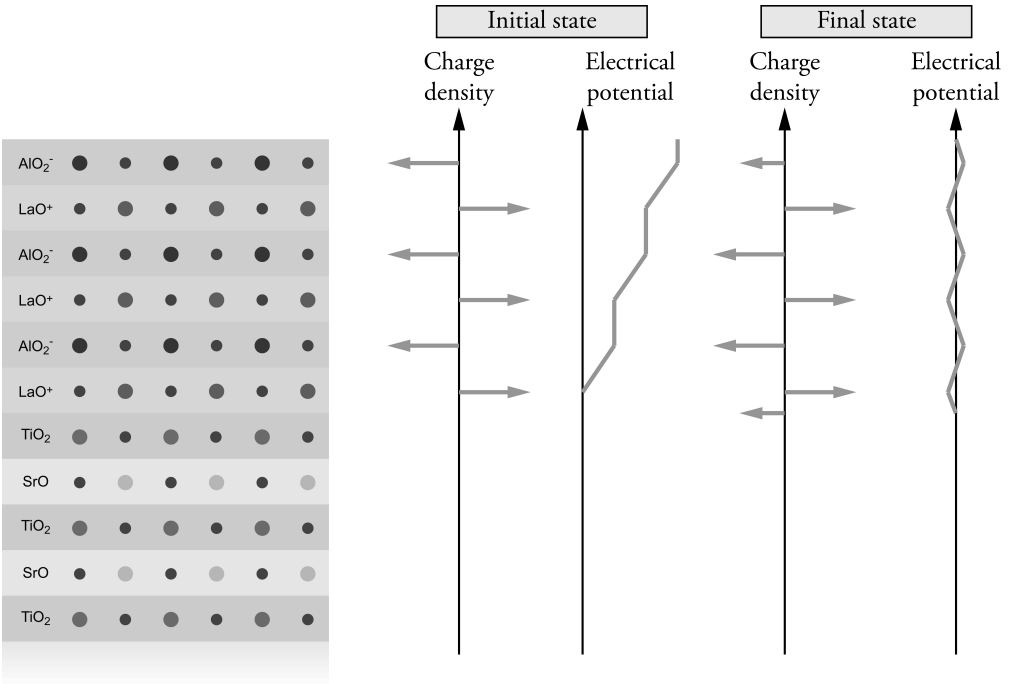

Figure 3.1: *An illustration of the intrinsic doping mechanism. The charge density in the $LaAlO_3$ varies from +1 to -1 from layer to layer causing the potential in the material to increase monotonically (initial state). One solution to correct for this large potential is to move half an electron per unit cell to the interface. This change in charge density corrects the diverging potential (final state).*

LaO^+ layers in $LaAlO_3$ have net charge. For an ideal planar interface this yields a net interface charge equal to half that of the last plane, if no other reconstructions take place.[9] Indeed a neutralizing charge at the interface is required to avoid a *polarization catastrophe* that arises due to this net interface charge, which is graphically depicted in figure 3.1. If left uncompensated, the energy associated with this polarization grows indefinitely as the thickness of the $LaAlO_3$ layer increases. Therefore, electrons have to be promoted to the conduction band of $LaAlO_3$ at some point. The charge that is necessary to prevent this polarization catastrophe is equal to half an electron per unit cell, or 3.2×10^{14} cm^{-2}. Note that this estimate applies only for perfectly stoichiometric $LaAlO_3$ and in this sense is an approximate upper limit in the intrinsic case; any defects may reduce this number. In any event, clearly this line of reasoning cannot explain the very large charge densities observed. Of course, in the case of lower carrier densities, an *intrinsic* doping mechanism may become operative. Hence, an important subsidiary question is whether experimental conditions can be identified for which the intrinsic limit can be achieved.

The high sheet conductivities and carrier densities can also be explained by an

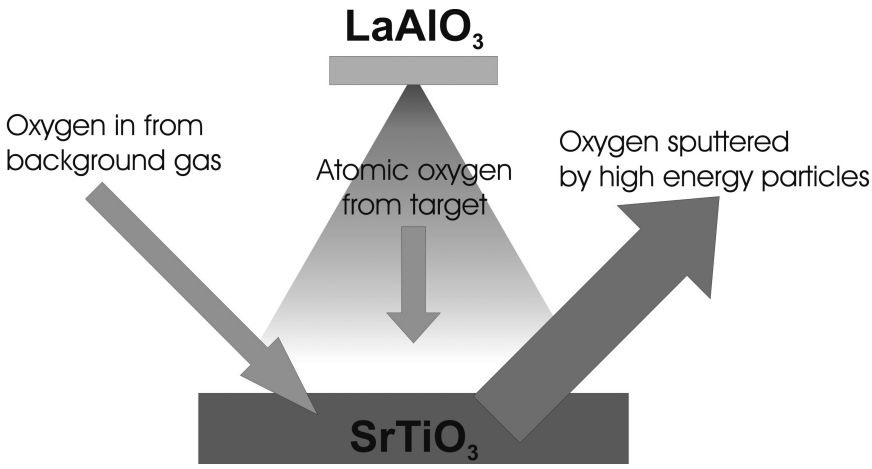

Figure 3.2: *A schematic representation of the oxygen balance during deposition of a $LaAlO_3/SrTiO_3$ interface. Oxygen is removed from the substrate due to sputtering caused by the high energy particles in the PLD plume. At the same time oxygen is supplied to the sample coming from the background gas and from the oxygen in the $LaAlO_3$ target. At low pressures (below 100 mTorr) the sputtering of oxygen will be significant, which may create enough charge carriers for the $SrTiO_3$ to become conducting.*

extrinsic doping mechanism, i.e. the charge carriers are generated in the synthesis process itself. Even the original work[1,2] mentions 10^{17} carriers cm^{-2} is rather unphysical to be explained by an electronic reconstruction. One likely cause of charge carriers are oxygen vacancies in the $SrTiO_3$ substrate,[10] an idea that is dismissed by the authors of the original work.[1,2] These vacancies can be the result of high energy particle bombardment during the PLD process used so far by all researchers in the field to make these hetero-structures. At the same time vacancies that are created will be filled by oxygen coming from the target and from the background gas. Figure 3.2 shows schematically the flow of oxygen in and out of the substrate. The number of vacancies, and therefore the number of charge carriers, that are eventually measured are a function of the deposition parameters in this case, whereas in the intrinsic case they should not vary much with deposition conditions. The growth of the $LaAlO_3$ depends on the deposition parameters as we will discuss in the next sections.

3.2 $LaAlO_3$ growth on $SrTiO_3$

All of the films reported here were grown using PLD as described previously in section 2.2.6 on page 12. During growth, RHEED was used to determine the amount of material deposited and to monitor the morphology of the samples. RHEED intensity oscillations reveal typically 120 laser pulses are required to grow a monolayer of $LaAlO_3$. We found that if atomic oxygen is introduced during deposition the growth

proceeds in a multilayer fashion, as revealed by the damping of the RHEED oscillations, and thus could complicate the transport properties. Therefore, in order to achieve high degrees of oxidation without such degradation, atomic oxygen was only introduced after deposition during sample cooling, or after taking the sample out of the system for characterization and subsequently reintroducing it for a post oxidation treatment.

Various parameters were varied from run to run. These included laser repetition rate, number of laser pulses, mask size and post-deposition treatment. The effects of these variations are important and will be discussed below. In addition, to obtain consistent results, we found it necessary to use a standard post-deposition treatment for samples grown at low oxygen pressures (10^{-6} Torr) in which the oxygen flow and the substrate temperature were quenched immediately. This treatment is believed to prevent oxygen from diffusing through the very thin $LaAlO_3$ layer during cooling; in this manner it is possible to look at the interface as grown. At higher oxygen pressures (10^{-5} Torr) such treatment was not necessary and samples were cooled down at the deposition pressure.

After deposition the samples were moved in situ into the adjacent photoemission analysis chamber. Electrical transport properties were measured as described in section 2.4.2 on page 23, taking appropriate precautions to avoid photo-induced carriers, which, depending on the conductivity of the sample, could mean the sample had to be kept in a dark environment for as long as 12 hours prior to measuring.

Two different classes of samples were prepared for physical study. The first was prepared under relatively low oxidation conditions (10^{-6} Torr of oxygen, as measured with a hot cathode ion gauge), resulting in a high number of carriers. The second was deposited and cooled at higher oxidation conditions (2×10^{-5} Torr of oxygen) resulting in a reduced carrier density. Within each class, samples with $LaAlO_3$ thicknesses of 1 and 5 ML were studied, the thinner samples were used for surface sensitive measurements.

3.3 Transport measurements

In the following sections we discuss the physical properties of these two classes of samples. In figure 3.3 on the facing page we show the temperature dependence of the resistivity for representative samples of the two classes. Together with accompanying Hall measurements, we deduce a sheet carrier density of $\sim10^{16}$ cm^{-2} and a mobility of 10^4 cm^2 V^{-1} s^{-1} (at 4 K) for the samples that are made at low pressure and a sheet carrier density of $\sim10^{13}$ cm^{-2} and a mobility of 10^3 cm^2 V^{-1} s^{-1} (at 4 K) for the samples made at higher pressure. These findings are very much in line with what has been reported by others and demonstrates directly that the oxygen pressure during deposition clearly affects the transport properties of these hetero-structures. Also, we have tested the role of the substrate alone by performing the entire deposition procedure, without depositing any $LaAlO_3$. UPS was not possible due to charging (indicating an insulating interface), and no conductivity was measured after the sample was taken out of the deposition chamber. Thus, the existence of a conducting interface depends on either the $SrTiO_3/LaAlO_3$ interface and/or the PLD process itself. Either

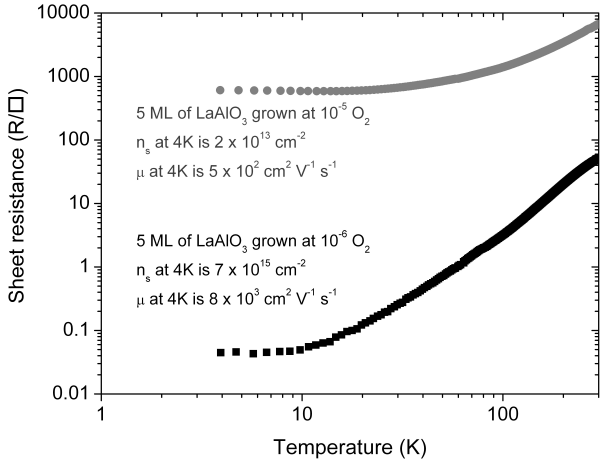

Figure 3.3: *Resistance as a function of temperature for two 5 ML thick $LaAlO_3$ on $SrTiO_3$ samples deposited at different oxygen background pressures.Some important parameters of the films at 4 K are also provided.*

way, the deposition of the $LaAlO_3$ layer is essential to the observed phenomena in these heterointerfaces.

Now we focus on the transport data for films made at low oxygen pressure (10^{-6} Torr), since these display the most extraordinary densities and mobilities. Note that these samples are also discussed in the next section on UPS measurements. The sheet resistance and Hall effect of the films were measured as a function of temperature. The results for the 1, 3, and 5 monolayer (ML) samples are shown in figure 3.4 on the next page. Note that the 1 ML thick sample was additionally oxidized after deposition whereas the other samples were not. In any event, the sheet resistance (see inset of figure 3.4) of all samples is strikingly low. Also, both the temperature dependence and the absolute values of the sheet resistance are in good agreement with those reported by Ohtomo and Hwang.[1,2] The Hall-effect data shown in the inset of figure 3.4 are also similar to those reported by those authors. The electron mobilities and sheet carrier densities derived from these data are shown in figure 3.4. The inferred sheet carrier density is 1.5×10^{16} cm^{-2} for the 1 ML thick film (post annealed in oxygen), and 7.6×10^{15} cm^{-2} for the 3 and 5 ML samples at 4 K.

Next, we turn to the interfaces made under higher oxidation conditions (10^{-5} Torr). From resistivity and Hall measurements we arrive at a reduced sheet carrier density and mobility, which, as expected, is lower than the previous case. In addition, an interesting temperature hysteresis effect is measured for the films with low carrier densities, this is shown in figure 3.5 on the following page. The amplitude of these features increases for thinner $LaAlO_3$ overlayers. So far a maximum effect has been observed for 4 unit cell layers for as deposited films (fewer than 4 layers deposited resulted in insulating samples for these deposition conditions, which has also been observed by Thiel *et al.*)[4] and the amplitude of the features also increases with magnetic field. These features

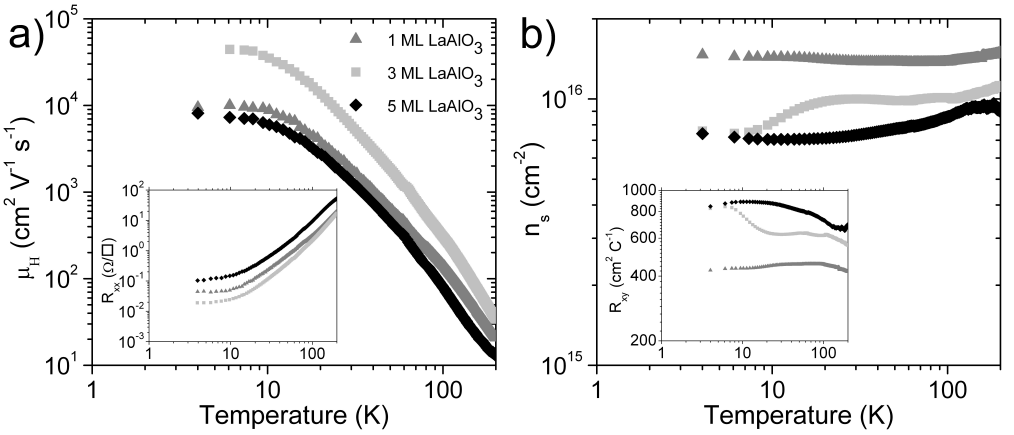

Figure 3.4: *Transport measurements and analysis of films grown at low oxygen pressure (10^{-6} Torr). a) The mobility of the charge carriers, μ_H, as a function of temperature of the one (dark grey triangles), three (gray squares) and five (black diamonds) monolayer thick films of $LaAlO_3$ on $SrTiO_3$; the one monolayer sample has been oxidized (6000 L). The sheet resistance, R_{xx}, is shown in the inset. b) The sheet carrier density for the same samples calculated from the Hall resistance data (R_{xy}, see inset).*

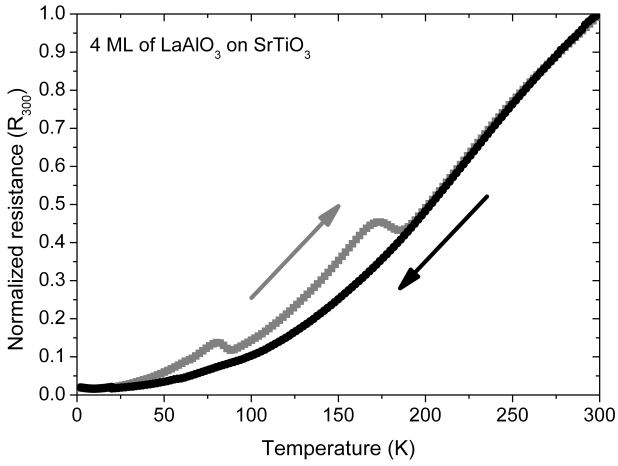

Figure 3.5: *Extra features show up in the resistance as a function of temperature plots during warmup compared to during cooldown. These increases in resistivity have been observed in multiple samples and always occur at the same temperatures.*

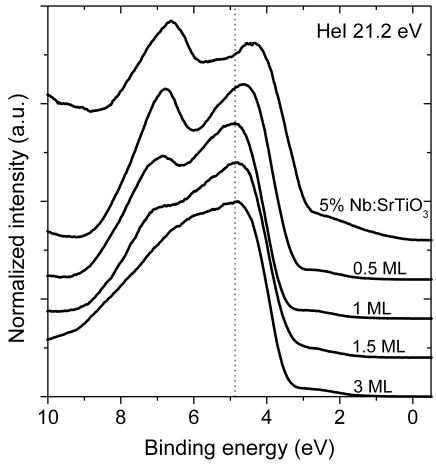

Figure 3.6: *Normalized UPS (HeI 21.2 eV) wide scans for samples with different $LaAlO_3$ thicknesses on $SrTiO_3$. A clear trend is visible as the spectrum changes from bare $SrTiO_3$ (5% Nb doped $SrTiO_3$ was used to avoid charging of the sample) to 3 ML of $LaAlO_3$. The thickness of the $LaAlO_3$ films was varied from 0.5 to 3 unit cell (UC) layers based on RHEED oscillations. The dotted line is a guide to the eye. These spectra were given an arbitrary offset for clarity.*

appear not to be stable over time: when during warm up the temperature is fixed to the maximum of one of the features, the resistance of the sample slowly drops over time until it reaches the resistance the sample had during cool down; the time over which this happens is in the order of hours. The temperature at which these features occur is always the same though.

3.4 Photoemission of buried interfaces

UPS spectra were taken from the samples made under low oxygen pressure. The transport properties of such samples were discussed in the previous section. The angle-integrated UPS data for hetero-structures with different $LaAlO_3$ layer thicknesses are shown in figure 3.6. These UPS spectra were taken for hetero-structures with $LaAlO_3$ films ranging in thickness from a half to three unit cell layers, as determined by RHEED. Note that as the thickness of $LaAlO_3$ is increased, the relative intensities of the oxygen $2p$ double-peak structure (at about 5 eV and 7 eV, respectively) change in a systematic fashion. Unfortunately, excessive charging has prevented us from taking a useful *0 ML case* spectrum, i.e. undoped $SrTiO_3$ (instead we have added a spectrum of a Nb doped $SrTiO_3$ substrate). On the other hand, this charging confirms directly that the $SrTiO_3$ is initially insulating. In addition, by extrapolation, our data seems compatible with known fully oxidized $SrTiO_3$ UPS data (see for example Henrich and Cox's book).[11]

To check the conductivity of the sample one has to measure carefully around the Fermi level to check for states being present. As an example, an expanded version of the

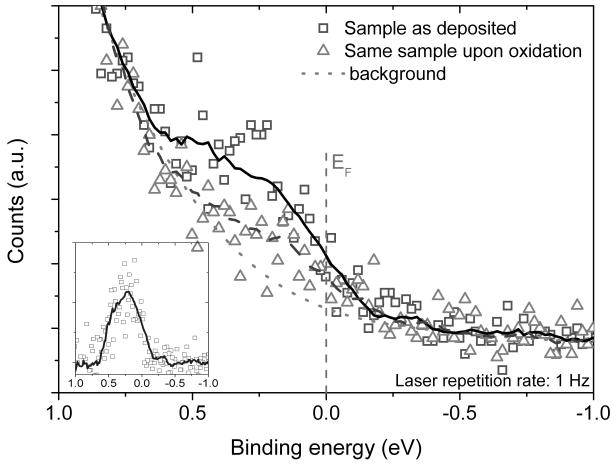

Figure 3.7: *UPS near the Fermi level. Raw UPS HeI spectra of one monolayer thick $LaAlO_3$ layer on TiO_2 terminated $SrTiO_3$ prepared at 1 Hz (open squares and fitted with a solid black line) and the same sample after exposure to ∼6000 L of oxygen (open triangles and fitted with a dashed dark grey line). Inset: 1 ML sample before oxidation upon subtraction of background indicated by the dotted gray line in the main figure.*

UPS data near the Fermi energy is presented in figure 3.7 for a representative sample, both as deposited and after additional oxidation. This particular sample had a 1 ML thick $LaAlO_3$ layer and was deposited at a repetition rate of 1 Hz in an atmosphere of 10^{-6} Torr molecular oxygen. The additional oxidation was carried out by exposing the sample to 6000 L of oxygen at 150 °C. The oxidation of the sample had no discernable effect on the UPS spectrum outside the region shown in figure 3.7.

Most importantly, the UPS data show the existence of electron states extending up to the Fermi energy, indicating the existence of a conducting charge layer at the interface (the conducting nature of this interface was confirmed directly by transport measurements presented below). Moreover, the size of this density of states is sensitive to the oxidation history of the sample, being lowered by further oxidation. At a more quantitative level, the photoemission signal at the Fermi level for the 1 ML sample is roughly 1000 times smaller than the O $2p$ peak. This ratio is comparable to that measured in photoemission for $Sr_{0.95}La_{0.05}TiO_3$, confirming a high carrier density at the surface.[12] Earlier work by Takizawa *et al.*[13] also revealed high densities of states observed by photoemission for related samples of $LaTiO_3/SrTiO_3$ hetero structures prepared at low oxidation conditions.

In order to compare the resulting density of states produced using various deposition conditions, we subtracted from the UPS data a background function given by the overall trend in the data from -3 eV to +2 eV (see the gray dotted line in figure 3.7 for the sample shown). An example of this difference spectrum is shown as the inset in figure 3.7 for the case of one monolayer deposited at 1 Hz in 10^{-6} Torr of oxygen. Finally, in order to better statistically average the data, we integrated the area under

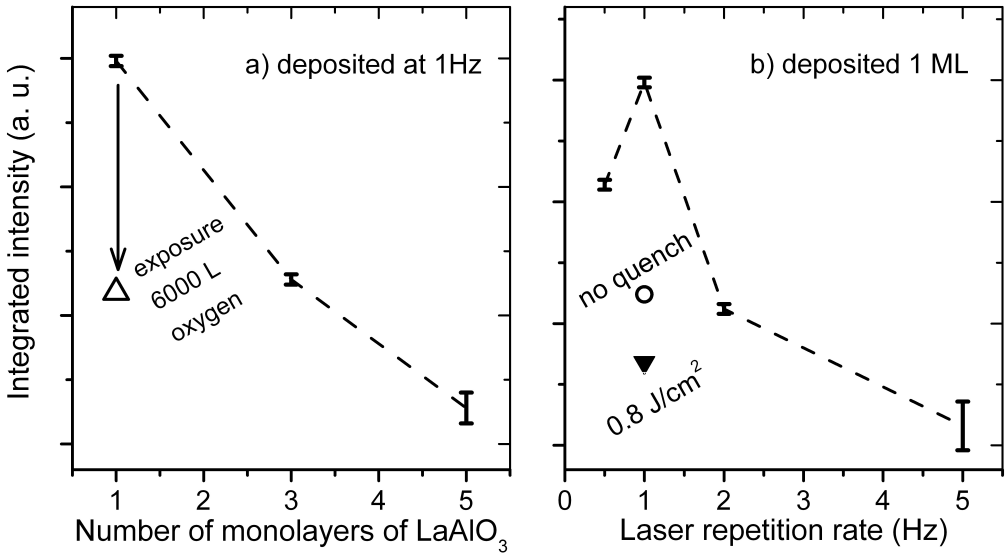

Figure 3.8: *Analysis of UPS data for different samples. a) Comparison of the UPS signal near E_F for different $LaAlO_3$ film thicknesses by integration of the difference intensity (for example from figure 3.7 on the facing page), the error bars indicate the statistical error, the connecting line is a guide to the eye, the triangle is the value found for the 1 Hz, 1 ML sample after exposure to ∼6000 L of oxygen. b) Comparison of the integrated difference intensity as a function of the laser repetition rate (1 ML — 1 Hz, 2 Hz, 5 Hz) the error bars indicate the statistical error, the connecting line is a guide to the eye; the open circle is the value found for a sample where the pressure quench described in the text is not applied, the solid square represents the value found for a sample made when a laser energy of 0.8 J cm^{-2} per pulse is used.*

the difference spectra. Physically, this integrated density of states corresponds to the number of carriers per unit volume in the layer. These values for various samples are compared in figure 3.8.

In figure 3.8a, we see that the integrated density of states at the surface decreases monotonically with the thickness of the $LaAlO_3$ for otherwise identical samples. This is consistent with the states existing at the interface and the usual escape depth arguments, i.e., the fall off is roughly exponential with a characteristic mean free path of ∼8 Å. Samples with thicknesses greater than 5 ML yielded no appreciable photoelectron signal, and for an order of magnitude greater thicknesses, insulating behavior and its associated charging effects prevented UPS study.

Figure 3.8b shows the effect of varying the PLD laser repetition rate. The data suggest an optimal repetition rate of ∼1 Hz for the number of interface states generated. Repetition rates over 5 Hz did not show any discernable UPS signal.

Finally we discuss some special cases. When exposing the 1 ML film deposited at 1 Hz to 10^{-5} Torr oxygen for ten minutes at 150 °C the spectral weight at the Fermi energy is reduced (see figure 3.7 on the preceding page and figure 3.8a (open triangle)).

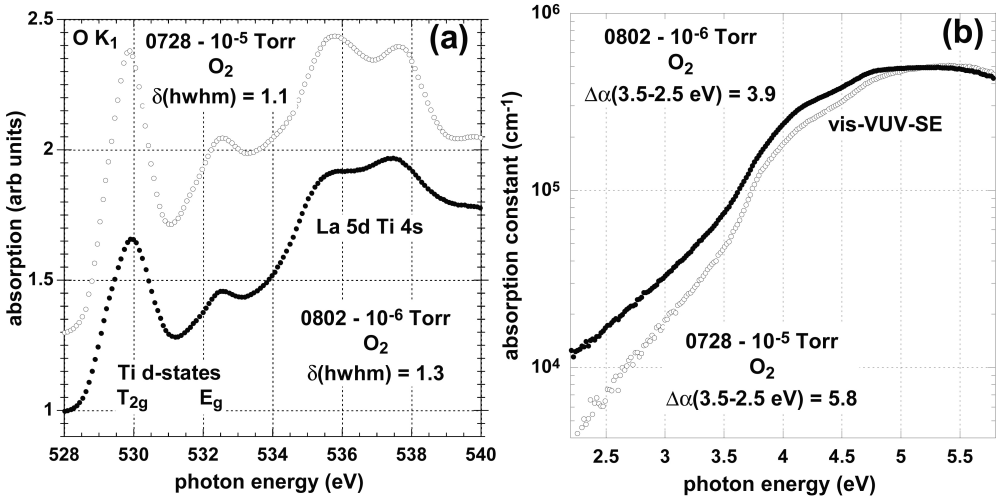

Figure 3.9: *(a) NEXAS O K_1 of sample 0728 (deposited at 10^{-5} Torr) and sample 0802 (deposited at 10^{-6} Torr) (b) vis-VUV Spectroscopic Ellipsometry absorption constant, α, spectrum of the same samples as in (a).*

Signal reduction is also observed when the pressure quench is not applied, and thus the sample is cooled in 10^{-6} Torr of oxygen (figure 3.8b, open circle) or similarly when the laser energy per pulse is lowered from 1.2 to 0.8 J cm^{-2} (Figure 3.8b, solid triangle). Samples grown at higher oxygen pressure (10^{-5} Torr) show no discernable signal at the Fermi level.

Other spectroscopic techniques have been applied to the samples with the help of Gerry Lucovsky at North Carolina State University. Details on NEXAS and vis-VUV-SE are described elsewhere.[14,15] The NEXAS O K_1 edge absorption results are shown in figure 3.9a. As is evident, the Ti $3d$ and $4s$ features in the sample prepared at high oxidation conditions are significantly stronger relative to the La $5d$ features. The half-width-at-half-maximum (hwhm), at the low energy side of the Ti T_{2g} feature relative to TiO_2 is smaller for the sample prepared at high oxidation conditions compared with the sample at low oxidation conditions. This is indicative of decrease in the density of oxygen vacancies or alternatively Ti^{3+} bonding. The presence of oxygen defects broadens all features in the NEXAS spectrum and therefore affect all peaks in the spectrum. The absorption constants, α, extracted from vis-VUV-SE measurements in figure 3.9b support the interpretation of the of the O K_1 spectra. The band edge defect state features between 2.3 and 3.5 eV at the onset on conduction band Ti $3d$ absorption edge, are stronger in the sample deposited at the lower oxygen pressure consistent with a higher concentration of O-atom vacancies, or equivalently Ti^{3+} defect sites. The beauty of these data is that they make a direct, spectroscopic connection to the presence of Ti^{3+} and therefore oxygen vacancies.

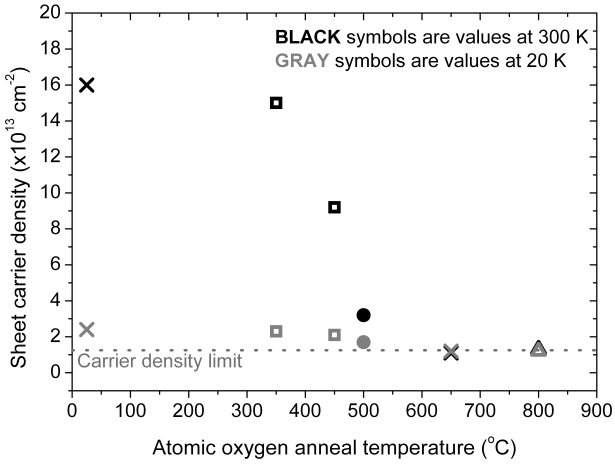

Figure 3.10: *Sheet carrier densities at 20 K (gray symbols) and 300 K (black symbols) as a function of annealing temperature in 600 W atomic oxygen, for samples made at 10^{-5} Torr of O_2 600 W of atomic oxygen corresponds to $\sim 10^{17}$ oxygen atoms cm^{-2} s^{-1}. The latter value was taken after Ingle et al.[16] who worked on the same system in our laboratory. The values at 25 °C indicate the as deposited samples. The different symbol shapes indicate different samples made under similar conditions: two made at Stanford (circles and triangles), the other two made at the University of Twente (crosses and squares). Sample thickness ranges from 5 to 26 ML.*

3.5 Annealing experiments

We turn now to the question of how low the carrier density can be achieved at these interfaces. In order to address this question, we annealed various samples in atomic oxygen at elevated temperatures (350–800 °C). The results of these measurements are shown in figure 3.10. To exclude the possibility of introducing interstitial oxygen, we cooled the samples below 250 °C in vacuum, after annealing in vacuum for one hour at that temperature. The samples annealed up to 800 °C show a reduced sheet carrier density: $1.2–1.3\times10^{13}$ down from 2.3×10^{13} at 4 K, whereas the mobility remains unchanged. Most strikingly, for anneals above 500 °C, the carrier sheet density appears to settle at a lower limit value and becomes independent of temperature, which is consistent with the findings of the Augsburg group.[4]

3.6 Carrier distribution model

Regardless of the mechanism that created the carriers, there remain the questions of what causes the high mobility, what causes the temperature dependence, and where the carriers reside. The carriers cannot be distributed uniformly over the bulk unless there was an equal density of compensating charged donors and based on bulk data for $SrTiO_3$ their the mobility would be much lower than we observe.[17] The other extreme,

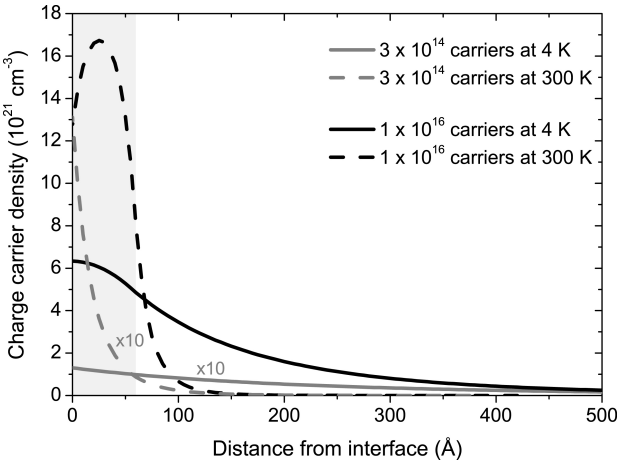

Figure 3.11: *Calculations of the electron density as a function of distance from the interface for two different total numbers of electrons per cm^2 (3×10^{14} and 1×10^{16}) at two different temperatures. The shaded gray area indicates the location of the oxygen vacancies for the high carrier density case, 10^{16}, for the low carrier density case no oxygen vacancies were assumed, hence the different slopes at the interface.*

for which there is no supporting evidence, was they occupied surface bands at the interface. We see no reason to suggest such bands exist for this type of interface. The more plausible scenario is that this is a kind of modulation doping where a high mobility conducting layer results because the carriers are separated in space from the charged vacancies due to their thermal distribution in space.

To support this scenario, we have modeled the distribution of the electrons in the $SrTiO_3$. We assume that the vacancies are distributed homogeneously in a narrow region of depth 6 nm in the $SrTiO_3$ at the interface. We assume a Thomas-Fermi distribution of the carriers, which is valid when $V(x) < k_B T$, where $V(x)$ is the potential at depth x, and therefore appropriate for the cases that follow. Using this source distribution, we solve Poisson's equation to obtain the potential and charge density as a function of depth in the $SrTiO_3$, which is linked to the carrier density at a depth x by $n(x) = -n_0 V(x)^{3/2}$, with $n_0 = (2m/h^2)^{3/2}/3\pi^2$. The outcomes for both a high (10^{16}) and the low (10^{14}) interface carrier density cases are shown in figure 3.11 at 300 and 4 K.

The calculations show that the electrons move into the material over 50 nm at low temperatures and that this depth decreases dramatically at high temperatures (see dotted lines in figure 3.11) — a rather counterintuitive result. The reason for this unusual behavior is the very large and strongly temperature dependent dielectric constant of $SrTiO_3$, some 20,000 at low temperature compared to 300 at room temperature.[18] Note that the values for the dielectric constant taken here are for zero field and stoichiometric $SrTiO_3$. The real values might deviate but would not change our qualitative

conclusion. It also offers an explanation of the high mobility that is measured especially for the samples deposited at low pressures: the carriers are moved away from the defects into the pristine $SrTiO_3$ where they are highly mobile. It also explains the absence of clear Shubnikov-de Haas oscillations since the carrier density varies with depth.

3.7 Multilayers of $LaTiO_3$ and $SrTiO_3$

For a related materials system, the interface between $LaTiO_3$ and $SrTiO_3$, theory predicts interesting conducting and magnetic behavior. Okamoto, Millis, and Spaldin [6,19] expect the interface to conduct and display magnetism, properties that do not arise in the constituent oxides themselves. $LaTiO_3$ is normally antiferromagnetic and a Mott insulator, $SrTiO_3$, on the other hand, is a band insulator. These authors simulate a $LaTiO_3$ layer of several MLs thick confined between two very thick layers of $SrTiO_3$. The magnetic behavior calculated depends on the thickness of the $LaTiO_3$ layer and on the intraband Coulomb interaction, U, between the electrons. This last parameter is the main uncertainty in such calculations, because the value for U is not known from measurements. The expected magnetism, for layers thicker than 1 ML, ranges from paramagnetic at low values of U ($0 < U < 3$ eV) to antiferromagnetic at intermediate values of U ($3 < U < 5$ eV) and ferromagnetic at large values of U ($U > 5$ eV). For a layer thickness of 1 ML they calculate paramagnetic behavior for $U < 3$ and ferromagnetic behavior for $U > 3$. Hamann, Muller, and Hwang [20] also predict conductivity in this system, but do not comment on possible magnetic effects. Popovic and Satpathy [21] do not predict ferromagnetic behavior. They expect that the antiferromagnetism of the $LaTiO_3$ prevails at layer thicknesses of more than 1 ML, while for the 1 ML case no magnetism is expected.

Verifying these predictions experimentally is not straightforward due to complications in the growth of $LaTiO_3$. Ohtomo *et al.* [22] find using PLD that $LaTiO_3$ is only stable when grown under low oxygen pressures (below 10^{-4} Torr), whereas at higher pressures $La_2Ti_2O_7$ is the more stable phase. For optimal growth they suggest 5×10^{-6} Torr O_2 and a temperature of 700 °C. They note that as the oxygen pressure during growth is lowered the samples become more conductive, very much in line with our own notion of the creation of oxygen vacancies, an effect which is acknowledged in literature. [23,24] Using TEM analysis they also looked at stacking faults and found that those were absent only in samples below 6 ML thick. The stability of the $LaTiO_3$ can be enhanced by also growing $SrTiO_3$ on top of it, so that stabilizing strain is applied from both sides. Shibuya *et al.* [25] and Mihara *et al.* [26] show that even a 1 ML film shows conductivity in this case. They grow superlattices of $LaTiO_3$ and $SrTiO_3$ and demonstrate when the $SrTiO_3$ layer thickness is increased smoother films result and the lattice constant of the superlayers increases with the ratio of $LaTiO_3$ to $SrTiO_3$. Takizawa and coworkers [13] have also created such interfaces and measure a finite density of states at the Fermi level with PES in much the same way as was shown earlier in this chapter for the $LaAlO_3$ interface. To exclude oxygen vacancies as the cause of the conductivity they anneal their samples in molecular oxygen at 500 °C for an

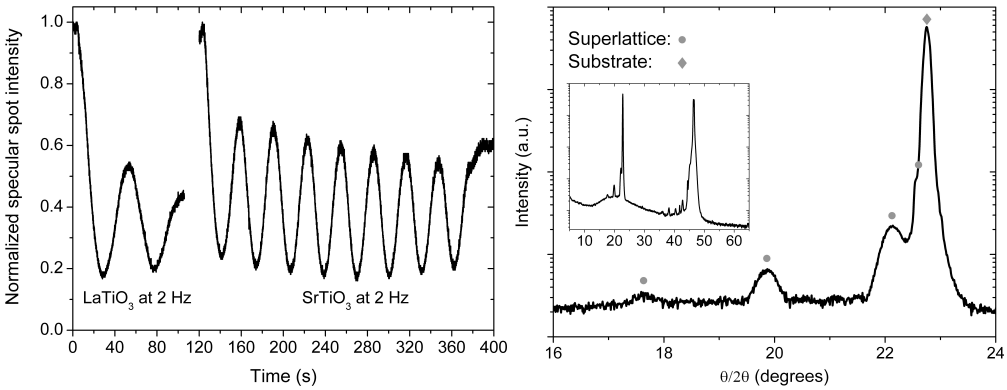

Figure 3.12: *On the left: typical RHEED oscillations for the deposition of $LaTiO_3/SrTiO_3$ multilayers, in this case 2 MLs of $LaTiO_3$ and 8 MLs of $SrTiO_3$ repeated five times. Typically around 100 pls were needed for 1 ML of $LaTiO_3$ and around 60 pls for a ML of $SrTiO_3$. The oscillations are damped for $LaTiO_3$ due to roughening of the surface. For $SrTiO_3$ they are only slightly damped, the initial drop in the figure for the first ML is due to the difference in optimal RHEED reflection angles between $LaTiO_3$ and $SrTiO_3$. The part of the curve between the two $LaTiO_3$ and the eight $SrTiO_3$ has been omitted due to realignment of the RHEED pattern. On the right: the XRD $\theta/2\theta$ spectrum of the same sample showing multilayer peaks (gray solid circles) and confirming the enlargement of the out-of-plane lattice parameter with respect to the substrate (gray solid diamond). The inset shows a wider range and indicates no other phases were formed, the additional sharp peaks are from $k\beta$ radiation.*

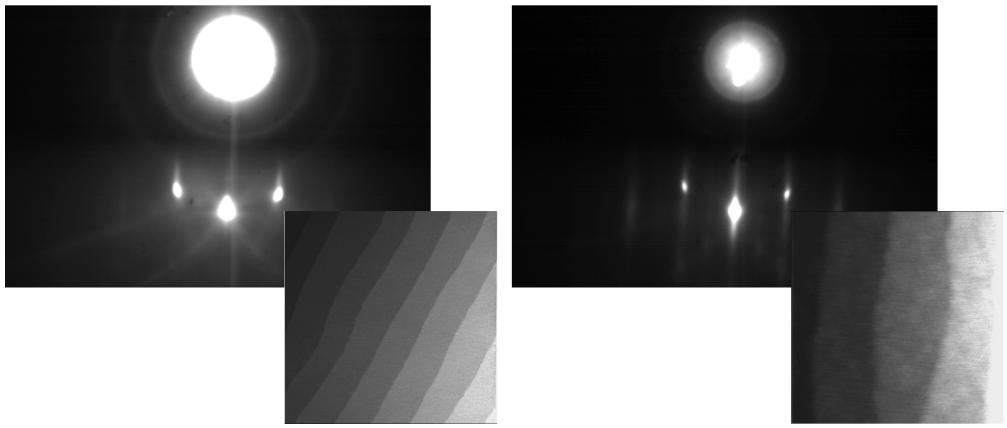

Figure 3.13: *RHEED spectra before (left) and after (right) deposition of $LaTiO_3/SrTiO_3$ multilayers, in this case 1 MLs of $LaTiO_3$ and 9 MLs of $SrTiO_3$ repeated five times. After deposition the patterns shows no 3D spots and still displays Kikuchi lines, indicative of very smooth and well ordered layers. The 1×1 μm AFM images, which for the pristine substrate is of a different, representative sample, show smooth terraces and unit cell high steps.*

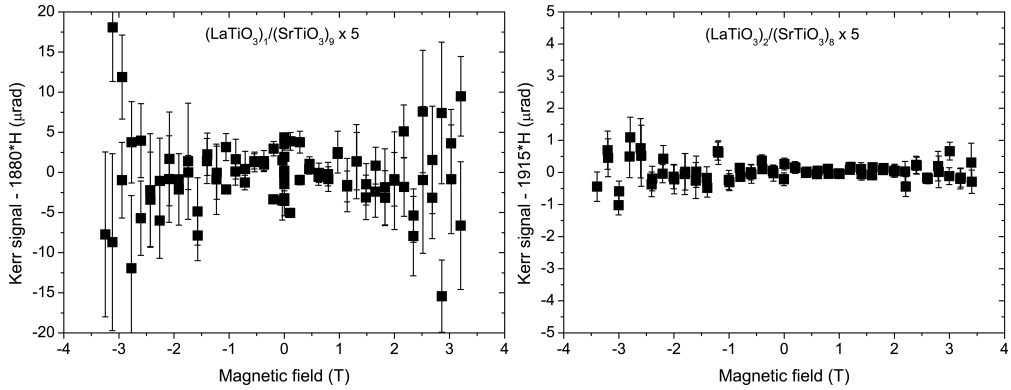

Figure 3.14: *Hysteresis loops of the $(LaTiO_3)_1/(SrTiO_3)_9$ on the left and the $(LaTiO_3)_2/(SrTiO_3)_8$ on the right. Neither shows a clear ferromagnetic signal.*

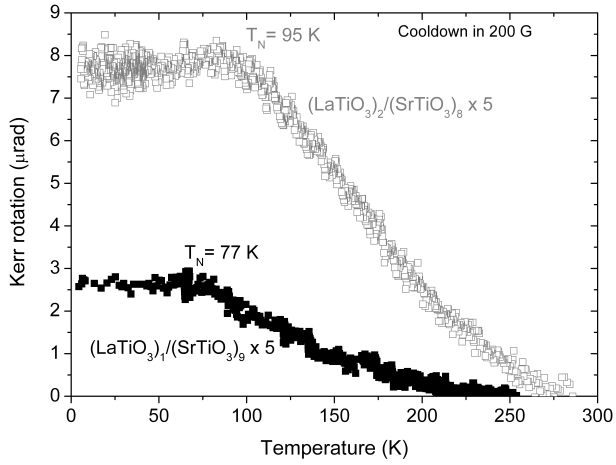

Figure 3.15: *Kerr signal during cooldown in a magnetic field of both samples mentioned in the text. Both show a magnetic transition and the transition temperatures are given with the curves.*

hour, but the annealing experiments that were done on the $LaAlO_3$ (discussed before in this chapter) suggest that this temperature might be too low to oxidize the sample sufficiently.

In order to verify the theoretical claims and the experimental findings of other groups, we have grown a number of superstructures of $LaTiO_3$ and $SrTiO_3$. The two samples that will be discussed here are build up of units of $(LaTiO_3)_1/(SrTiO_3)_9$ and $(LaTiO_3)_2/(SrTiO_3)_8$, both repeated 5 times at 700 °C in 10^{-5} Torr O_2. An example of the RHEED specular spot intensity during deposition is given in figure 3.12 on page 40. After deposition the RHEED spectrum showed no 3D spots, and some Kikuchi lines were still visible indicating that the samples were smooth and well ordered, which was confirmed by AFM, as is shown in figure 3.13 on page 40. In order to avoid oxygen vacancies a procedure similar to the $LaAlO_3$ samples was followed: samples were exposed to atomic oxygen after deposition and were cooled down in it to 250 °C. The samples were then annealed for one hour in vacuum at 250 °C to remove any interstitial oxygen. This procedure has no discernable effect on the RHEED spectra. The samples were examined with XRD and the $\theta/2\theta$ as well as the reflectivity measurements confirm the creation of the expected superlattices. For superlattices with $LaTiO_3$ layers thicker than 2 ML the growth was found to be less controlled, probably due to the creation of stacking faults, which resulted in rougher samples and interfaces. For that reason those samples have been excluded from this analysis.

Both samples were found to be insulating at room temperature and no conductivity was measured down to 2 K. No ferromagnetic hysteresis loop was measured at 4 K on neither samples as shown in figure 3.14 on the previous page, indicating no ferromagnetic order down to 4 K. A linear contribution from the substrate and optical components has already been subtracted from the hysteresis loops. To study the temperature dependence of susceptibilities of the multilayers, we conducted Kerr measurements in a finite small magnetic filed of 200 G as a function of temperature. The results are visible in figure 3.15 on the preceding page. The $(LaTiO_3)_1/(SrTiO_3)_9$ sample showed a paramagnetic response above 77 K and the Kerr signal remains constant below that temperature, indicating a a faint transition to an antiferromagnetic state with out-of-plane antiferromagnetic moments around 77 K (compared to the bulk Néel temperature of $LaTiO_3$ which is around 135 K). On the $(LaTiO_3)_2/(SrTiO_3)_8$ superstructure a transition to an antiferromagnetic state is visible at a higher temperature of 95 K.

3.8 Discussion and conclusions

The summary of our data presented in table 3.1 on the next page confirms the strong dependence of the conducting layer properties at these $SrTiO_3/LaAlO_3$ interfaces on the oxidation conditions under which the samples were made.

To summarize the results of the photoemission spectroscopy: the experimental results presented above strongly suggest that the origin of this high charge density is associated with oxygen vacancies in the $SrTiO_3$, despite the fact that prior to deposition such vacancies are demonstrably not present. The UPS data confirms explicitly the

Prep. cond. (pO_2 in Torr)	Thickness [ML $LaAlO_3$]	n_s [cm^{-2}] 4K/300K	μ [$cm^2\ V^{-1}s^{-1}$] 4K/300K
10^{-6}	1	...	...
10^{-6} + 6000 L*	1	2×10^{16} / 2×10^{16}	1×10^{4} / 5
10^{-6}	5	2×10^{16} / 2×10^{16}	1×10^{4} / 5
10^{-5}	1	Not conducting	Not conducting
10^{-5}	5	2×10^{13} / 2×10^{14}	3×10^{2} / 4

Prep. cond. (pO_2 in Torr)	Thickness [ML $LaAlO_3$]	UPS (relative int. at E_F)	NEXAS δ(hwhm) Ti_{2g}**	Vis-VUV-SE Δ(3.5-2.5)***
10^{-6}	1	100%	...	...
10^{-6} + 6000 L*	1	40%	1.3	3.9
10^{-6}	5	...	...	...
10^{-5}	1	...	1.1	5.8
10^{-5}	5	...	...	...

Table 3.1: *A comparison between samples of different thicknesses made at low and high pressures. In the top panel the most important parameters from the transport measurements are listed: the charge carrier density at 4 K and 300 K and their mobility at those temperatures. In the bottom panel are the results of the spectroscopic techniques: the integrated area under the curve from the UPS spectra at the Fermi level, the width of the Ti2g peak in the NEXAS spectra, and the change in α in the Vis-VUV-SE spectra.*
** 1 ML sample prepared at 10^{-6} Torr of O_2 and after in situ exposure to 10^{-6} Torr of O_2 for 10 minutes at 150 °C;*
*** ratios of hwhm of T_{2g} d-state relative to TiO_2;*
**** ratios of α between 3.5 and 2.5 eV.*

existence of states at the Fermi level and that the number of states can be reduced by oxidation. The various dependencies of the results on deposition conditions are consistent with this view. A natural interpretation of these data is that competing processes are present. For example, deposited material at the surface may need some time to crystallize, which we estimate to be on the order of one tenth of a second,[27] and for the lowest repetition rates re-oxidation occurs. Another is the sputtering of oxygen from the surface being balanced by growth of the $LaAlO_3$ over-layer and anion vacancies formed deeper in the $SrTiO_3$[28] through oxygen diffusion. Similarities in transport between the $LaAlO_3/SrTiO_3$ interface and low energy Ar sputtering were found by Reagor and Butko[29] and suggest particles generated in the PLD process can indeed cause the $SrTiO_3$ to become conducting. Further evidence for oxygen vacancies, and a discussion on suppressing them, was presented here in the form of NEXAS and vis-VUV-SE measurements. Additional evidence for oxygen vacancies presented by Kalabukhov *et al.*[10] based on cathode-luminescence.

The effect of oxygen vacancies is clearly reflected in the transport measurements, where sample properties depend on deposition conditions. For samples made at low

oxygen pressures we showed remarkably high sheet carrier densities. The inferred mobilities ($\sim 10^4$ cm^2 V^{-1} s^{-1}) at 4 K are also high, suggesting that the charge donors of the interface carriers are well removed from the interface region itself, as in modulation doping in semiconductor hetero-structures. For samples made at higher oxygen pressure we find temperature hysteresis. Extra features in the resistivity were shown to appear at fixed temperatures, which tend to relax slowly over time. These increases occur at the same temperatures at which increases in the dielectric constant are observed.[30,31] Although they have observed these dielectric relaxations in La doped $SrTiO_3$, Yu and coworkers[30] show that they are related to oxygen vacancies in the sample. Those authors anneal in oxygen and/or air at high temperatures (1100 °C) and find the relaxations disappear. We cannot anneal at such high temperatures since there is a high possibility of damaging the interface. Similar relaxation times have been observed by Thiel *et al.*[4] in a field effect structure based on these hetero-structures.

In that same paper a critical thickness was observed for a sample to be conductive: samples with a $LaAlO_3$ layer thickness of fewer than 4 ML were found to be insulating. Interestingly, the hysteresis we observe in the conductance also appears to be maximal for samples with an over-layer thickness of 4 ML. What causes this critical thickness has not been determined yet. Note however that if one assumes an intrinsically doped interface (due to the polarized nature of the $LaAlO_3$),[1,2] the potential that is created can promote electrons into the conduction band. For this effect to occur it is necessary that the potential over the $LaAlO_3$ layer is larger than its bandgap. We calculated that the jump in potential per unit cell is $\sim$3.8 eV, from $\Delta V = 8\pi e^2/\varepsilon a$, which is quite large compared to the bandgap of 5.6 eV. This would mean that after two unit cells there is enough of a potential to put electrons in the conduction band. For real films more layers are probably needed due to the presence of defects. Note that if some oxygen vacancies are present in the $SrTiO_3$ the diverging potential in the $LaAlO_3$ is attenuated due to the charge already being present in the $SrTiO_3$. For the samples grown at low pressures the high carrier density is present even with only 1 ML of $LaAlO_3$, effectively ruling the charge transfer mechanism out as the source of the carriers under these growth conditions.

Even though we see signs of oxygen vacancies in all our films, their density can be strongly reduced by choosing the correct deposition conditions. This could mean for sufficiently low oxygen vacancy densities two mechanisms could be at play creating charge carriers (oxygen vacancies and the charge transfer due to the polarize nature of the $LaAlO_3$), which seem to balance one another. Their effects add up in the regime where both mechanisms of the same order of magnitude. From our data we cannot tell at which electron density this is the case. However, Brinkman *et al.*[5] show that the properties of the interface layers continue to change when the deposition pressure is increased up to 10^{-3} Torr. The features that show up in the resistivity measurement, which are linked to oxygen vacancies, do not disappear after atomic oxygen annealing and suggest vacancies are still present even at such reduced carrier densities. It therefore seems likely the carriers are produced by an *extrinsic* doping mechanism (oxygen vacancies) at all deposition pressures.

We have also performed measurements on a related materials system, the interface between $LaTiO_3$ and $SrTiO_3$, for which theory predicts interesting conducting and

magnetic behavior. The magnetic measurements prove the interaction between the two materials is less than would be expected based on some of the theoretical predictions. On the contrary, the $LaTiO_3$ seems to retain its antiferromagnetism even though it is just one monolayer thick. The transition temperature is suppressed for such thin layers, probably due to a finite size effect as described by Ambrose and Chien.[32] A note of caution is required however, since the calculations are performed for interfaces at 0 K and the measurements were performed at 4 K. Even so, it is unlikely a ferromagnetic phase will form at lower temperatures, when an antiferromagnetic one is stable at higher temperatures already.

To conclude, measurements of the electronic properties of the interfaces created by depositing $LaAlO_3$ on $SrTiO_3$ show electronic properties similar to the remarkable values found originally by Ohtomo and Hwang.[1,2] Also, UPS spectra show states at the Fermi level, indicating a conducting interface. The number of these states is lowered when the sample is oxidized, insinuating oxygen vacancies play an essential role in supplying the charge carriers. This is further confirmed by NEXAS and vis-VUV-SE measurements which show more Ti^{3+} for samples made at lower pressures. We argue that the vacancies are created by the PLD process itself where relatively high energy particles sputter off oxygen. To reduce the number of vacancies we have annealed samples in atomic oxygen, which reduces the number of carriers, but keeps their mobility the same.

The location of the charge carriers changes dramatically as a function of temperature. We have calculated the potential and the carrier density in the $SrTiO_3$ to determine where the electrons are located as a function of distance from the interface. We have also calculated the electrons move into the pristine $SrTiO_3$ over large distances mainly due to the high dielectric constant of $SrTiO_3$ at low temperatures.

Bibliography

1. A. Ohtomo and H. Y. Hwang, Nature **427**, 423 (2004).

2. A. Ohtomo and H. Y. Hwang, Nature **441**, 120 (2006).

3. M. Huijben, G. Rijnders, D. H. A. Blank, S. Bals, S. V. Aert, J. Verbeeck, G. V. Tendeloo, A. Brinkman, and H. Hilgenkamp, Nature Materials **5**, 556 (2006).

4. S. Thiel, G. Hammerl, A. Schmehl, C. W. Schneider, and J. Mannhart, Science **313**, 1942 (2006).

5. A. Brinkman, M. Huijben, M. van Zalk, J. Huijben, U. Zeitler, J. C. Maan, W. G. van der Wiel, G. Rijnders, D. H. A. Blank, and H. Hilgenkamp, Nature Materials **6**, 493 (2007).

6. S. Okamoto, A. J. Millis, and N. A. Spaldin, Physical Review Letters **97**, 056802 (2006).

7. W. Siemons, G. Koster, H. Yamamoto, W. A. Harrison, G. Lucovsky, T. H. Geballe, D. H. A. Blank, and M. R. Beasley, Physical Review Letters **98**, 196802 (2007).

8. W. Siemons, G. Koster, H. Yamamoto, T. H. Geballe, D. H. A. Blank, and M. R. Beasley, Physical Review B **76**, 155111 (2007).

9. W. A. Harrison, *Elementary Electronic Structure* (World Scientific, 1999).

10. A. Kalabukhov, R. Gunnarsson, J. Borjesson, E. Olsson, T. Claeson, and D. Winkler, Physical Review B **75**, 121404 (2007).

11. V. E. Henrich and P. A. Cox, *The Surface Science of Metal Oxides* (Cambridge University Press, 1994).

12. Y. Aiura, H. Bando, I. Hase, Y. Nishihara, Y. Haruyama, T. Shimizu, and H. Suzuki, Journal of Electron Spectroscopy and Related Phenomena **78**, 199 (1996).

13. M. Takizawa, H. Wadati, K. Tanaka, M. Hashimoto, T. Yoshida, A. Fujimori, A. Chikamatsu, H. Kumigashira, M. Oshima, K. Shibuya, et al., Physical Review Letters **97**, 057601 (2006).

14. R. M. A. Azzam and N. M. Bashara, *Ellipsometry and Polarized Light* (Elsevier, 1977).

15. G. Lucovsky, C. Fulton, Y. Zhang, Y. Zou, J. Luning, L. Edge, J. Whitten, R. Nemanich, H. Ade, D. Schlom, et al., IEEE Transactions on Device and Materials Reliability **5**, 65 (2005).

16. N. J. C. Ingle, R. H. Hammond, M. R. Beasley, and D. H. A. Blank, Applied Physics Letters **75**, 4162 (1999).

17. H. P. R. Frederikse and W. R. Hosler, Physical Review **161**, 822 (1967).

18. H.-M. Christen, J. Mannhart, E. J. Williams, and C. Gerber, Physical Review B **49**, 12095 (1994).

19. S. Okamoto and A. J. Millis, Physical Review B **70**, 075101 (2004).

20. D. R. Hamann, D. A. Muller, and H. Y. Hwang, Physical Review B **73**, 195403 (2006).

21. Z. S. Popovic and S. Satpathy, Physical Review Letters **94**, 176805 (2005).

22. A. Ohtomo, D. A. Muller, J. L. Grazul, and H. Y. Hwang, Applied Physics Letters **80**, 3922 (2002).

23. Y. Taguchi, T. Okuda, M. Ohashi, C. Murayama, N. Môri, Y. Iye, and Y. Tokura, Physical Review B **59**, 7917 (1999).

24. F. Lichtenberg, D. Widmer, J. G. Bednorz, T. Williams, and A. Reller, Zeitschrift für Physik B **82**, 211 (1991).

25. K. Shibuya, T. Ohnishi, M. Kawasaki, H. Koinuma, and M. Lippmaa, Japanese Journal of Applied Physics **43**, L1178 (2004).

26. T. Mihara, K. Shibuya, T. Ohnishi, H. Koinuma, and M. Lippmaa, Thin Solid Films **486**, 63 (2005).

27. G. Koster, G. J. H. M. Rijnders, D. H. A. Blank, and H. Rogalla, Applied Physics Letters **74**, 3729 (1999).

28. J. G. López, D. H. A. Blank, and H. Rogalla, Applied Surface Science **127–129**, 1011 (1998).

29. D. W. Reagor and V. Y. Butko, Nature Materials **4**, 593 (2005).

30. Z. Yu, C. Ang, and L. E. Cross, Applied Physics Letters **74**, 3044 (1999).

31. E. Iguchi and K. J. Lee, Journal of Materials Science **28**, 5809 (1993).

32. T. Ambrose and C. L. Chien, Physical Review Letters **76**, 1743 (1996).

Chapter 4

Thin films of $SrRuO_3$

4.1 Introduction

Thin films of the perovskite $SrRuO_3$ have attracted considerable interest due to their low room temperature resistivity and small lattice mismatch with a range of functional oxide materials.[1,2,3] In addition they exhibit *bad metal* behavior, which is one of the unsolved problems of contemporary condensed matter physics, show signs of electron correlation in the material, and are ferromagnetic below a temperature of 160 K. For these reasons thin films of $SrRuO_3$ are of great current interest, both from the materials science and the physics point of view.

In this chapter we will focus on a number of materials science issues related to $SrRuO_3$ thin films, which will lead to a discussion of the physics of $SrRuO_3$. One of the questions which inspired this work was: why do $SrRuO_3$ films grow untwinned even though the bulk crystal structure at the growth temperature is cubic? To answer this question we have performed high temperature x-ray diffraction studies to determine the crystal symmetry at the growth temperature and show that the structural phase transitions occur at different temperatures in epitaxially grown films than in bulk material. The tetragonallity of the unit cell at the growth temperature offers an elegant explanation for the formation of untwinned films.

Another intriguing materials science issue requiring clarification was the importance of the technique used to grow the films. The best transport properties are found in film grown by MBE, whereas films grown by PLD are always of lower quality. The crystallinity of the samples grown by either technique is extremely high and cannot be an explanation for the differences observed. To solve this problem we have examined the degree of correlation or, what turns out to be equivalent, a deficiency of ruthenium in the various films, which is due to oxygen activity during growth. This way we demonstrate a direct link between correlation in and the transport properties of the films.

In the last part of this chapter we will turn to the magnetic properties of $SrRuO_3$. $SrRuO_3$ is an itinerant ferromagnet and becomes ferromagnetic in bulk material below a temperature of 160 K. When $SrRuO_3$ films are to be used in devices it is important to

know how thin layers can be made while still displaying the same magnetic properties. We found an interesting phase transition in the magnetic properties as a function of thickness and will offer explanations as to its origin. Before proceeding to the results some background information on structural, electronic, and magnetic properties will be given in the following sections.

The research described in this chapter has been published in Physical Review B and Applied Physics Letters.[4,5]

4.1.1 Crystal structure

In order for $SrRuO_3$ to grow coherently on a single crystal, substrate matching of layer in-plane lattice parameter to that of a substrate is required. The mismatch between in-plane lattice parameters of a film and the substrate introduces strain which affects the structural and electrical properties of the $SrRuO_3$ layer.

X-ray and neutron diffraction studies show bulk $SrRuO_3$ at room temperature possesses an orthorhombic *Pbnm* symmetry with a = 5.5670 Å, b = 5.5304 Å, and c = 7.8446 Å, similar to other ABO_3 perovskite compounds, and is isostructural with $GdFeO_3$.[6] The orthorhombic phase can be obtained by rotation of BO_6 (RuO_6) octahedra counterclockwise about the $[010]_{cubic}$ and $[001]_{cubic}$ directions and clockwise rotation about the $[100]_{cubic}$ direction of an ABO_3 cubic perovskite. At around 550 °C, the orthorhombic structure transforms into a tetragonal structure with space group *I4/mcm*.[7] In the tetragonal unit cell RuO_6 octahedra are rotated only about the $[001]_{cubic}$ $SrRuO_3$ direction. At even higher temperatures of about 680 °C tetragonal $SrRuO_3$ transforms into a cubic structure with a standard perovskite space group *Pm*-3*m* where the RuO_6 octahedra are not rotated.[7]

Maria *et al.*[8] report thin $SrRuO_3$ films grown on $SrTiO_3$(001) substrates undergo an orthorhombic to tetragonal (O-T) structural phase transition at a somewhat lower temperature of ∼350 °C. They measured a tetragonal to cubic (T-C) phase transition temperature of ∼600 °C as well, but this was obtained from a bulk $SrRuO_3$ sample. The suggested transitions imply $SrRuO_3$ exhibits cubic symmetry during film synthesis, which is typically in the range of 600-700 °C.[8] Since the T-C transition was observed on a powder $SrRuO_3$ sample, which does not represent conditions of commensurate strained layer growth, it is still unclear what crystal symmetry strained epitaxial $SrRuO_3$ layer possesses during growth under constrained geometries (epitaxy) imposed by the substrate. A schematic representation of the unit cell as it grows on $SrTiO_3$ in its orthorhombic form can be found in figure 4.1 on the facing page.

The only experiment that can clarify the presence of one or the other symmetry is the measurement of the structure of a $SrRuO_3$ layer at high temperatures under the conditions at which it is normally deposited on any given single crystal substrate. To see the T-C transition in a thin oriented $SrRuO_3$ film is difficult because it involves just a slight rotation of the RuO_6 octahedra along the $[001]_{cubic}$ $SrRuO_3$ axis where only light oxygen atoms are involved. Using $SrRuO_3$ powder diffraction pattern simulations we established that the $SrRuO_3$(211) diffraction peak is very sensitive to oxygen rotation and is absent in the cubic symmetry. In this chapter, capitalizing on this insight, we report a study of the temperature-dependent structural transition of $SrRuO_3$ films

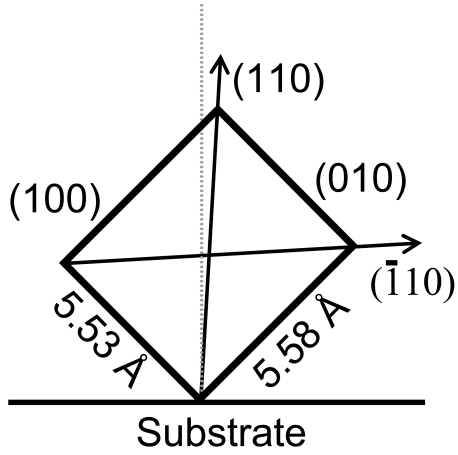

Figure 4.1: *An illustration of the $SrRuO_3$ orthorhombic unit cell as it grows on $SrTiO_3$ at room temperature, with its out-of-plane lattice parameters, the in-plane lattice parameter is strained to $SrTiO_3$ and is 7.81 Å in length. Note that the (110) axis is not perfectly parallel to the surface normal.*

coherently grown on $SrTiO_3(001)$ substrates by high-resolution x-ray diffraction using laboratory as well as synchrotron radiation sources.

4.1.2 Electronic structure and correlation

As noted above, besides its structural properties $SrRuO_3$ is a material of uncommon scientific interest. It is unusual among the correlated complex oxides in that it is a metallic itinerant ferromagnet. It exhibits so-called bad metal behavior at high temperatures, but it is clearly a Fermi liquid at low temperatures. It is also of great technical interest and is widely used as a conducting electrode in many devices utilizing complex oxides of various kinds. One of the important open questions in the physics of $SrRuO_3$ is its degree of electron correlation and how that correlation affects the physical properties of the material. A related question is what are the factors that control the degree of correlation. Recently Kim *et al.*[9] have shown, using photoemission data, how the degree of correlation varies systematically in the ruthenate family of complex oxides as a whole. Toyota *et al.*,[10,11] using transport and photoemission measurements, have studied the degree of correlation as a function of $SrRuO_3$ film thickness (at the few monolayer level) and shown that a correlation-driven insulator-to-metal transition occurs as film thickness increases. In this chapter we demonstrate that the degree of correlation depends on stoichiometry and how this dependence correlates with various physical properties of the material.

At the same time our results solve the heretofore mystery of why the transport properties of $SrRuO_3$ are so sensitive to how it is synthesized, particularly in thin film form.[12] More specifically, we show that this sensitivity is not a simple matter of defect

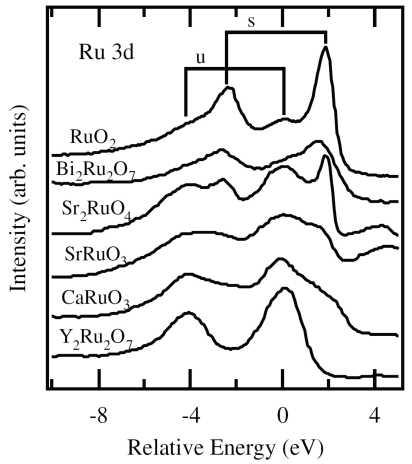

Figure 4.2: *Ru 3d XPS spectra of RuO_2, $Bi_2Ru_2O_7$, Sr_2RuO_4, $SrRuO_3$, $CaRuO_3$, $Y_2Ru_2O_7$. s and u denote screened and unscreened peaks, respectively. All the spectra are aligned by the unscreened-peak positions of Ru $3d_{\frac{5}{2}}$. This figure was taken from Kim et al.*[9]

scattering, but once again is related to stoichiometry and the degree of correlation.

The properties observed in the ruthenate family of complex oxides range from very good metals (RuO_2) to insulators ($Y_2Ru_2O_7$). Recently Kim *et al.*[9] suggested that this change in electronic behavior can be attributed to a change in electron-electron correlation. Those authors come to this conclusion based on fits of experimental core level photoemission spectra[13] using Dynamic Mean Field Theory.[14] Kim *et al.*[9] compared the $3d$ peaks of ruthenium for ruthenates that are put in order of metallicity and a systematic relative shift in spectral weight from the so called *screened* peak to the *unscreened* peak is observed, as is shown in figure 4.2, which was taken from the paper by Kim and coworkers.[9] To explain these shifts, these authors[9] use a model in which the fitting parameters are the Hubbard U and the bandwidth W of the ruthenium $4d$ band. The outcome of their analysis is that the ratio U/W correlates with the ratio of the *screened* and *unscreened* peaks, from which one can deduce that the stronger the *screened* peak the less correlation (i.e. the more metallic).

In UPS spectra, a similar shift in spectral weight is observed. In this case, the t_{2g} peak, which is very close to the Fermi level and referred to as the *coherent* peak (i.e. the quasiparticle band near E_F), is reduced as correlation increases, and a broad peak around 1.5 eV starts to rise. This latter peak is called the *incoherent* peak, which is the remnant of the Hubbard bands 1–2 eV above and below E_F. Both $SrRuO_3$ and $CaRuO_3$ can be classified by their XPS and UPS spectra in this way, despite, for example, similar transport properties at room temperature. Based on the classification by XPS spectra $CaRuO_3$ should be a more correlated system than $SrRuO_3$. However the samples studied by Kim *et al.*[9] could have suffered from the same off-stoichiometry, for example, due to the surface or sample preparation processes, as we will discuss later in this chapter.

Viewed from the perspective of the work by Kim *et al.*,[9] in this chapter we show that similar systematic variations in the degree of correlation can occur within a single ruthenate as a function of stoichiometry. In particular, it turns out that one source of disorder/off-stoichiometry can be varied in $SrRuO_3$ thin films by changing the deposition conditions or (what turns out to be more or less equivalent) the deposition technique. Specifically, we demonstrate that variation of vacancies on the ruthenium site gives rise to a systematic change in the degree of correlation. Moreover, the transport properties of our samples are clearly linked to their photoemission spectra (XPS and UPS) and to the crystal unit cell parameters. This correlation with the unit cell volume, V_c, permits us to use V_c as a surrogate variable for the ruthenium deficiency, a dependency which is well known from literature.[12] This change in volume also alters the average Ru-O-Ru bond angle which is known to be closely connected to the d-band width[15] and therefore electron correlation. $SrRuO_3$ appears to be a system where these effects of correlation can be studied in a systematic fashion, usually not easily accessible, but we suspect that the underlying physics is generic.

4.1.3 Magnetic properties

Besides the structural and electronic properties this chapter will also focus on the magnetic properties of very thin layers. Itinerant magnetism in strongly correlated electron systems has been a subject of intense study in recent years. While the transport and magnetic properties of good metallic ferromagnets, such as the $3d$ elemental ferromagnets, are by now fairly well understood, this is not the case for bad metallic itinerant ferromagnets. $SrRuO_3$ is an itinerant ferromagnet with an orthorhombically distorted cubic perovskite structure and exhibits a transition to a ferromagnetic state at $T_c \sim 150$ K (for strained thin films) that was shown to be dominated by transverse fluctuations of robust local moments of size $\sim 1.6\ \mu_B$,[16] the largest of any $4d$ ferromagnet. In the paramagnetic phase it was shown to exhibit a *bad metal* behavior in the limit of $k_F l \sim 1$,[17] suggesting that Fermi liquid theory may not be valid at high temperatures. However, the observation of quantum oscillations in the electrical resistivity of a high-quality thin films of $SrRuO_3$ demonstrated the existence of long-lived fermion quasiparticles at low temperatures, and strongly suggested that the ground state of this system is a Fermi liquid.[18] To understand the contrast in the behavior of $SrRuO_3$ between high and low temperatures, appropriate perturbations such as disorder and reduced dimensionality, are needed that directly disturb the magnetic and transport properties of the system.

Indeed, recent studies from several groups emphasized the interplay between itineracy and ferromagnetism in thin films of $SrRuO_3$.[10,19] In particular, Toyota *et al.*[10] presented new results on the thickness dependence of metallicity and ferromagnetism in this $SrRuO_3$ films concluding that a metal-insulator transition (MIT) accompanied by the disappearance of ferromagnetism occurs in these films at a critical film thickness of 4 to 5 monolayers (ML). The observation was supported by photoemission measurements showing that below that critical thickness no finite density of states is found at the Fermi level, and by resistivity measurements showing insulating behavior below that thickness. The ferromagnetic transition was determined from the anomaly in the

resistivity.[17]

While Toyota *et al.*[10] presented a complete set of measurements with a definite conclusion, the quality of the samples near the critical thickness suggests that much of the behavior observed is due to the island-like growth and coalescing of three-dimensional patches. Thus, a complementary study, in which the films grow layer-by-layer for at least the first ∼10 layers, is needed to establish the relation between ferromagnetism and itineracy in ultrathin films of $SrRuO_3$. In addition, a more direct probe of ferromagnetism is needed to establish the nature of the magnetic moment, its strength and anisotropy, as well as its strength below the critical thickness.

In this chapter we present new results on the MIT in ultrathin $SrRuO_3$ films and the magnetic properties of such films. We show that in homogeneous films of $SrRuO_3$ a MIT occurs at a critical thickness below 4 monolayers (ML), below which ferromagnetism is also undetectable. While T_c drops rapidly below ∼10 ML, the size of the moment remains unchanged from its 1.6 μ_B in thick films.[16] Examination of the transport properties of the measured films shows an increase in the sheet resistance with decreasing thickness. At 4 ML the extrapolated low-temperature sheet resistance is ∼7 kΩ (about a quarter of the two-dimensional quantum of resistance), jumping to several megaohm just below the transition.

4.1.4 Summary

To summarize the questions that will be answered in this chapter:

1. What crystal symmetry does the strained $SrRuO_3$ unit cell on $SrTiO_3$ possess at deposition temperatures (700 °C)?;
2. How can we explain the untwinned growth of $SrRuO_3$ on $SrTiO_3$?;
3. Why are the transport properties of $SrRuO_3$ so sensitive to the deposition conditions and to the deposition technique?;
4. How does the degree of correlation vary with other properties of $SrRuO_3$?;
5. How does the magnetism in the material behave when films are made thinner than 10 ML?;
6. How can we explain the MIT that occurs as a function of thickness between 3 and 4 ML?

As a first step to answering these questions, the growth of the thin films will be briefly discussed.

4.2 Thin film growth

The thin film samples reported in this chapter are grown by two different methods: Molecular Beam Epitaxy (MBE) and Pulsed Laser Deposition (PLD). The samples are grown in the same vacuum chamber with a background pressure of 10^{-9} Torr. All films are grown on TiO_2 terminated $SrTiO_3$ substrates, prepared according to Koster *et al.*[20] The MBE samples are deposited in an oxygen pressure of 10^{-5} Torr and at

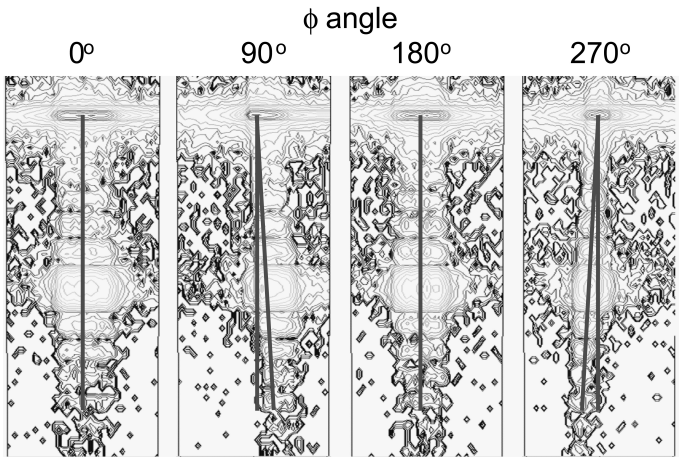

Figure 4.3: *Reciprocal lattice map of $SrRuO_3$ (220) and $SrTiO_3$ (002), which shows that the films are strained and slightly distorted from the orthorombic structure (γ=89.1–89.4°).*

a substrate temperature of 700 °C at a rate of about 1 Å/s from separate ruthenium and strontium sources, which enables us to vary the ratio of ruthenium to strontium. Typical thickness of the films grown ranges from 200 to 300 Å.

For PLD, the energy density on the target is kept at approximately 2.1 J/cm^2. Films are deposited with a laser repetition rate of 4 Hertz, with the substrate temperature at 700 °C. The oxygen background pressure is 10^{-5} Torr as in the MBE case for samples grown in the MBS vacuum chamber or 320 mTorr (50 % Ar, 50 % O_2) when grown in an alternative (simpler) vacuum system, however no atomic oxygen was provided for the PLD films in either system. The thickness of the films is in the same range as for the MBE samples.

4.3 Temperature dependent XRD

The XRD results demonstrate that our $SrRuO_3$ films exhibit (110) out-of-plane orientation with their (100) and (-110) in-plane orientations along the [100] and [010] directions of the $SrTiO_3$ substrate. Reciprocal lattice maps (RLM) taken at room temperature using symmetrical and asymmetrical reflections confirm that the $SrRuO_3$ layers are grown in a fully coherent fashion to the underlying $SrTiO_3$(001) substrate and exhibit a slightly distorted orthorhombic unit cell with the angle γ between the [100] and [010] directions being less than 90°. Such a distortion was reported earlier by Gan *et al.*[21] Coherently grown $SrRuO_3$ is compressively strained along the [-110] and [001] directions. The in-plane compressive stress introduces out-of-plane strain that elongates the $SrRuO_3$ unit cell along the [110] direction. Such constrained in-plane geometry distorts the $SrRuO_3$ lattice from the ideal orthorhombic structure, which is made visible in the reciprocal space map in figure 4.3.

Figure 4.4 on the next page contains the reciprocal space map for a twinned film,

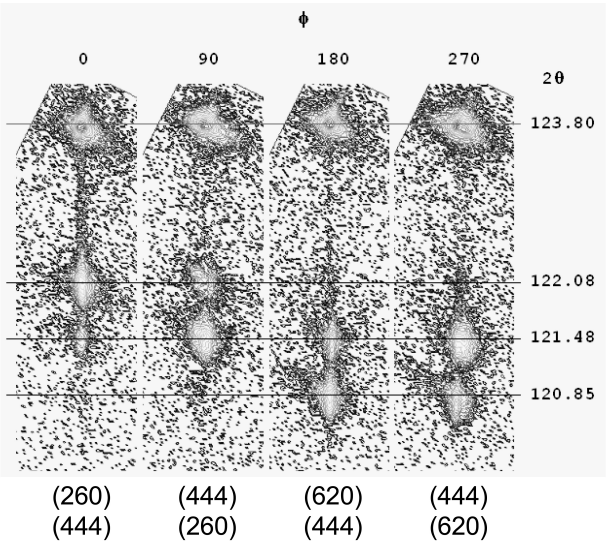

Figure 4.4: *Room temperature reciprocal space maps of $SrTiO_3$(204) and $SrRuO_3$(260), (444), (620), and (44$\overline{4}$) Bragg reflections for a twinned PLD grown film. The twinning manifests itself in the double peak structure of the film peaks. The maps for the untwinned case are shown in figure 4.5.*

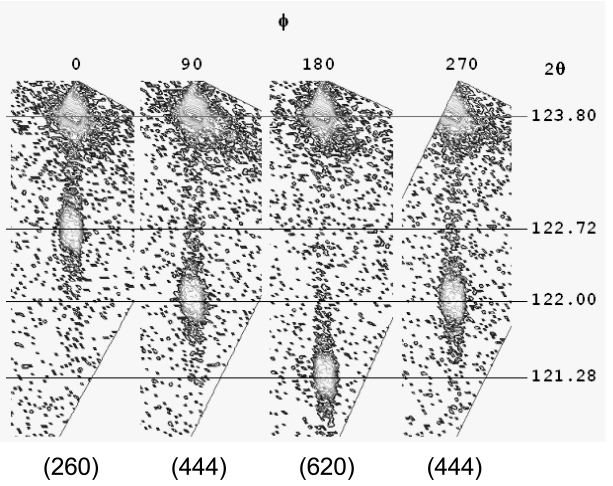

Figure 4.5: *Room temperature reciprocal space maps of $SrTiO_3$(204) and $SrRuO_3$(260), (444), (620), and (44$\overline{4}$) Bragg reflections for an untwinned MBE grown film. The fact that (260) and (620) peak positions are different from (444) and (44$\overline{4}$) positions indicates that the unit cell is orthorhombic. Compare these maps to the ones in figure 4.4, which are for a twinned film.*

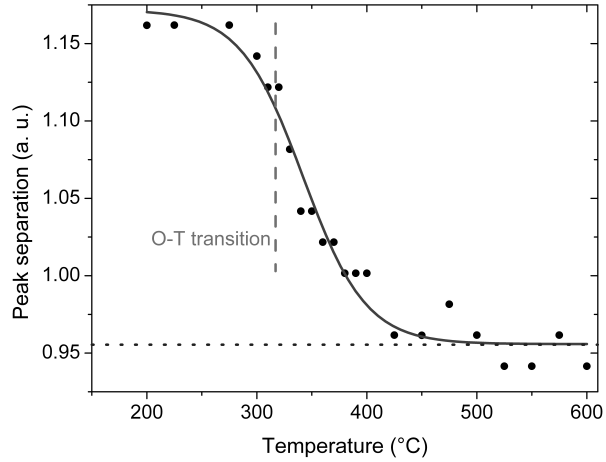

Figure 4.6: *The distance between the $SrTiO_3(204)$ and $SrRuO_3(620)$ peaks in reciprocal space as a function of temperature indicating an orthorhombic to tetragonal transition. The black horizontal dotted line indicates the separation between the $SrTiO_3(204)$ and $SrRuO_3(444)/(44\overline{4})$ peak positions (see figure 4.5 on the facing page)*

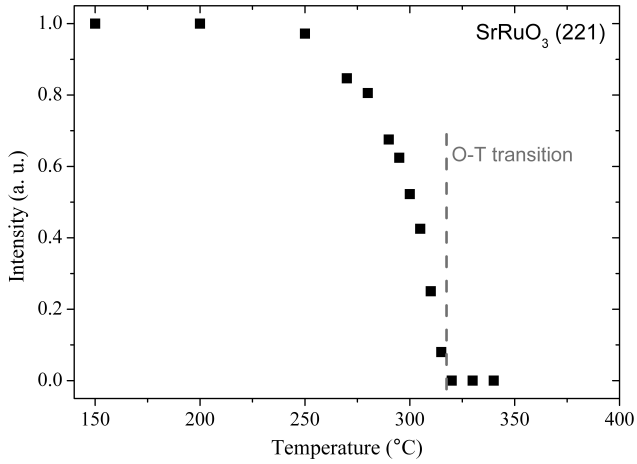

Figure 4.7: *The intensity of the $SrRuO_3(221)$ peak as a function of temperature, the disappearance of the peak indicates the symmetry of the film changes to tetragonal.*

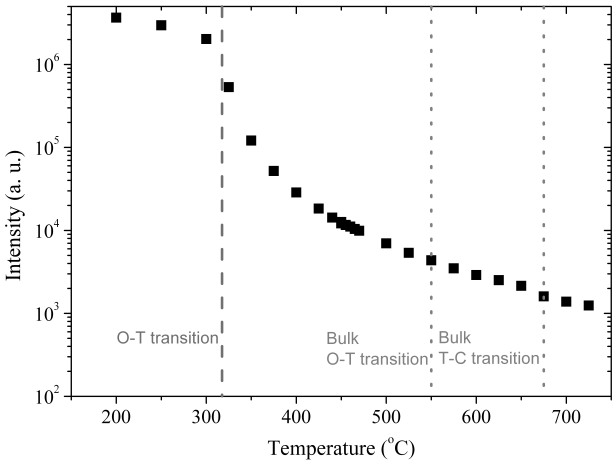

Figure 4.8: *Intensity of the $SrRuO_3$ (211) peak as a function of temperature. The nonzero intensity indicates that $SrRuO_3$ possesses a tetragonal symmetry up to 730 °C.*

grown by PLD in this case. The $SrTiO_3$ (204) peaks show only one domain, whereas the film peaks show a double peak for each 90° phi rotation. Figure 4.5 on page 56 shows reciprocal lattice maps from the (260), (444), (620) and $(44\bar{4})$ reflections for an MBE grown film together with the $SrTiO_3$(204) reflections of a single domain $SrRuO_3$ layer. The difference in $SrRuO_3$ (260) and (620) atomic plane spacings represents dissimilarity in the a and b lattice parameters that is typical for the orthorhombic structure. In contrast, the tetragonal structure with $a = b$ would show identical positions for the (260) and (620) Bragg reflections. In reciprocal space the transition from the orthorhombic to the tetragonal structure leads to an increase of the distance between $SrRuO_3$(260) and $SrTiO_3$(204) peaks while the distance between the $SrRuO_3$(620) and $SrTiO_3$(204) peaks will decrease.

In order to examine the O-T transition, temperature-dependent XRD scans were performed along l-direction. As can be seen from figure 4.6 on the previous page, the distance between $SrTiO_3$(204) and $SrRuO_3$(620) peaks decreases as the temperature increases. Above ∼450 °C the $SrRuO_3$(620) peak position reaches the same value as $SrRuO_3$(260) completing the transition to the tetragonal structure. Figure 4.7 on the preceding page shows the $SrRuO_3$(221) peak intensity as a function of temperature. The disappearance of this peak at higher temperatures further proves the presence of a tetragonal phase with an O-T transition temperature of ∼310 °C.

Finally, temperature dependent x-ray diffraction measurements of the $SrRuO_3$(211) diffraction peak were performed using synchrotron radiation. The $SrRuO_3$(211) peak intensity as a function of temperature is shown in figure 4.8. The peak intensity gradually decreases indicating the rotation of the oxygen atoms, but it does not vanish up to temperatures of ∼730 °C.

4.4 Electron correlation

4.4.1 Stoichiometry manipulation

By varying the deposition conditions, we found that the properties of the films changed. The films so obtained were divided into three groups: ruthenium rich, nearly stoichiometric and ruthenium poor. The ruthenium rich samples are typically made by using a relatively low oxygen partial pressure and/or low atomic oxygen flux and depositing a little excess ruthenium. The nearly stoichiometric samples are single phase and are obtained by tuning the oxygen activity together with the use of a Ru/Sr ratio close to one. The ruthenium poor samples are created by using relatively high partial oxygen pressures and a Ru/Sr ratio greater than or equal to one (the ruthenium flux does not seem to be the determining factor here).

Results show it is impossible to grow $SrRuO_3$ with strontium vacancies. It is possible though to grow samples that are stoichiometric or with ruthenium vacancies (for reasons discussed later). These samples are single phase and have the $SrRuO_3$ crystal structure with no precipitations. The precise stoichiometry is difficult to determine, but, based on the combined analysis (XRD and XPS), we can make the above distinction without further specifying the exact composition of individual samples in each group. All three sample types can be obtained by MBE, but samples made by PLD using a stoichiometric target typically are ruthenium poor. In the remainder of this section, we will focus on samples that are either nearly stoichiometric or ruthenium poor.

4.4.2 Results

We first present our resistivity measurements. In figure 4.9 on the following page, the normalized resistance is plotted as a function of temperature for three samples: a stoichiometric MBE, a ruthenium poor MBE, and a ruthenium poor PLD film. The normalization factor is the room temperature resistivity. For the stoichiometric samples the room temperature resistivity (in the bad metal regime) is around 190 $\mu\Omega$ cm, which compares well to values found in literature for polycrystalline and single crystal samples (150 to 200 $\mu\Omega$ cm). When ruthenium vacancies are introduced the value increases markedly to roughly 300 $\mu\Omega$ cm. The room temperature resistivity varies systematically with the amount of ruthenium vacancies, as will be shown in figure 4.11 on page 62 (discussed below). Also of interest is the Residual Resistivity Ratio (RRR), which is defined as the resistivity at 300 K divided by the value at 4 K. For the best single crystals, values between 50 and 100 are reported,[22] and similar results can be obtained for optimized thin films.[17] Like the room temperature resistivity, the RRR is very sensitive to changes in stoichiometry. For the stoichiometric sample in figure 4.9 on the following page (black line), the RRR is 26, which is excellent for the thickness of these samples,[23] whereas for both ruthenium poor films (light gray and dark gray lines) the RRR drops to around 7. Note that for the majority of PLD films in the literature, which fall in the ruthenium poor class (see below), values of 5 or less are reported.[24,25]

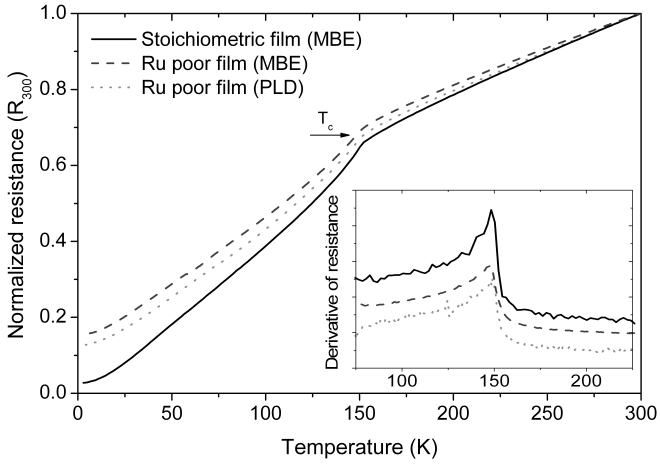

Figure 4.9: *Resistance behavior as a function of temperature for a nearly stoichiometric MBE grown (black solid), a ruthenium poor MBE grown (dark gray dashed), and a PLD grown (light gray dotted) $SrRuO_3$ film. The resistance has been normalized with respect to the values at 300 K. The inset shows the derivative of each line, T_C has been set as the point where the derivative is maximal. The resistivity (ρ) of the stoichiometric MBE grown $SrRuO_3$ at room temperature is about 190 $\mu\Omega$ cm and its carrier density at 4 K is 2 $\times$ 10^{22} cm^{-3}.*

Next we turn to the Curie temperature of our films, which are shown in the inset of figure 4.9, where the temperature derivatives of the resistance near the transition temperature are compared. The transition temperature, T_C, in bulk samples is 160 K, whereas in all of our thin film samples T_C is reduced by about 10 K due to strain.[26] According to literature, we know that when a sufficient amount of ruthenium vacancies are introduced, T_C is lowered further.[12] This gives us some indication of the order of magnitude of the vacancy density. On this basis we estimate that for the range of samples studied in this section the vacancy concentration is much smaller than a few percent.

In order to get a quantitative indicator of the ruthenium deficiency, we examined the change in lattice parameters on going from the stoichiometric to ruthenium poor samples. In figure 4.10 on page 62 we show $\theta/2\theta$ scans for two thick films (330 nm), one grown with MBE in low oxygen pressure and one with PLD in high oxygen pressure, to illustrate the difference in the d-spacing for the out-of-plane (110) direction of $SrRuO_3$ when different deposition techniques are used. These films are much thicker than the samples compared in other parts of the section to show that the films remain perfectly crystalline and strained up to very large thicknesses. In addition these scans reveal the very high degree of crystallinity of the samples by the existence of finite size fringes in the scans for both samples. As can be seen, the out-of-plane lattice constant is larger for the film grown in high oxygen pressures, which is explained by a lower ruthenium content.[12] Since the c-axis (in-plane) of the $SrRuO_3$ is fixed by epitaxy (the films are fully strained for all sample thicknesses in this chapter) the increase in the

(110) direction (linear combination of the a- and b-axis) is directly proportional to an increase in unit cell volume, which we take as our measure of the ruthenium deficiency in figure 4.11 on the next page.

We obtained the lattice parameters by refining on six reflections. For samples which were classified as having low ruthenium content, we find a unit cell with larger volume. This increase in the case of ruthenium vacancies is consistent with earlier measurements done on ruthenium deficient single crystal samples.[12] The bulk values taken from literature are a=5.572 Å, b=5.533 Å, c=7.849 Å and V_{bulk}=242.0 Å^3 for single crystals and correspond to an unstrained lattice, unlike the films grown here on $SrTiO_3$.[12]

In figure 4.11 on the following page we show how changes in the transport data correlate with the volumes of the orthorhombic unit cell for various films studied. The room temperature and low temperature resistivities as well as the RRRs show a clear trend with smaller volumes showing the lowest resistivities and highest RRRs. These films are typically found in our second group made by MBE (oxygen activity tuned to optimize oxidation and ruthenium sticking). On the other end, PLD films appear to have larger volumes and poorer transport properties. Note that the Curie temperature should also show a similar trend, although the change in T_C is small as shown in figure 4.9 on the preceding page.

To get a clearer understanding of how or whether the electronic properties of $SrRuO_3$ vary as a function of stoichiometry, we measured the UPS and XPS spectra of some of our samples. XPS and UPS measurements were performed *in situ*, which is crucial for obtaining reliable data in this case since the surface of $SrRuO_3$ is known to change when exposed to air[27] in a way that gives rise to surface states in the spectra. In figure 4.12 on page 63, the UPS spectra are plotted for the same samples that were used for the transport data in figure 4.9 on the preceding page. Note that these spectra are normalized on the t_{2g} peak to make comparing them easier. For the stoichiometric $SrRuO_3$ sample grown by MBE, the spectrum shows a peak at the Fermi energy, corresponding to the ruthenium t_{2g} band and a valley at binding energy ∼1.5 eV. This peak has been observed before by Kim and coworkers[28] and also is expected based on models.[29] In ruthenium poor samples, as can be seen in figure 4.12, for both the PLD film as well as the ruthenium poor MBE film, a second, broad peak appears at ∼1.5 eV, the so-called *incoherent* peak.

Examples of XPS core level spectra for one stoichiometric and one ruthenium poor sample are plotted in figure 4.13 on page 63. For clarity we reduced these spectra of the ruthenium 3d doublet by subtracting the strontium $3p_{\frac{1}{2}}$ peak fitted with a Gaussian, which overlaps at lower binding energy. Note that our *in situ* measurements are free of carbon contamination and its complications near the surface region[27] and of the C 1s peak, which normally also overlaps with Ru 3d. The stoichiometric sample shows more spectral weight for the Ru $3d_{\frac{3}{2}}$ peak at lower binding energy compared to the ruthenium poor sample. Peak fitting using 3 sets of Gaussians (the area of the peaks in each spin orbit doublet pair have a 2:3 ratio) shows that at a binding energy of ∼278 eV an extra curve (gray filled) is necessary to fit the data for stoichiometric $SrRuO_3$, which is arguably the so-called *screened* peak typical for $SrRuO_3$. On the other hand, the data for the ruthenium poor sample is dominated by the *unscreened* peaks.

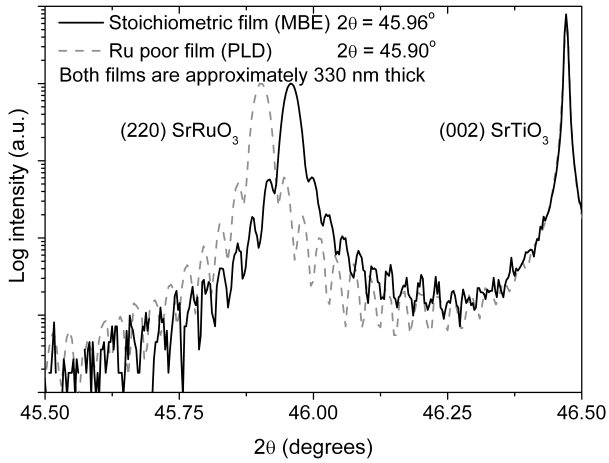

Figure 4.10: *Comparison of $\theta/2\theta$ XRD scans of two thick (330 nm) films grown by PLD and MBE. The fringes indicate good crystalline quality of the films, the shift in peak position shows the PLD film has a larger out of plane lattice parameter (110 direction).*

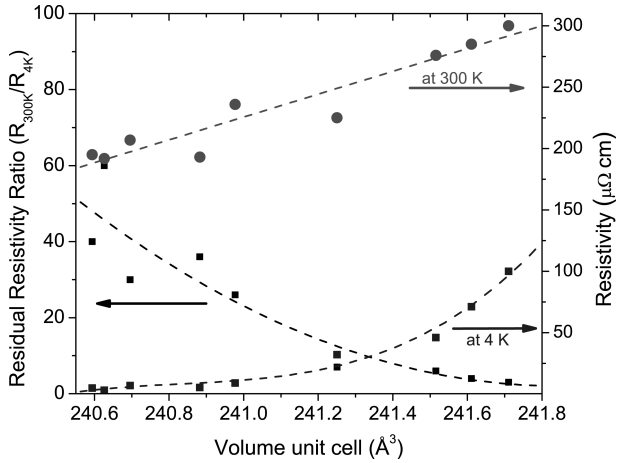

Figure 4.11: *A comparison between the volume of the $SrRuO_3$ unit cell in thin films on $SrTiO_3$ substrates grown by either MBE or PLD and their transport properties: room temperature and low temperature resistivity on the right y-axis and Residual Resistance Ratio on the left y-axis. The dashed lines are guides to the eye.*

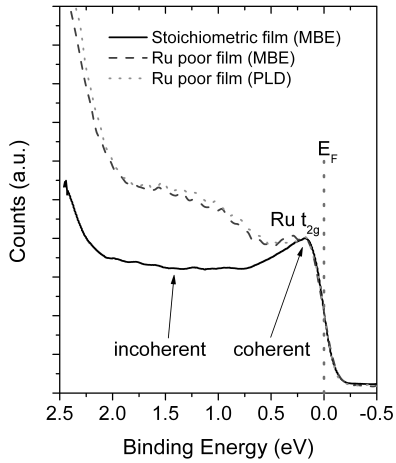

Figure 4.12: *UPS spectra at room temperature of three $SrRuO_3$ films: an MBE film, a ruthenium poor MBE film and a PLD grown film (same samples as in figure 4.9 on page 60). All samples show states at the Fermi edge and a Ru t_{2g} peak close to the Fermi level. The spectra have been normalized on the t_{2g} peak.*

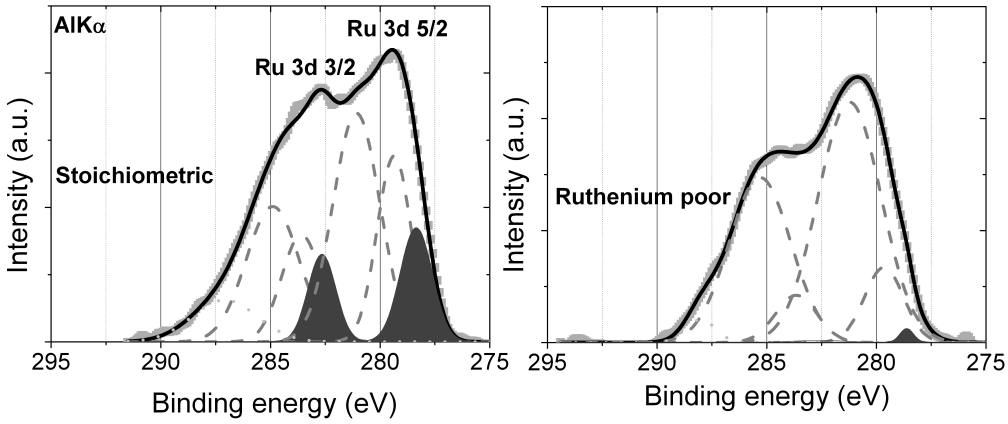

Figure 4.13: *XPS detail spectra at room temperature of the Ru 3d doublet of a stoichiometric film (left) and a ruthenium poor film (right), including fitting of the spectra using 3 spin orbit coupled doublets represented by Gaussians; the overlapping Sr $2p_{\frac{1}{2}}$ peak (Gaussian) was subtracted for both spectra. In the spectrum of stoichiometric film more pronounced screened peaks (dark gray filled) are needed to give a good fit, indicative of less correlated behavior. For the ruthenium poor spectrum the screened peaks are almost non-existent.*

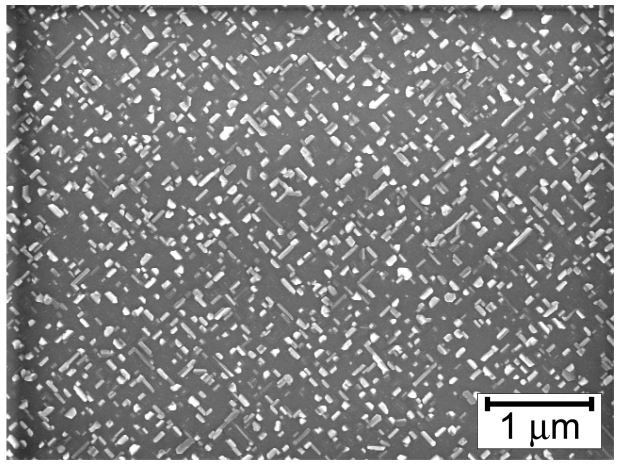

Figure 4.14: *A SEM image of a ruthenium rich sample. Precipitations on the surface that show up in a lighter color than the $SrRuO_3$ background. The islands are elongated in one direction which lies parallel to the (110) of $SrTiO_3$ (the (100) and (010) of $SrTiO_3$ run parallel to the sides of the image), which indicates that the unit cell is 45 degrees rotated with respect to the substrate, as expected for RuO_2.*

4.4.3 Discussion

Before discussing the data explicitly, we would first like to point out that the stoichiometry of the samples is extremely dependent on the oxygen activity during deposition. For MBE this can be independently varied by controlling the flux of molecular or atomic oxygen. Apparently the sticking of ruthenium (possibly through the formation of RuO_4, which is very volatile)[30,31] is a function of oxygen activity: at relatively low oxygen activity the stoichiometry is mostly determined by the supplied Sr/Ru ratio. When excess ruthenium is supplied, RHEED, SEM, Auger spectroscopy and TEM reveal precipitation of RuO_2, and the Ru 3*d* core-level spectra show very strong *screened* peaks typical for RuO_2. An SEM image for a ruthenium rich film is given in figure 4.14 and the AES images for the same sample are shown in figure 4.15 on the facing page. From the AES images the precipitations appear to be ruthenium rich, strontium poor and slightly oxygen poor when compared to the $SrRuO_3$ film. The precipitations, which are most likely RuO_2, might show up as oxygen poor due to a different sensitivity factor for oxygen between $SrRuO_3$ and RuO_2. At intermediate oxygen activity, it is most favorable to achieve perfect stoichiometry: RHEED shows two dimensional growth and XPS/UPS show almost perfect spectra typical for $SrRuO_3$. The *best* values for resistivity and RRR are obtained here. Finally, at high oxygen activity, ruthenium vacancies are unavoidable and independent of the ratio Sr/Ru in the supplied vapor: RHEED shows two dimensional growth, layer-by-layer or even step flow[2] and XRD clearly shows a modification in the unit cell indicative of ruthenium vacancies.[12]

We believe the last scenario also to be the case for PLD films where a high (atomic) oxygen pressure exists within the plume (additional to the background activity); very

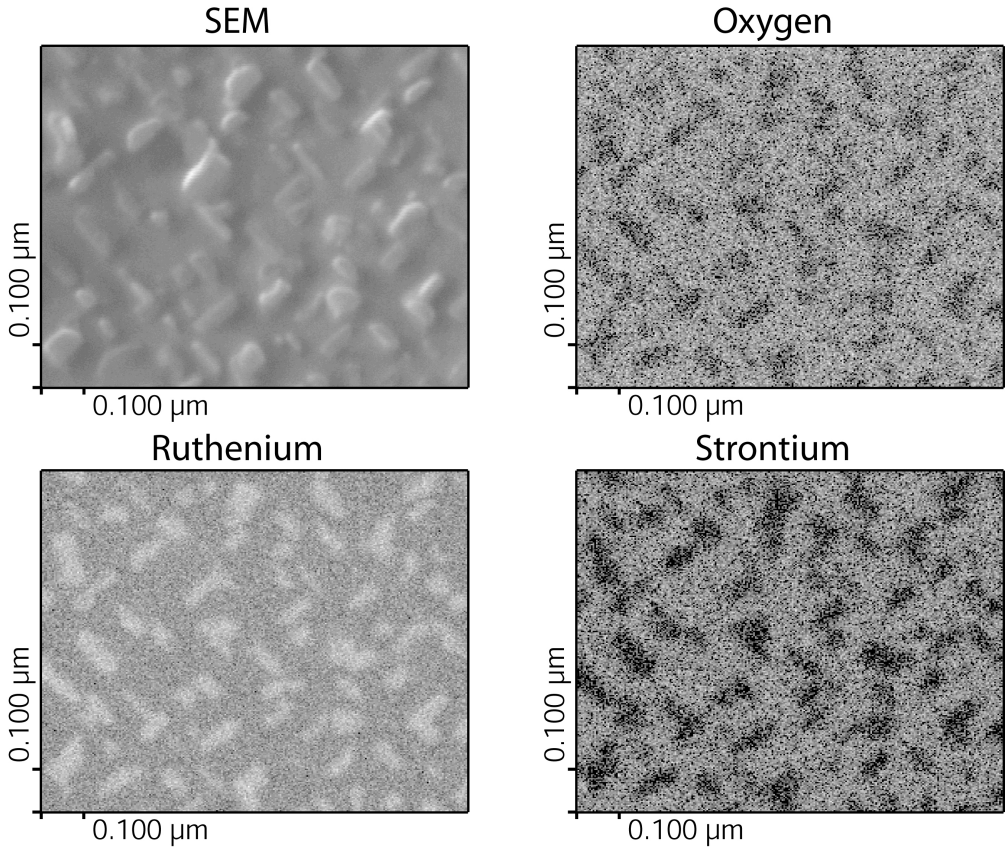

Figure 4.15: *A SEM picture of a ruthenium rich $SrRuO_3$ thin film with the associated elemental maps as obtained with AES. The precipitations show up clearly in all the scans and contain no strontium, but seem ruthenium rich and oxygen poor. The precipitations are almost certainly RuO_2 and might show up oxygen poor due to a change in the sensitivity factor between $SrRuO_3$ and RuO_2.*

little can be done to avoid this. PLD offers the advantage of making the same quality film every time, albeit ruthenium poor. On the other hand, we have shown that even when ruthenium vacancies are present the crystallinity of the material remains the same compared to the stoichiometric films and therefore, cannot be used to explain any of the observed variations in transport and PES. There seems to be no indication that oxygen vacancies play a significant role, but we cannot distinguish this from the formation of ruthenium vacancies by looking the response of lattice constants only. In a study of similar ruthenium deficient samples, oxygen vacancies were not observed.[12]

Resistivity is both affected at low temperatures with lower RRR values and at higher temperatures with a variation in lower room temperature resistivity for stoichiometric samples. At low temperatures defect scattering dominates transport properties resulting in the systematic behavior of the resistivity at low temperatures. The RRR values increase and decrease, respectively, almost exponentially with unit cell volume (more defects). On the other hand, at room temperature in the bad metal regime, the resistivity increases more linearly with the unit cell volume. This indicates that more than just scattering is contributing at room temperature. It would be interesting to study the high temperature behavior (beyond the Ioffe-Regel limit[32]) as a function of stoichiometry, which is part of a planned future endeavor.

Now we turn to the observed differences in PES and their correlation with transport properties as a function of ruthenium stoichiometry. First, it is logical to exclude the ruthenium rich samples from this comparison because both transport and PES would be a mixture of $SrRuO_3$ and precipitated RuO_2. Both UPS and XPS spectra of films with ruthenium vacancies are distinctly different from their stoichiometric counterparts. Our data of the Ru $3d$ peaks in $SrRuO_3$ with vacancies suggest that these ruthenium poor samples show almost no *screened* peaks, whereas the stoichiometric samples show pronounced *screened* peaks. This effect is most often associated with the material becoming more correlated, which has been quantified by Kim and coworkers;[9] see also our earlier discussion. In the same spirit, ruthenium poor samples show spectral weight at ∼1.5 eV in HeI UPS, which has previously been attributed to an *incoherent* peak in a picture of a strongly-correlated system. When the ∼1.5 eV peak is absent, the t_{2g} peak at the Fermi level becomes more pronounced. It is worth noting here that the t_{2g} peak at the Fermi level has not yet been observed with scraped bulk samples, indicating that thin film specimens may provide a better opportunity in investigating an intrinsic electronic structure of $SrRuO_3$ with photoemission spectroscopy as has been pointed out by Kim *et al.*[28] This shift in spectral weight is to be expected when the spectra are compared with DOS calculations.[29,33,34] The calculations show a t_{2g} peak with almost the same height as the O $2p$ peak. We can consider this discrepancy in terms of a self-energy correction to the one-electron band structure.[15,28,29,34,35] Due to the k dependence of the self-energy the spectral weight at the Fermi level is reduced by a factor m_k/m_b, where m_k is called the k *mass* and m_b is the bare band mass. By comparing to band calculations we estimate m_k/m_b to be 0.3 for the sample with ruthenium vacancies and 0.6 for the stoichiometric sample. Combining these values with the mass enhancement factor m^*/m_b as derived from the electronic specific heat γ, one obtains the quasiparticle weight $Z = (m_k/m_b)/(m^*/m_b)$. For m^*/m_b we have used the average value of 4.1 as determined by two different measurements.[29,33] This

leads to values of Z^{-1} of 13 and 7 for the ruthenium poor and stoichiometric samples respectively. The value of 13 for the ruthenium poor samples is in line with what has been reported by most authors.[28,29,34] The value of 7 for the stoichiometric samples is slightly lower than what was reported by Kim *et al.*[28] on their samples. The high values for Z^{-1} have been used by others[29,34] to explain the reduction of the t_{2g} peak at the Fermi level due to electron correlation. Our work shows that the intensity of the t_{2g} peak is very sensitive to the ruthenium stoichiometry and that UPS spectra of stoichiometric films look much more like the calculated DOS than ruthenium poor films. We conclude that the ruthenium stoichiometry (and possibly surface states contribute as well) has a much larger impact on PES spectra than previously assumed and could function for a large part as an explanation for the observed photoemission results in this section, but also by others. Of course the change in the PES spectra could be caused by a change in correlation due to the change in unit cell and the Ru-O-Ru bond angle, but it is also possible that the vacancies themselves cause it. Therefore we propose that besides a change in correlation, the transfer of spectral weight could also be caused by inelastic processes at the ruthenium vacancies. The t_{2g} orbitals that form the conduction band form states spreading in two dimensions. To define the energy of a state to within the observed 0.5 eV peak, it would be necessary to construct a packet of band states, for a band of width 4 eV, which extended $4/0.5 = 8$ cube edges. The corresponding $\pi 4^2 \approx 50$ ruthenium sites would generally contain at least one vacancy, even at only 2% vacancies. It would be reasonable to expect that the removal of a band electron might cause shake-off excitations, vibrational or electronic, of the vacancy. This would increase the energy needed to eject the electron, as can be seen in both the UPS and XPS spectra.

4.5 Magnetism in ultra-thin films

The films for the following experiments were grown in the PLD system as described earlier in this chapter and in chapter 2. The thickness of the films ranges from 2 to 25 monolayers (ML), as determined by calibrating on thicker samples with x-ray reflectivity. The reproducibility of the thickness was found to be very high.

4.5.1 Results

The morphology of the films was characterized using atomic force microscopy (AFM). Figure 4.16 on the next page shows AFM images of $SrTiO_3$ substrate and $SrRuO_3$ films of various thickness immediately after film growth. $SrRuO_3$ films with thicknesses between 2 and 9 ML showed homogeneous coverage of the substrate, with two-dimensional stripe shaped steps following the $\sim 0.2^\circ$ miscut of the substrate. These two-dimensional steps are 1 ML in height and are typically 100 nm in width. Moreover, unlike previous reports,[10,19] no three-dimensional island growth was observed, indicating an atomically smooth surface and single domain structure in these films. The observed step-like growth seems to fade at thicknesses above 9 ML as the steps mostly coalesce, suggesting a transition from two-dimensional layer-by-layer growth to a step flow growth mode,

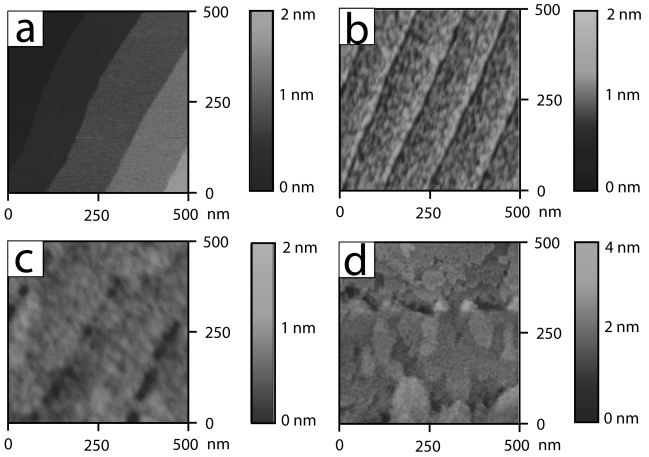

Figure 4.16: *AFM images of: (a) a $SrTiO_3$ substrate before deposition, (b) a 2 ML, (c) a 5 ML and (d) a thick $SrRuO_3$ film, all taken immediately following film deposition.*

in agreement with earlier reports.[3]

Resistance of samples was measured from room temperature down to 4.2 K. The ferromagnetic transition was noticeable in all films of 4 ML and above, however the transition becomes wide and difficult to determine for the very thin films. Figure 4.17 on the facing page shows the resistivity for the thin films through the transition. We note that while 4 ML exhibits a sheet resistance of ∼7 kΩ just below the transition, the resistance of the 3 ML is many orders of magnitudes higher than the quantum of resistance for two-dimensions of h/e^2 ∼26 kΩ. Thus, it is clear that a metal-insulator transition has occurred in between these two thicknesses.

The Kerr signal is measured with the loop-less Sagnac interferometer described in section 2.4.2 on page 23. In such a configuration, the polar Kerr signal is only sensitive to the out-of-plane component of the magnetization. Since the optical penetration depth at the used frequency is of the order of 200 nm and the thickest sample used was only 8.8 nm, the signal measured, to a very good approximation, was proportional to the area density of the magnetic moment.[36]

Figure 4.18 on the facing page shows the evolution of the polar Kerr effect (PKE) measured on the samples from 2 ML to the thickest samples measured 22 ML. Hysteresis loops were obtained by recording the Kerr signal at the lowest temperature while ramping an out-of-plane magnetic field, and then subtracting the linear paramagnetic response from the $SrTiO_3$ sample and diamagnetic response from the optical components in the fringing magnetic field. After the magnetic field was turned off, the films were then warmed in zero magnetic field to measure the remanent PKE signal ($\theta_K^R(T)$) as a function of temperature in order to determine the Curie temperature T_c of each film.

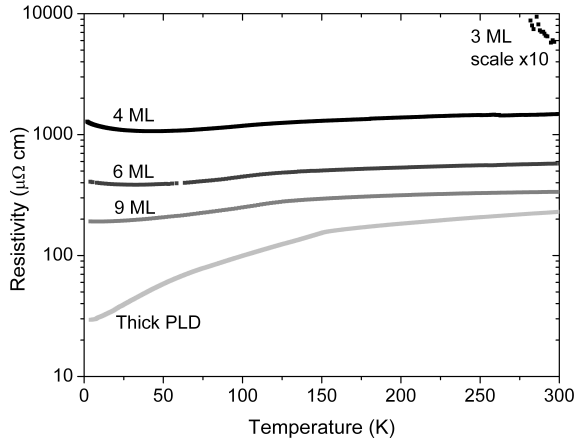

Figure 4.17: *The resistivity of the films as a function of temperature showing a MIT between 3 and 4 ML and weak localization behavior for the 4, 6, and 9 ML films at low temperature.*

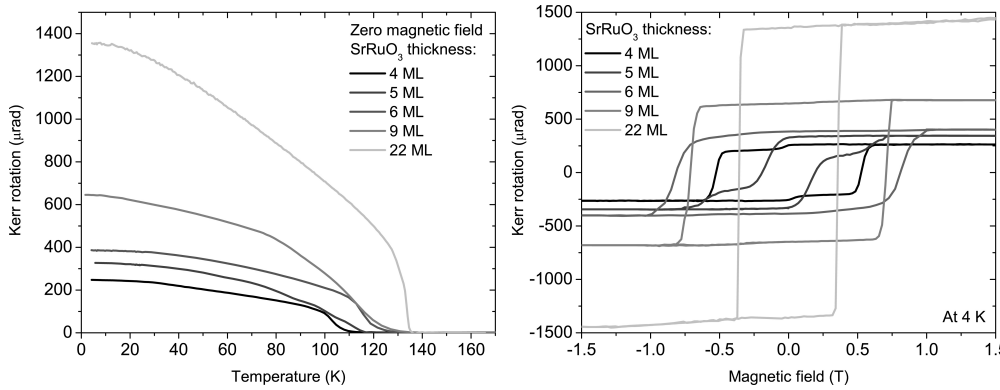

Figure 4.18: *(left) The temperature dependencies for various layer thicknesses of the remanent PKE signal measured in zero magnetic field during warmup, after a positive saturation magnetic field was turned off at the lowest temperature. (right) PKE hysteresis loops for $SrRuO_3$ films of different thickness taken at 4 K.*

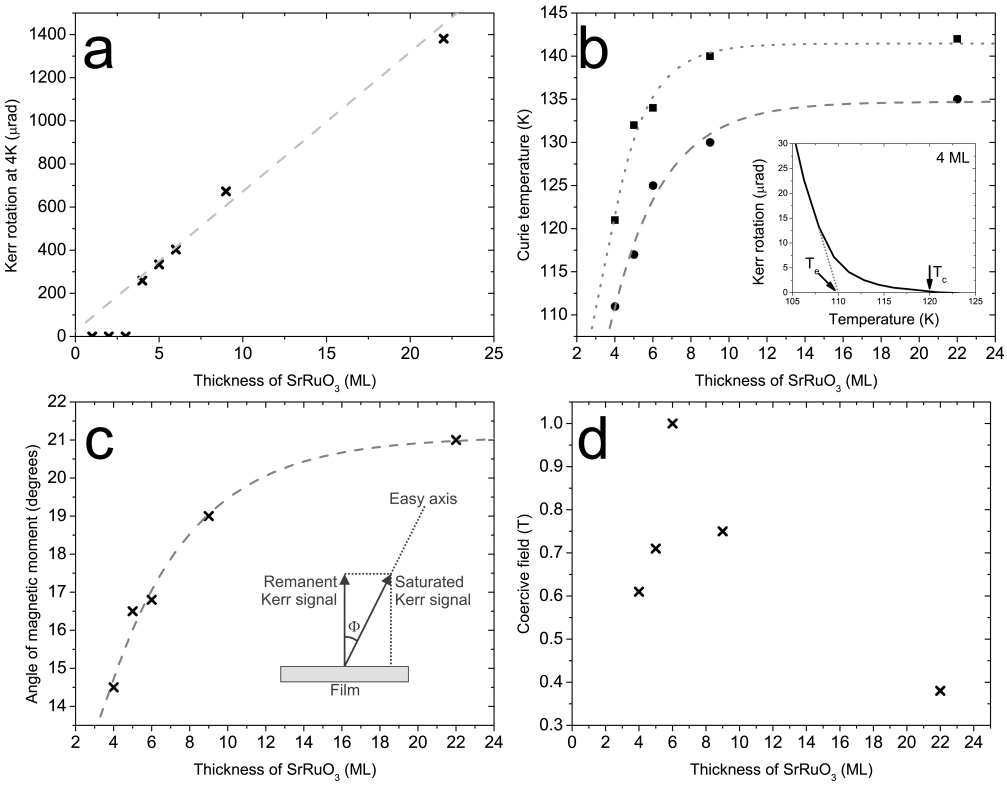

Figure 4.19: *Thickness dependence of: (a) the saturated Kerr signal at the lowest temperature, the dashed line is a linear fit of the points; (b) the Curie temperature with decreasing thickness, which shows the magnetic properties are suppressed in thinner layers; (c) the angle Φ between the film normal and magnetic easy axis at the lowest temperature; (d) the magnitude of the coercive field.*

In the magnetization curves of 2 and 3 ML films at 0.5 K no hysteresis or *S-shaped* curves are observed, suggesting the absence of either ferromagnetic or superparamagnetic ordering down to 0.5 K. This observation supports our assertion that the films used, even the thinnest ones, were homogeneous with no three-dimensional island growth. The magnetization measurements show a very small remanent Kerr signal of 0.8 μrad for the 3 ML film, which is more than 300 times smaller than the 4 ML film. This can be explained if 0.3% of the film within the 3 μm optical spot was covered by 4 ML patches, which is consistent with the 2 μrad error bar in the hysteresis loop. The first clear hysteresis loop is obtained for the 4 ML sample, indicating the onset of ferromagnetism. This is also accompanied by a remanent signal and a finite T_c.

The summary of all samples is given in figure 4.19. Here we first show the saturation Kerr signal ($\theta_K^S(T)$), which is determined as the highest point of the hysteresis loop in figure 4.18 as a function of thickness, the T_c of the layers, the variation of the easy axis,

and the magnitude of the coercive field for all ferromagnetic films. The first clear result is that below 4 ML there is neither a saturated signal, nor a finite Curie temperature indicating that these films are not ferromagnetic. Together with our observation on the disappearance of itineracy we conclude that both ferromagnetism and the MIT occur at the same critical thickness between 3 and 4 ML. We next note that the saturated Kerr signal is proportional to the film thickness from the thick 22 ML down to the thinnest samples, extrapolating to zero thickness. Since we argued that all these films are in the very thin limit compared to the optical penetration depth of the light, this result clearly shows that ferromagnetism is lost due to the film reaching a critical thickness below which ferromagnetism is not supported.

Figure 4.19b shows the thickness dependence of T_c. To determine the temperature above which no ferromagnetism is observed we magnified the region near the transition as shown in the inset of that figure. While in general the magnetization vanishes at T_c, with an exponent smaller than unity, this is not the case for our very thin films. We therefore define two critical temperatures as shown in the inset and plot both in figure 4.19b. We note that it is T_c, the temperature at which the Kerr signal vanishes, which smoothly extrapolates to the thick films limit and corresponds to previously published data on 3-dimensional $SrRuO_3$ films.[17] Both T_e and T_c vanish below 4 ML. Defining a distance: $\zeta \equiv (T_c - T_e)/T_c$, we note that ζ increases with decreasing film thickness, especially below $\sim$9 ML. This may point to the fact that the transition from ferromagnetic to non-ferromagnetic films with decreasing thickness is a first order transition occurring at T_e with T_c being a mean field transition. In fact, the lower temperature data in the $\theta_K(T)$ extrapolates very close to T_c rather than T_e.

We next determine the magnetic anisotropy angle, $\Phi = \cos^{-1}(\theta_K^R(T)/\theta_K^S(T))$ as demonstrated by the insert in figure 4.19c. Φ as a function of the film thickness is plotted in figure 4.19c. We note that Φ decreases from 22° in the case of 22 ML film, which is close to the value in thick films,[37] to 14° in the 4 ML film. Applying this trend to thinner films would imply that if they were ferromagnetic, the magnetic easy axes would have been even more out-of-plane, and thus any ferromagnetic moment would have been easily detected in the zero field warmup measurements.

In figure 4.19d the magnitude of the coercive field is plotted. The coercive field reaches a maximum for the 9 ML thick film and is lower for both thinner and thicker films.

4.6 Conclusions

The results of the high temperature XRD measurements unambiguously demonstrate that a $SrRuO_3$ (110) layer grown coherently on $SrTiO_3$ (001) substrate does not undergo a tetragonal to cubic transition and remains tetragonal at temperatures up to 730 °C. The tetragonal unit cell allows us to explain single domain growth of $SrRuO_3$ films on miscut $SrTiO_3$ substrates. In step flow growth mode, growing species tend to attach to the steps due to the larger diffusion length as compared to the terrace length of the substrate. For a tetragonal unit cell where $c > a = b$, $SrRuO_3$ will tend to align its c-axis along the steps. If the step edges run only along $SrTiO_3$ [100] or [010] directions

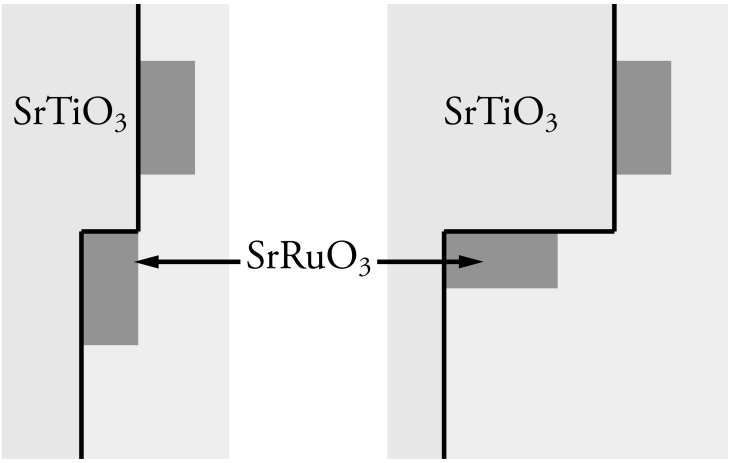

Figure 4.20: *The growth of $SrRuO_3$ depends on the direction of the $SrTiO_3$ step edges with respect to the $SrTiO_3$ crystal lattice. If the step edges run only along $SrTiO_3$ [100] or [010] directions then a single domain $SrRuO_3$ layer is formed, as is depicted in the left figure, because the $SrRuO_3$ will allign its long axis along the steps. When the step edges run at some arbitrary angle with respect to the [100] or [010] of $SrTiO_3$ the result will be a twinned film, since the $SrRuO_3$ can now arrange its long axis along both directions as shown on the right side.*

then a single domain $SrRuO_3$ layer is formed. On the other hand, if the step edges run along a direction rotated by some angle from [100] or [010] directions, $SrRuO_3$ will attach to steps with its longer unit cell axis parallel to the steps resulting in twinned structure due to the serrated nature of the step edge, as was already observed by Gan *et al.*[38] These two forms of growth are illustrated in figure 4.20. $SrRuO_3$ layers on substrates with low miscut angles exhibit twinned structures due to large length of the substrate terraces as compared to the diffusion length of $SrRuO_3$, which results in island growth. In this regime $SrRuO_3$ tetragonal unit cell tends to align randomly along [100] and [010] directions of the $SrTiO_3$ substrate.

We further show that we can grow $SrRuO_3$ thin films on $SrTiO_3$ under various conditions and conclude that this material exhibits a range of properties, due to a subtle change in stoichiometry on the ruthenium site, related to the oxidation conditions during deposition. Resistivity, X-ray diffraction, UPS and XPS all seem to indicate that this change in behavior is due to a changing electron-electron correlation, although we also point out that contributions from inelastic processes at vacancy sites as well as surface states cannot be ignored. These results shed light on the well-known sensitivity of the properties of $SrRuO_3$ to its synthesis conditions. Equally important, they suggest a clear path to more quantitative comparisons with theory.

In the last part of this chapter we have shown that in ultrathin films of $SrRuO_3$ itinerancy and ferromagnetism disappear at a critical film thickness between 3 and 4 monolayers. While a MIT could also happen if there are subtle rotations of the oxygen

octahedra rendering the unit cell symmetry tetragonal or even cubic for extremely thin films, this cannot be the case for our fully strained films since the observed MIT is abrupt while strained films will relieve the strain gradually with increasing thickness. A strong deviation from thick films behavior that begins around 9 ML may either indicate a 2D to 3D transition, or a change in the order of the transition to the ferromagnetic state. At that thickness transport is 2D dominated with a weak localization increase in the resistance at low temperatures.

Bibliography

1. B. Nagaraj, S. Aggarwal, and R. Ramesh, Journal of Applied Physics **90**, 375 (2001).
2. G. Rijnders, D. H. A. Blank, J. Choi, and C.-B. Eom, Applied Physics Letters **84**, 505 (2004).
3. J. Choi, C. B. Eom, G. Rijnders, H. Rogalla, and D. H. A. Blank, Applied Physics Letters **79**, 1447 (2001).
4. W. Siemons, G. Koster, A. Vailionis, H. Yamamoto, D. H. A. Blank, and M. R. Beasley, Physical Review B **76**, 075126 (2007).
5. A. Vailionis, W. Siemons, and G. Koster, Applied Physics Letters **91**, 071907 (2007).
6. C. W. Jones, P. D. Battle, P. Lightfoot, and W. T. A. Harrison, Acta Crystallographica Section C **45**, 365 (1989).
7. B. J. Kennedy and B. A. Hunter, Physical Review B **58**, 653 (1998).
8. J.-P. Maria, H. L. McKinstry, and S. Trolier-McKinstry, Applied Physics Letters **76**, 3382 (2000).
9. H.-D. Kim, H.-J. Noh, K. H. Kim, and S.-J. Oh, Physical Review Letters **93**, 126404 (2004).
10. D. Toyota, I. Ohkubo, H. Kumigashira, M. Oshima, T. Ohnishi, M. Lippmaa, M. Takizawa, A. Fujimori, K. Ono, M. Kawasaki, et al., Applied Physics Letters **87**, 162508 (2005).
11. D. Toyota, I. Ohkubo, H. Kumigashira, M. Oshima, T. Ohnishi, M. Lippmaa, M. Kawasaki, and H. Koinuma, Journal of Applied Physics **99**, 08N505 (2006).
12. B. Dabrowski, O. Chmaissem, P. W. Klamut, S. Kolesnik, M. Maxwell, J. Mais, Y. Ito, B. D. Armstrong, J. D. Jorgensen, and S. Short, Physical Review B **70**, 014423 (2004).
13. P. A. Cox, R. G. Egdell, J. B. Goodenough, A. Hamnett, and C. C. Naish, Journal of Physics C: Solid State Physics **16**, 6221 (1983).
14. A. Georges, G. Kotliar, W. Krauth, and M. J. Rozenberg, Reviews of Modern Physics **68**, 13 (1996).
15. M. Imada, A. Fujimori, and Y. Tokura, Reviews of Modern Physics **70**, 1039 (1998).

16. J. S. Dodge, E. Kulatov, L. Klein, C. H. Ahn, J. W. Reiner, L. Miéville, T. H. Geballe, M. R. Beasley, A. Kapitulnik, H. Ohta, et al., Physical Review B **60**, R6987 (1999).

17. L. Klein, J. S. Dodge, C. H. Ahn, J. W. Reiner, L. Mieville, T. H. Geballe, M. R. Beasley, and A. Kapitulnik, Journal of Physics: Condensed Matter **8**, 10111 (1996).

18. A. P. Mackenzie, J. W. Reiner, A. W. Tyler, L. M. Galvin, S. R. Julian, M. R. Beasley, T. H. Geballe, and A. Kapitulnik, Physical Review B **58**, R13318 (1998).

19. G. Herranz, B. Martínez, J. Fontcuberta, F. Sánchez, M. V. García-Cuenca, C. Ferrater, and M. Varela, Applied Physics Letters **82**, 85 (2003).

20. G. Koster, B. L. Kropman, G. J. H. M. Rijnders, D. H. A. Blank, and H. Rogalla, Applied Physics Letters **73**, 2920 (1998).

21. Q. Gan, R. A. Rao, C. B. Eom, L. Wu, and F. Tsui, Journal of Applied Physics **85**, 5297 (1999).

22. G. Cao, S. McCall, M. Shepard, J. E. Crow, and R. P. Guertin, Physical Review B **56**, 321 (1997).

23. J. W. Reiner, Ph.D. thesis, Stanford University (2002).

24. J.-P. Maria, S. Trolier-McKinstry, D. G. Schlom, M. E. Hawley, and G. W. Brown, Journal of Applied Physics **83**, 4373 (1998).

25. X. D. Wu, S. R. Foltyn, R. C. Dye, Y. Coulter, and R. E. Muenchausen, Applied Physics Letters **62**, 2434 (1993).

26. Q. Gan, R. A. Rao, C. B. Eom, J. L. Garrett, and M. Lee, Applied Physics Letters **72**, 978 (1998).

27. J. Shin, S. Kalinin, H. Lee, H. Christen, R. Moore, E. Plummer, and A. Baddorf, Surface Science **581**, 118 (2005).

28. J. Kim, J. Chung, and S.-J. Oh, Physical Review B **71**, 121406 (2005).

29. J. Okamoto, T. Mizokawa, A. Fujimori, I. Hase, M. Nohara, H. Takagi, Y. Takeda, and M. Takano, Physical Review B **60**, 2281 (1999).

30. M. Nakahara, S. Tsunekawa, K. Watanabe, T. Arai, T. Yunogami, and K. Kuroki, Journal of Vacuum Science and Technology B **19**, 2133 (2001).

31. W. E. Bell and M. Tagami, Journal of Physical Chemistry **67**, 2432 (1963).

32. A. F. Ioffe and A. R. Regel, Programmable Semiconductors **4**, 237 (1960).

33. P. B. Allen, H. Berger, O. Chauvet, L. Forro, T. Jarlborg, A. Junod, B. Revaz, and G. Santi, Physical Review B **53**, 4393 (1996).

34. K. Fujioka, J. Okamoto, T. Mizokawa, A. Fujimori, I. Hase, M. Abbate, H. J. Lin, C. T. Chen, Y. Takeda, and M. Takano, Physical Review B **56**, 6380 (1997).

35. I. H. Inoue, Y. Aiura, Y. Nishihara, Y. Haruyama, S. Nishizaki, Y. Maeno, T. Fujita, J. G. Bednorz, and F. Lichtenberg, Physica B **223-224**, 516 (1996).

36. S. D. Bader, Journal of Magnetism and Magnetic Materials **100**, 440 (1991).

37. G. Herranz, N. Dix, F. Sánchez, B. Martínez, J. Fontcuberta, M. V. García-Cuenca, C. Ferrater, M. Varela, D. Hrabovsky, and A. R. Fert, Journal of Applied Physics **97**, 10M321 (2005).

38. Q. Gan, R. A. Rao, and C. B. Eom, Applied Physics Letters **70**, 1962 (1997).

Chapter 5

Tetragonal CuO

Because of its relative simplicity, CuO is a candidate compound to study electron correlation effects and the influence of correlation on the electronic structure of transition metal compounds, in particular high temperature cuprate superconductors. In the cuprate superconductors the conductivity takes place in the copper oxide planes, which are sandwiched between charge reservoir layers. These planes have the composition CuO_2 and are arranged in a square pattern with the copper atoms on the corners and the oxygen atoms on the vertices between them. If another copper atom was placed in the middle of such a square a CuO rock salt plane would be created. If the charge reservoir layers were then removed and every second layer was given an offset of a Cu—O bond length, a three dimensional CuO rock salt structure would result, which would be a very interesting 3D potential model system with which to study the properties of high-T_c compounds.

There are, however, two problems: the proposed rock salt structure is not a stable phase of copper oxide, and the resulting structure would be a Mott insulator. To overcome these problems we have used epitaxial strain to force the CuO to grow in a tetragonal rock salt structure and studied the properties of this new tetragonal phase. The structural parameters were determined by using RHEED and x-ray photoemission diffraction. We had to resort to *in situ* measurement of the crystal structure because the films tended to relax to the more stable monoclinic CuO phase. Measuring properties was further complicated by the limited thickness ($\sim$2 nm) for which the tetragonal phase can be stabilized. Subsequently we studied the electronic structure with XPS and UPS. By comparing with stable copper oxides we have determined the Cu has a charge of +2 and that the tetragonal structure is more ionic than the monoclinic phase. To dope the material we have deposited overlayers to provide charge transfer to the CuO. Leaving aside the question of whether these electrons are localized or delocalized, we observe signs that the CuO is doped with electrons in this process. No Fermi edge was measured on these samples and when taken out of vacuum the alkali metals were found to have reacted with air, undoing any charge transfer effect. A UHV transfer chamber and a UHV, thin film scanning physical property measurement system are under development in our laboratory that will ameliorate such problems.

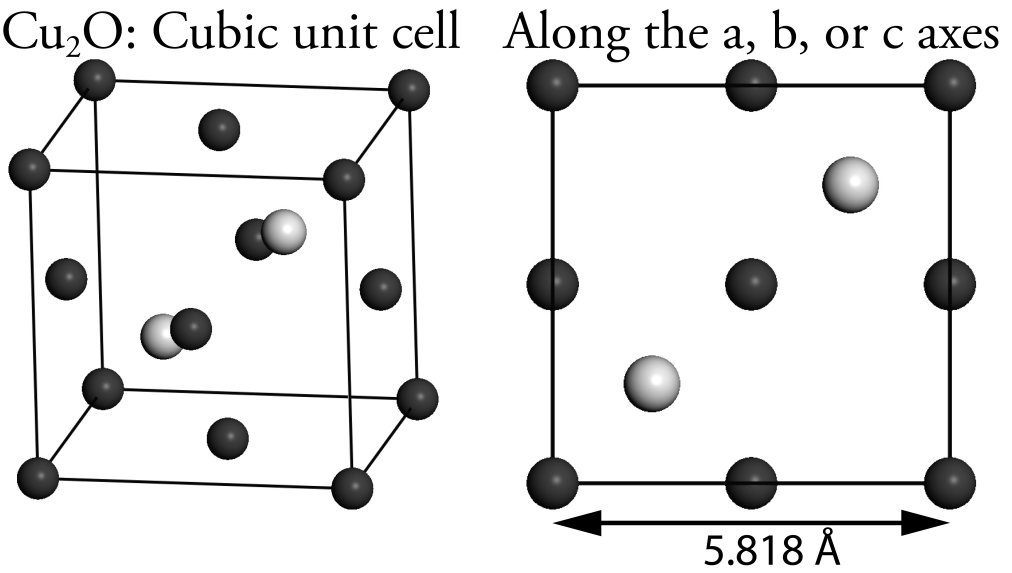

Figure 5.1: *An orthographic projection of the unit cell of cuprite (Cu_2O) is given on the left. The view along one of the crystal axes, together with the lattice parameter, is displayed on the right. Oxygen is represented by the larger lighter colored spheres and copper by the smaller darker colored spheres.*

This chapter describes these efforts and starts out with a general description of the well known stable oxides that can be formed with copper. The results of our experiments will be presented subsequently, followed by a discussion of the results and the conclusions.

5.1 The bulk oxides of copper

Copper can be progressively oxidized to form a number of oxides. It is important to know the properties of these oxides when a new phase is to be discerned. In this section the bulk structural, electronic, and magnetic properties of the natural oxides are summarized.

5.1.1 Structural properties

Copper metal has a face-centered-cubic (Fm-$3m$) lattice with a unit cell parameter of 3.604 Å,[1] which results in a Cu-Cu distance of 2.55 Å for nearest neighbors.

When copper is oxidized it first gives up one electron to become Cu^+ and forms Cu_2O, which is called cuprite and has space group Pn-$3m$. Cu_2O has a highly symmetric crystal structure: a cubic unit cell with a lattice parameter of 4.268 Å.[2] There are six atoms per unit cell; the oxygen atoms form a body-centered-cubic lattice and

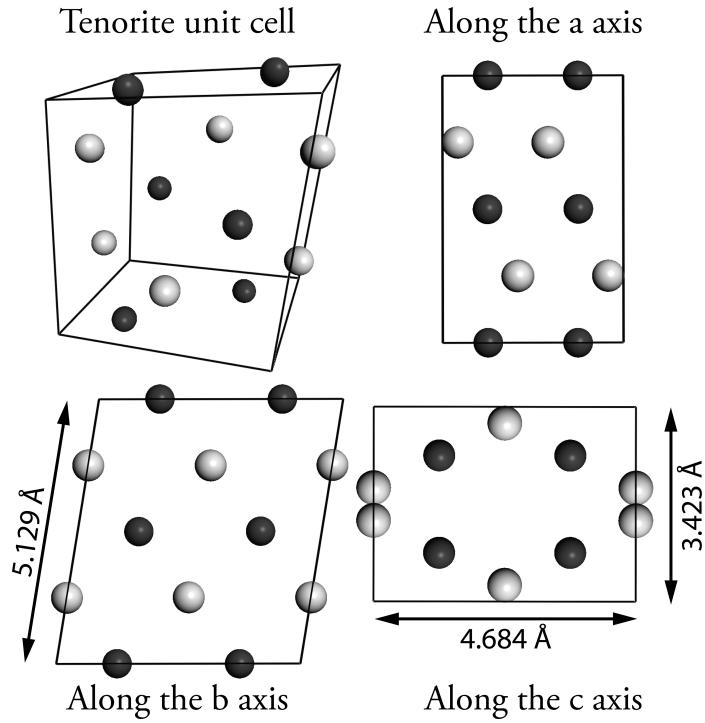

Figure 5.2: *A 3D image of the unit cell of tenorite (CuO) is given in the upper left corner. Views along each of the crystal axes, together with the lattice parameters, are also displayed. The copper has a valence state of 2+ in this structure. Oxygen is represented by the larger lighter colored spheres and copper by the smaller darker colored spheres.*

the copper atoms are on the vertices of a tetrahedron around each oxygen atom. A schematic representation of the unit cell is shown in figure 5.1 on the preceding page.

When Cu_2O is oxidized further copper becomes Cu^{2+} and the final composition is CuO, which is also known as tenorite and has space group $C2/c$. CuO has a monoclinic unit cell and each atom has four nearest neighbors of the other kind: the oxygen atoms are in the center of a distorted copper tetrahedron and the copper atoms are in the center of oxygen rectangles.[3] The unit cell of CuO is depicted in figure 5.2.

Between Cu_2O and CuO there is another phase that can form, namely Cu_4O_3 or paramelaconite. In this metastable phase the copper ions have a mixed valence: some are 1+ and some are 2+. Datta and Jeffrey,[4] O'Keeffe and Bovin,[5] and Morgan *et al.*[6] have determined that the unit cell has tetragonal symmetry, space group $I4_1/amd$, with $a = 5.818$ and $c = 9.894$ Å and unit cell contents $Cu_2^{2+}Cu_2^{1+}O_3$.

We will not consider further oxidation of the Cu to 3+, because of the following arguments, which were proposed by Geballe and Koster.[7] Those authors compare Cu in a crystal lattice to Cu in a aqueous solution, a comparison that is allowed because in both the crystal lattice and the aqueous solution the cations are coordinated by

Property	Cu	Cu_2O	Cu_3O_4	CuO
Symmetry	Cubic	Cubic	Tetragonal	Monoclinic
Space group	$Fm\text{-}3m$	$Pn\text{-}3m$	$I4_1/amd$	$C2/c$
Lattice constants (Å)	$a = 3.604$	$a = 5.818$	$a = 5.818$	$a = 4.6837$
			$c = 9.894$	$b = 3.4226$
				$c = 5.1288$
				$\beta = 99.54°$
Shortest Cu–Cu (Å)	2.55	3.02	2.92	2.90
Shortest Cu–O (Å)	n/a	1.84	1.87	1.95
Shortest O–O (Å)	n/a	3.68	2.56	2.62

Table 5.1: *Structural properties of the four phases of copper and copper oxide that were mentioned in the text. The symmetry of the unit cell, the space group, the lattice parameters and the shortest calculated bond lengths between atoms are given. For comparison, the Cu—O bonds in the CuO_2 planes of $La_{2-x}Sr_xCuO_4$ have a length of 1.89 Å.*

oxygen ions. In an aqueous solution one can use the electrode potential to calculate the energy needed to put a hole on the Cu. The standard electrode potential for $Cu^{3+} + e^- = Cu^{2+}$, $E(0) = +2.4$ eV is very high.[8] On the other hand, the standard electron potential for $Cu^{2+} + e^- = Cu^{1+}$ is low, $E(0) = -0.15$ eV indicating that Cu^{2+} can easily coexist with Cu^{1+}. In crystalline materials other energies need to be considered, but the ionic energies will be the largest. Therefore those authors conclude that Cu3+ does not play a significant role in the dynamics of copper compounds.

The unit cell parameters and the nearest neighbor distances for all four materials are given in table 5.1.

5.1.2 Electronic properties

Copper metal is a very good conductor and at room temperature has a resistivity of 1.7 $\mu\Omega$ cm. When copper is oxidized this conductivity quickly disappears. For Cu_2O values of 3×10^8 $\mu\Omega$ cm are reported, for Cu_4O_3 6.2×10^8 $\mu\Omega$ cm, and for CuO the resistivity is around 10^9 $\mu\Omega$ cm,[9] which were interpreted as the intrinsic values.

The band structure of Cu_2O is well understood and many calculations are available in literature.[10,11,12] Cu_2O has a full Cu $3d$ ($3d^{10}$) shell and is a model semiconductor with a band gap of 2.1 eV.[13] Due to the full $3d$ band, band theory predicts the electronic structure of Cu_2O accurately, because the generated electrons have no open-shell $3d$ electrons or holes with which to correlate. PES spectra of Cu_2O are well understood.

CuO on the other hand has an open Cu $3d$ shell ($3d^9$). Simple band theory predicts, in this case, that CuO should be metallic.[14] Electron correlation is, in fact, the reason CuO is a Mott insulator with a correlation gap of 1.4 eV.[15,16]

A classical way to determine whether a material is an insulator or a metal is to measure the conductivity as a function of temperature. In the case of an insulator the *dc* conductivity will vanish at low temperatures and when the material is a metal it will not. The vanishing conductivity in insulators occurs because the electronic

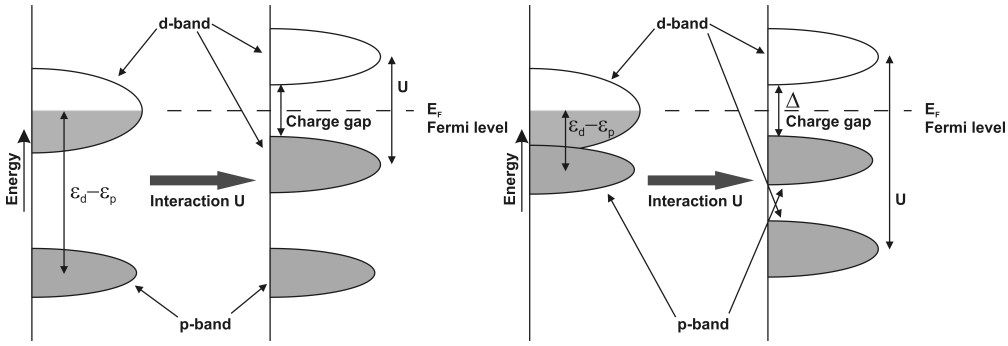

Figure 5.3: *Schematic illustration of the energy levels for a Mott-Hubbard insulator (left) and a charge-transfer insulator (right). The interaction on the d-site results in a splitting of the d-band and a charge gap formed by the upper and lower Hubbard band in the Mott-Hubbard insulator case or the upper Hubbard band and the p-band in the charge-transfer case. After Imada, Fujimori, and Tokura.* [17]

charges in these materials cannot flow freely when a *dc* electric field is applied, but instead undergo polarization. Conventional electronic structure techniques do not yield the right answer in all cases as they do not take strong electron correlation effects into account. In classical physics the difference in behavior when cooling down was explained by looking at the state of the electronic charges: they are either *bound* or *free*, corresponding to the Lorentz model for insulators and Drude model for metals respectively. When quantum physics is considered the distinction between the two states is no longer so obvious. The most used model to calculate electronic properties is the electronic band model: the band structure and the position of the Fermi level determine the behavior of the material.[19] In many materials, such as ionic insulators, simple metals, and some semiconductors, the band structure model and the related Fermi liquid description provide a good explanation of their physical properties. Insulators have only filled and empty bands in the band model, whereas metals have one or more partially filled bands. The assumption made in the band model is that electron interaction is limited to weak interactions. When Coulomb interactions become dominant in a system, immobilization of the electrons can occur for certain band fillings: these are commensurate fillings, for example $\frac{1}{2}$ filling. The insulators for which this is the case are called Mott insulators (after N.F. Mott who first described these materials in 1949).[20] Examples of Mott insulators are GaAs quantum wires, organic Bechgaard salts, undoped high-temperature superconductors,[21] and transition metal compounds including CuO. The interactions between the electrons can lead to novel phases which are strongly influenced by the carrier concentration as varied by doping away from half filling; an overview is provided by Imada, Fujimori, and Tokura.[17]

In a band insulator the conductivity is blocked by the Pauli exclusion principle: the electrons cannot move because the bands are fully filled (two electrons per unit cell). In a Mott insulator charge conduction is blocked by Coulomb repulsion. Every site contains a single electron, so when a second electron tries to hop to another site it

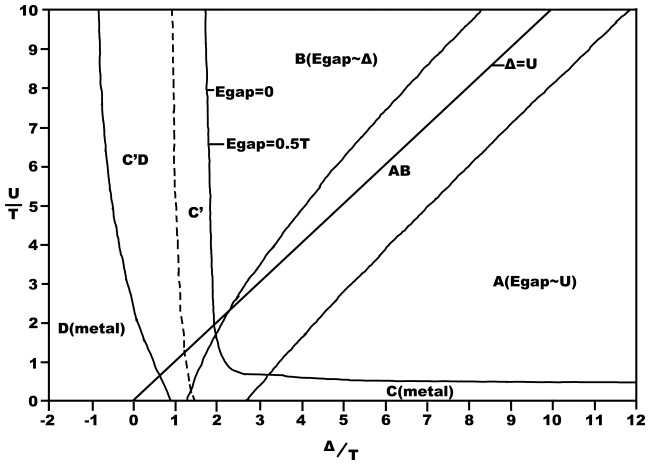

Figure 5.4: *The phase diagram by Zaanen, Sawatsky and Allen[18] classifies the various regions as a function of U and Δ. The various regions are: (A) The Mott-Hubbard insulators, where the energy gap (U) is formed by the d-band. Holes and electrons have a d character and are both heavy; (B) Charge-transfer insulators, where the energy gap (Δ) is formed by the p-band and the upper Hubbard band and is proportional to the electronegativity of the anion. Holes are light (p-band) and electrons are heavy (d-band); (AB) The intermediate region between the previous two, where holes are of intermediate mass and electrons are heavy; (C) d-band metals, where electrons and holes are both heavy; (D) p-type metals, which have holes in the anion valence band (light holes); (C'D) Intermediate region between the previous two regions.*

encounters the electron that was already there. This results in electron-electron repulsion, and when this repulsion is strong enough (roughly when the Coulomb interaction is larger than the bandwidth) all charges are fixed in the material, resulting in an insulator.

A good way to describe materials in which correlation dominates the transport properties is the Mott-Hubbard model. The Mott-Hubbard model proposes that charge fluctuations (with energy U) of the type $d_i^n d_j^n \leftrightarrow d_i^{n-1} d_j^{n+1}$ (where i and j label transition-metal sites) form the band gap; for CuO this would be $d_i^9 d_j^9 \leftrightarrow d_i^8 d_j^{10}$. This is correct for the light transition metal compounds, such as those of Ti and V. For the Co, Ni and Cu compounds however the gap does not seem to be a d–d gap, but is directly related to the electronegativity of the anion and is therefore of a charge transfer type.[22] This type of charge fluctuation does not involve U, but the charge transfer $d_i^n \leftrightarrow d_i^{n+1}\underline{L}$ (for CuO: $d_i^9 \leftrightarrow d_i^{10}\underline{L}$ with energy Δ), where $\underline{L}$ denotes a hole in the anion (oxygen in CuO) valence band. A schematic illustration of the energy levels for Mott-Hubbard and charge transfer insulators is given in figure 5.3 on the preceding page. In going from lighter to heavier transition-metal elements, the d level is lowered and therefore Δ is decreased, whereas U is increased because the spatial extend of the d orbital shrinks with the atomic number. This results in compounds containing a light transition-metal to become Mott-Hubbard insulators, whereas compounds containing a heavy transition

metal become charge-transfer type insulators. The electronegativity of the anion only influences Δ, higher electronegativity means Δ is decreased. Zaanen, Sawatzky and Allen[18] constructed a phase diagram that orders $3d$ transition-metal compounds with respect to the energies U and Δ. This phase diagram is given in figure 5.4 on the preceding page. Whether doped carriers in a filling controlled system have oxygen p-band character or transition-metal d-band character is an important question in considering the transport properties of transition metal oxides. Doped holes have a d-band character in Mott-Hubbard insulators and a p-band character in charge-transfer insulators. Doped electrons have a d-band character in both cases, because the conduction band has a d character in both cases.

Ghijsen *et al.*[23] show by using PES techniques that tenorite is a charge transfer gap insulator. NiO has a rocksalt structure and is also a charge transfer gap insulator, it can therefore be expected that CuO in a rock salt structure will be a charge transfer gap insulator as well. A summary of the electronic parameters of the oxides can be found in table 5.2.

Photoemission spectra

A direct way to measure the band structure is by performing PES. This section will describe the core level photoemission spectra of Cu, Cu_2O and CuO. It will focus on the $2p$ doublet of Cu, since it carries most information about the oxidation state of copper and on every sample made as part of this work these peaks have been measured. Examples of these spectra are given in figure 5.5 on the next page. For Cu and Cu_2O only two peaks appear: the $2p_{\frac{3}{2}}$ and the $2p_{\frac{1}{2}}$, which can be linked to $2p^5 3d^{10}$ final state. For CuO two extra satellite peaks appear, which are characteristic of the formation of a $2p^5 3d^9$ final state. Such satellite structures are also visible in the spectra of the copper dihalides[32] and nickel metal.[33] The ground state of copper is a $3d^9$ state and the main peaks related to the $3d^{10}$ state are not expected to have any intensity. Due to the hybridization of the bands the oxygen can donate an electron to the copper to create a lower energy state, which is denoted by an $\underline{L}$ indicating a hole on the ligand. The main peaks are therefore denoted as $2p^5 3d^{10}\underline{L}$ final states. The main peak is also

	Cu	Cu_2O	CuO
Resistivity at 300 K ($\mu\Omega$ cm)	1.7	6.2×10^8	10^9
Bandgap (eV)	n/a	2.1	1.4
Cu $2p$ binding energy (eV)	932.4 ± 0.1	932.3 ± 0.2	933.5 ± 0.3
O $1s$ binding energy (eV)	n/a	530.3 ± 0.3	529.5 ± 0.2

Table 5.2: *Summary of the electronic properties of Cu, Cu_2O, and CuO in numbers: the resistivity at room temperature, the bandgap, and the positions of important core level XPS lines. For CuO there are additional parameters related to the strong electron correlation: the copper–oxygen charge-transfer energy $\Delta = 1$ eV, the d–d Coulomb interaction $U = 7$ eV, and the ligand–d hybridization $T = 2.4$ eV.*[23,24] *For the XPS lines an average of the values found in literature is given and the standard deviation.*[23,25,26,27,28,29,30,31]

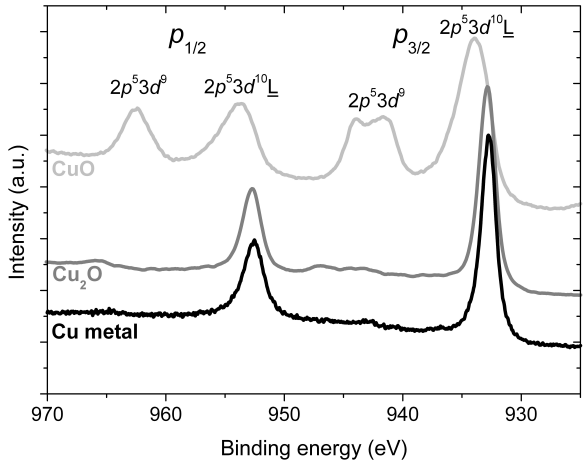

Figure 5.5: *Photoemission spectra of Cu, Cu_2O, and CuO (tenorite). For both Cu as well as Cu_2O only 2 peaks are visible, which are related to the $2p^5_{3/2}3d^{10}$ and the $2p^5_{1/2}3d^{10}$ final states, which have almost the same binding energy in both materials. The CuO spectrum is more complex and has 4 peaks due to the possibility of oxygen donating an electron to the copper 3d band. The final states for the CuO peaks are labeled in the figure. The largest peak is called the main peak and the smaller peak related to the ground state is called the satellite peak in the text. The peaks of the CuO are shifted to higher binding energy by more than 1 eV. They are also much broader than the peaks of the other two materials due to delocalized screening and multiplet splitting, which is explained in the text.*

a lot broader for CuO than it is for Cu or Cu_2O, which has been explained by Van Veenendaal and Sawatsky.[34,35] By performing calculations they show that there is a competition between screening electrons coming from local ligand atoms and electrons coming from ligand atoms of neighboring Cu metal ions to screen the charge on the Cu. This causes an extra contribution to the main peak, which shows up as a shoulder at higher binding energy in the case of CuO. The multiplet splitting in the $2p^5 3d^9$ satellite peak is more subtle and is the subject of many papers.[36,37]

5.1.3 Magnetic properties

The electrons in a Mott insulator cannot move, but their spins can still fluctuate. The spins usually arrange themselves in an antiparallel fashion, due to virtual charge fluctuations,[38] which leads to long-range antiferromagnetic ordering. The temperature at which this ordering takes place is the Néel Temperature (T_N).

The Néel temperatures for transition metal monoxide compounds with a rock salt structure are graphically represented in figure 5.6 on the facing page. The y-axis is scaled logarithmically and the Néel temperature increases exponentially with the transition element number. The Néel temperature for CuO does not follow this trend, but remember, CuO has a monoclinic structure, which could be the cause of the reduced transition temperature. If CuO could be forced into a rock salt structure its Néel

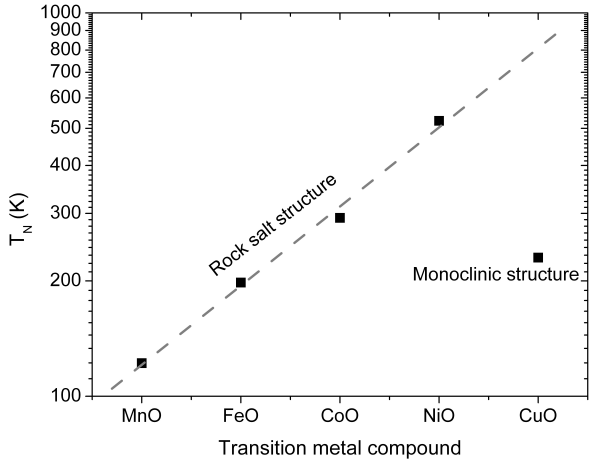

Figure 5.6: *An overview of the Néel temperatures for transition metal monoxides with a rock salt structure. T_N increases exponentially with each element up to NiO as indicated by the dashed line, which is a fit of the first four points. The T_N of the monoclinic CuO structure does not follow this trend, but is much lower. When a rocksalt structure of CuO is formed T_N might follow the trend and linear extrapolation predicts a T_N slightly higher than 800 K.*

temperature would be slightly higher than 800 K based on a linear extrapolation. A recent theoretical exploration of the Néel temperature in these materials was performed by Harrison with a tight-binding model.[39]

The Néel temperature in these materials in thin films is also a function of thickness, which has been observed both experimentally[40,41] as well as theoretically.[42] For NiO the Néel temperature is reduced from 520 K for bulk material to 470, 430, and 295 K for 20, 10 and 5 monolayer films respectively, as measured by x-ray absorption spectroscopy.[40] This thickness effect is due to uncompensated moments at the surface causing disorder and can be modeled as a finite-size effect.[43] The reduction of the Néel temperature with thickness is quite substantial in transition metal monoxides compared to other compounds.[44] This strong dependence in NiO can be qualitatively understood by looking at the crystal structure. In a rocksalt structure the nearest-neighbor (100) layers are not or hardly coupled via the superexchange interaction because of the 90° Ni-O-Ni bonds, while the next-nearest-neighbor layers are only coupled by one 180° superexchange path. Due to this weak coupling the bulk Néel temperature will only be reached for fairly thick layers of NiO. A similar dependence is to be expected for CuO when it is stabilized in a rock salt structure.

Measuring the Néel temperature or the magnetic properties of an antiferromagnetic thin film in general is not easy due to the antiparallel arrangement of the spins which means the long range magnetic signal averages to zero. The usual way of determining the Néel temperature for bulk samples is to measure heat capacity, a method which is not suitable for very thin films. A good example of heat capacity measurements on doped CuO is the work by Saito *et al.*[45] Another bulk technique is the use of neutron

diffraction to determine spin alignment and has to be performed at specialized facilities. However, more material than is present in our thin films is needed to gather reliable data. Bulk data of this type is available on a lot of transition metal compounds, for example the work by Roth on the transition metal monoxides.[46] In somewhat thicker films measuring the dc-susceptibility is a good option. After the transition to the antiferromagnetic state the susceptibility will drop sharply, which can be seen in CoO/SiO_2 multilayers by Ambrose and Chien.[43] For thinner films there are some synchrotron related techniques. The first one is x-ray absorption spectroscopy (XAS). Alders *et al.*[40] calculate that the Ni L_2-XAS in NiO is dependent on the presence exchange interaction. This way those authors measure the Néel temperature in NiO films as thin as 5 ML. The second synchrotron technique is x-ray magnetic linear dichroism spectroscopy (XMLD). Here linearly polarized x-rays are used to probe the expectation value of the square of the magnetic moment, $< M^2 >$, because linearly polarized photons have only axiality. Because linearly polarized light is used, in contrast to circularly polarized light, any uniaxial magnetic system can be measured, which includes antiferromagnets. In the right setup this technique measures only the top 2 nm of a film, making this a very suitable technique for very thin films. The merits of this technique were demonstrated by Stöhr and coworkers on a film of NiO.[47] The last technique we will discuss here is measuring the transition temperature by using the exchange bias effect. The exchange bias effect, which was discovered in 1956,[48] exists at the interface between a ferromagnet and an antiferromagnet. It will be discussed in more detail in the following paragraphs, since we will come back to it later in the chapter.

Ferromagnets have a large exchange parameter, but a relatively small anisotropy, which makes the ferromagnetic ordering stable at high temperatures, but the orientation may not be stable. Most ferromagnets have two equally favored magnetic directions which are collinear and lie along the so-called easy axis. Antiferromagnets on the other hand have a very large anisotropy and therefore have very stable orientations.

When an interface is formed between a ferromagnet and an antiferromagnet the exchange coupling can result in the existence of ferromagnetic behavior with stable order and high anisotropy.[49] This phenomena is called the exchange bias effect and influences the shape and position of the magnetic hysteresis loop. When a ferromagnet is grown on top of an antiferromagnet the exchange coupling between the two systems only leads to an increased coercivity of the ferromagnet. This is usually attributed to the increased coercivity of *interfacial spins* which need to be dragged around by the external field. However, the ferromagnetic hysteresis loop is still symmetric, indicating two equivalent easy directions.

When cooled down in a magnetic field on the other hand the hysteresis loop is no longer centered around zero magnetic field. These shifts are most easily observed when perfect interfaces are formed and the Néel temperature of the antiferromagnet is lower than the Curie temperature of the ferromagnet. In that case a magnetic field is applied to the heterostructure above the Néel temperature and the sample is then cooled down to below the Néel temperature in a magnetic field. In this case the layers of the ferromagnet closest to the interface will be pinned in a uniform direction and a shift in the hysteresis loop results.

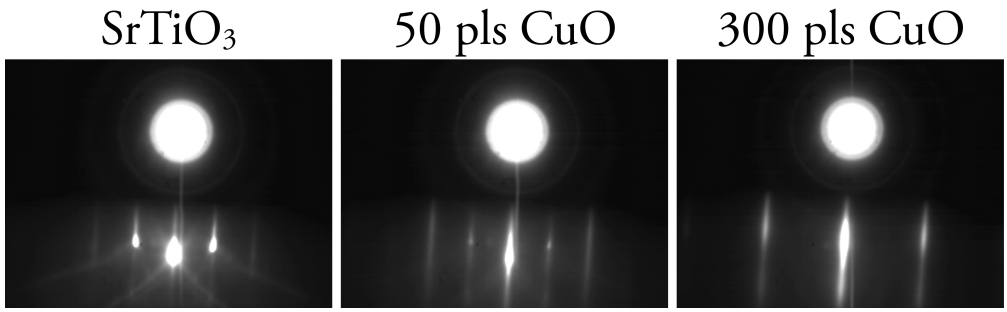

Figure 5.7: *The evolution of the RHEED spectrum during the growth of CuO on $SrTiO_3$ taken along the (01) direction of $SrTiO_3$ shows a transition from a clear 2D pattern for bare $SrTiO_3$ on the left to the streaky pattern of CuO on the right. 300 pulses of CuO corresponds to a 15 – 20 Å thick film.*

The condition of $T_N < T_C$ may not be satisfied in our materials system, because we do not know the Néel temperature of the new phase, and a more disordered system might result. This disorder can come from structural defects, but also from the formation of domains in the ferromagnet and the antiferromagnet.[50] The measurement can, therefore, be an average over many such domains and may not show a shift in the hysteresis loop. The magnitudes of the coercive and exchange bias fields are a function of the thickness of the antiferromagnetic layer, which is most likely due to a change in its domain structure.[51,52] Much work has been done recently on describing exchange bias effects at interfaces[53] and so far the Mauri-Siegmann model[54] seems to offer the best fit with observations. If a rock salt structure of CuO can be formed it might behave a lot like NiO, which is the transition metal compound closest to it. NiO is known to exhibit weak bias fields, probably due to the relatively small magnetocrystalline anisotropy (i.e., NiO is not a very hard antiferromagnet).

Measuring the Néel temperature by the exchange bias effect is further complicated by the so-called blocking temperature, T_b. At T_b the exchange bias field, i.e. the shift in the hysteresis loop, approaches zero and T_b is a measure for the thermal stability of the exchange bias. The blocking temperature is always lower than the Néel temperature and has been shown to be a function of the thickness of the antiferromagnetic layer.[55]

5.2 Epitaxially strained growth on $SrTiO_3$ and characterization

It is possible to grow CuO with a higher degree of symmetry (tetragonal) by depositing on $SrTiO_3$ and thereby making use of epitaxial strain. The next few sections offer an overview of the findings on this new tetragonal phase of CuO. The results on growth, structure, electronic properties, and magnetic properties are presented.

5.2.1 Growth

Samples were either grown on $SrTiO_3$ or on doped, conducting $SrTiO_3$, where the doping was 0.5% Nb. The latter offers the advantage of reduced charging when performing PES on the insulating CuO samples. Both kinds of substrates were TiO_2 terminated, as described in section 2.3.1 on page 13.

In order to stabilize the new phase it is of utmost importance to oxidize Cu to a 2+ state. This is accomplished by using a target of CuO and providing atomic oxygen with the source operating at 600 W with a flow of 2.5 sccm oxygen resulting in a background pressure in the system of 1.5×10^{-5} Torr. The temperature of the substrate was kept constant at 600 °C and the growth was monitored by RHEED. The RHEED patterns in figure 5.7 on the preceding page show a sequence of events in the case of perfect growth. A streaky pattern emerges from the CuO, without any 3D spots between the streaks. Figure 5.8 contains a pattern that shows what happens when the film relaxes to tenorite, which is clearly different from the new CuO phase.

When grown on dual terminated substrates the growth was found to be more 3D and the films relaxed to the tenorite phase at an earlier stage. Similar effects were observed on other substrate materials, such as $DyScO_3$ and $LaAlO_3$, where 3D growth patterns dominated. Those substrates are double terminated by nature and no known reliable methods exist to make them single terminated, an effort further complicated by the polar nature of these materials (for more information on polar materials see chapter 3 on page 27). These other substrates have different lattice parameters as well, which influence the stress put on the material.

The films were not always stable in atomic oxygen below 300 °C, when cooled after deposition. The films, it was found, would relax to tenorite when cooled to room temperature under deposition conditions. For this reason the atomic oxygen was switched off at 300 °C and the sample was cooled to room temperature in molecular oxygen ($\sim 10^{-5}$ Torr). This implies that the stability line for the tetragonal CuO when exposed to atomic oxygen lies at 300 °C.

The thickness of the tetragonal CuO samples is limited by a relaxation to the

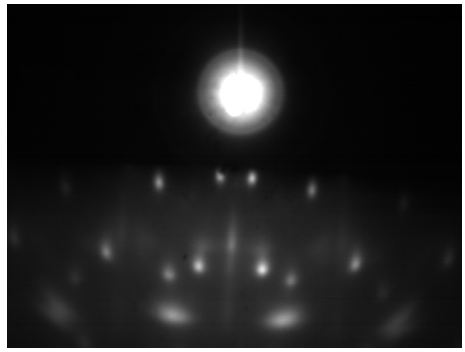

Figure 5.8: *The RHEED spectrum during the growth of tenorite CuO on $SrTiO_3$ taken along the (01) direction of $SrTiO_3$ showing clear 3D spots.*

tenorite phase when growing beyond a certain thickness. For most samples 300 laser pulses were used in the PLD process to guarantee a streaky RHEED pattern with no 3D spots. This corresponds to a layer thickness between 15 and 20 Å. AFM imaging confirms that thin samples are flat with the $SrTiO_3$ step structure still visible, whereas the samples that are thicker have *particles* on top, associated with the film growth process, that would cause a 3D pattern to appear.

5.2.2 Structural properties

To confirm the growth of a new phase the first thing to determine is its structure. The in-plane lattice parameters could be deduced from the RHEED spectra, which were taken during growth. The out-of-plane lattice parameter is more difficult to measure due to the limited amount of material with which to work. Through the application and simulation of XPD spectra we have been able to construct the unit cell of the new phase. First the in-plane and subsequently the out-of-plane parameters are discussed.

In-plane lattice parameters

To determine in-plane lattice parameters of the new phase RHEED spectra were used. Spectra taken along the $SrTiO_3$ (10) and (11) are shown in figure 5.9 on the next page, and since the lattice parameters of the $SrTiO_3$ are well known (3.905 Å cubic), those of the CuO can be calculated by comparing to $SrTiO_3$. When this data is taken at face value and this method is used on the spectra that are displayed, one calculates a distance of 1.92 Å along the $SrTiO_3$ (10) direction and 2.72 Å along the (11) direction. This suggests that the unit cell of the new CuO phase is 45 degrees rotated with respect to the $SrTiO_3$ if we assume a rock salt structure, i.e. the (11) direction of CuO is parallel to the (01) direction of $SrTiO_3$. The result would be a unit cell with as many atoms as the tenorite unit cell, but with only a quarter of the volume, and the Cu–O bond length would be 1.36 Å, a seemingly unphysical value. However, for a rock salt structure, in 3D as well as 2D, not all the diffraction peaks are allowed, as can be seen from the following calculations.

In a face centered crystal lattice every atom with coordinates (x, y) has one identical atom with coordinates $(x + \frac{1}{2}, y + \frac{1}{2})$. For every unit cell with n atoms there are $n/2$ groups of two atoms. The structure factor can be written as a summation of such groups of two:

$$F_{hk} = \sum_{n/2} \{ f_n \mathrm{e}^{2\pi \mathrm{i}(hx_n + ky_n)} + \mathrm{e}^{2\pi \mathrm{i}(h(x_n + \frac{1}{2}) + k(y_n + \frac{1}{2}))} \}$$

And can also be written as:

$$F_{hk} = [1 + \mathrm{e}^{\pi \mathrm{i}(h+k)}] \sum_{n/2} f_n \mathrm{e}^{2\pi \mathrm{i}(hx_n + ky_n)}$$

The part of the equation before the summation takes the value 2 if h and k are unmixed,

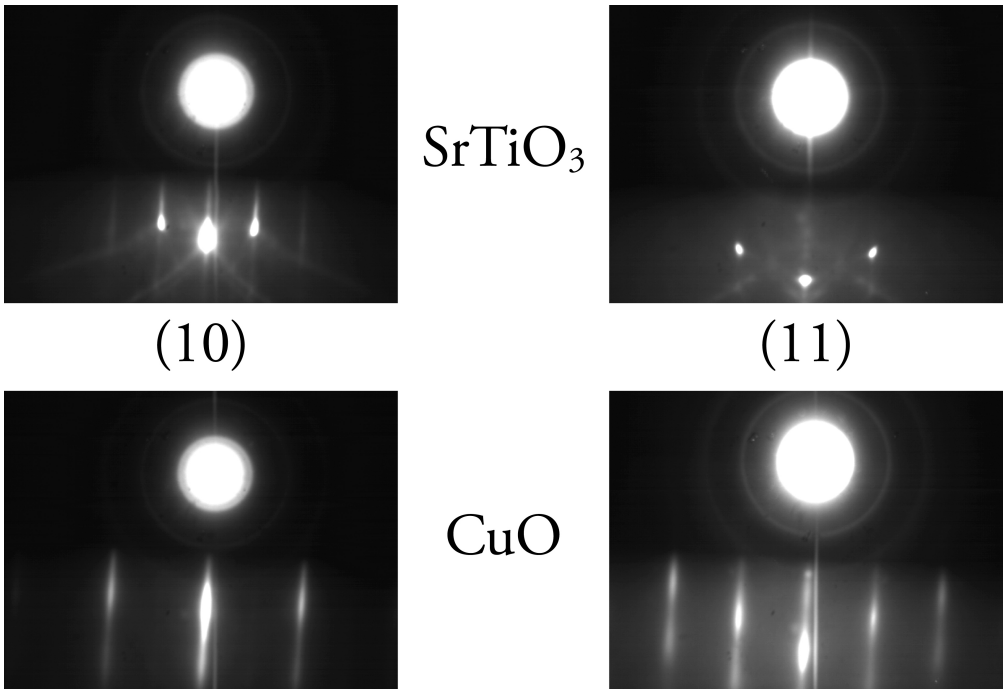

Figure 5.9: *The electron diffraction patterns of $SrTiO_3$ and CuO taken along their (10) and (11) directions. Even though the (10) reflection of CuO is not allowed as explained in the text, very faint lines at its position are usually visible. The patterns shown here are both fourfold symmetric when the sample is rotated around its azimuthal axis.*

both odd or both even, and 0 when they are mixed:

$$\text{h,k unmixed: } F_{hk} = 2\sum_{n/2} f_n \mathrm{e}^{2\pi \mathrm{i}(hx_n + ky_n)}$$

$$\text{h,k mixed: } F_{hk} = 0$$

In 3D the result is similar, but then for three dimensions: h, k, and l. The absence of l does make a difference though; the (330) reflection, for instance, would not be allowed in three dimensions, but in two dimensions it becomes (33) and is allowed. For the analysis of the RHEED patterns this results in the (01) reflection not being allowed, but the (11) is allowed and therefore the shortest spacing between the diffraction peaks now corresponds to the (11) direction.

Applying these insights allows us to calculate the correct in-plane lattice parameters. In the (11) direction of the $SrTiO_3$ substrate the (11) and (22) reflections of CuO are allowed, and along the (01) direction of the $SrTiO_3$ the (02) and (04) reflections of CuO are allowed. The CuO in-plane lattice parameters are exactly the same size as the $SrTiO_3$ underneath. This corresponds to a Cu–O bond length of 1.95 Å in-plane, a

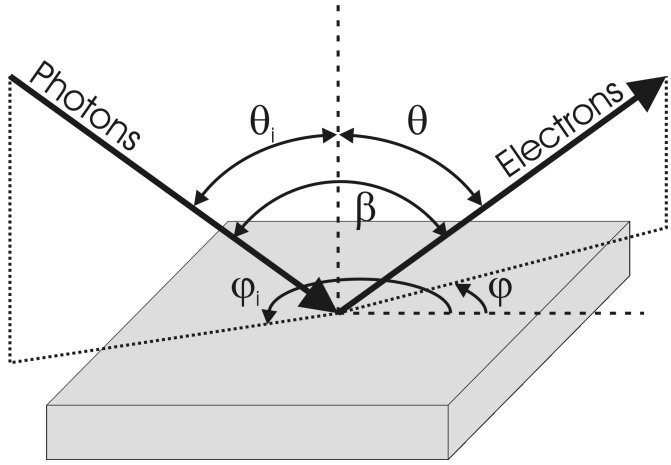

Figure 5.10: *A schematic layout of the XPD setup and the important angles, which are mentioned in the text. The angles the incident beam makes with respect to the sample have a subscript i. θ is the angle between the detector and the surface normal and φ is the angle between the detector and one of the in-plane crystal axes of $SrTiO_3$. In our setup only the sample moves and therefore $\theta + \theta_i = \beta = 45°$.*

number which corresponds well with values found in high T_c materials or in monoclinic CuO. If the unit cell were cubic this would result in a unit cell volume of 59.5 Å, still shy of the 81.1 $Å^3$ of tenorite. To solve this discrepancy the unit cell could be elongated along the out-of-plane direction, but based on the RHEED spectra alone we cannot draw any conclusions about the out-of-plane lattice constant, which is the subject of the next section.

Out-of-plane lattice parameters

To measure the out-of-plane lattice parameter we employed XPD (see section 2.4.1 on page 18). To verify that the technique would produce reliable results it was first applied to a conducting 0.5% Nb-doped $SrTiO_3$ substrate. For this measurement the energies were fixed on the Ti 2*p*, Sr 3*d*, and the O 1*s* peaks and a pass energy of 100 eV was set. The acceptance angle for electrons was 5 degrees and the peak heights were measured every 2° for θ and every 3° for ϕ resulting in a matrix of 3600 points. The results are displayed in figure 5.11 on the next page, and for each of the elements a clear modulation of intensity, as a function of angle, is visible. The simulations were performed with software by Abajo *et al.*[56] with the following key parameters:

- a cluster of 1247 atoms;
- incoming linear polarized light parallel to the surface;
- a surface potential of 10.5 eV;
- an electron inelastic mean free path of 23 Å for O and Ti, and 29 Å for Sr;

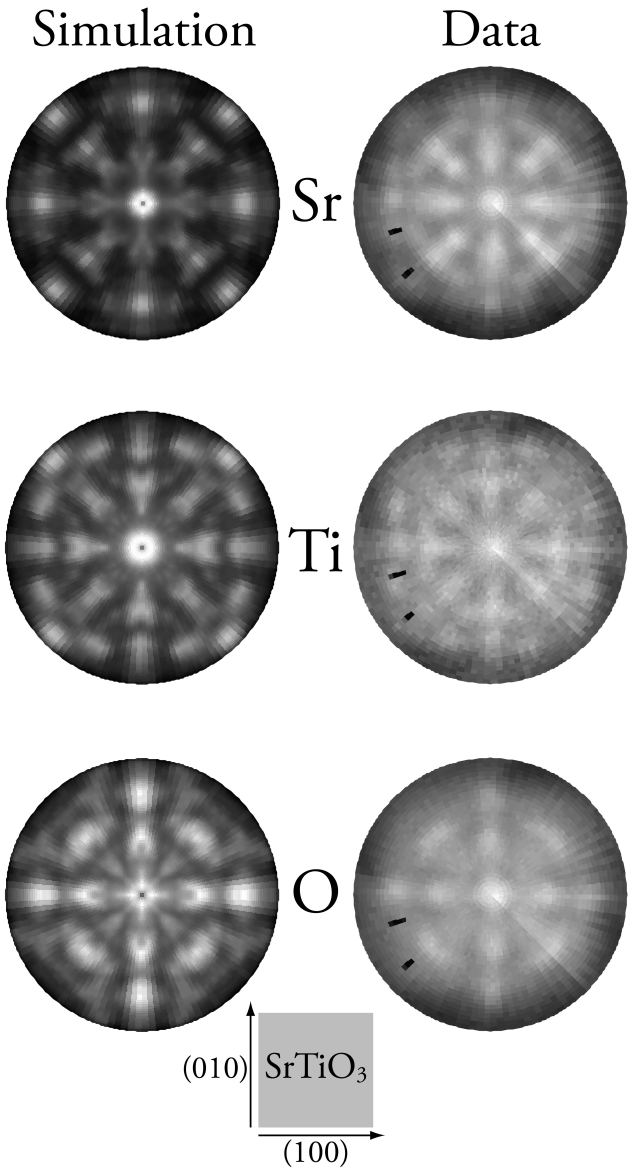

Figure 5.11: *Simulated and measured XPD patterns for each of the elements in $SrTiO_3$: Sr 3d, Ti 2p, and O 1s. The simulations were generated using the parameters mentioned in the text. The measurements were performed with the pass energy set at 100 eV and an acceptance angle of 5 degrees, in steps of 2° for θ and 3° for ϕ. The correspondence between the simulation and the measurement is good for low angles of θ, whereas some detail is lost in the measurements at high angles due to less than optimal alignment of the sample at high angles.*

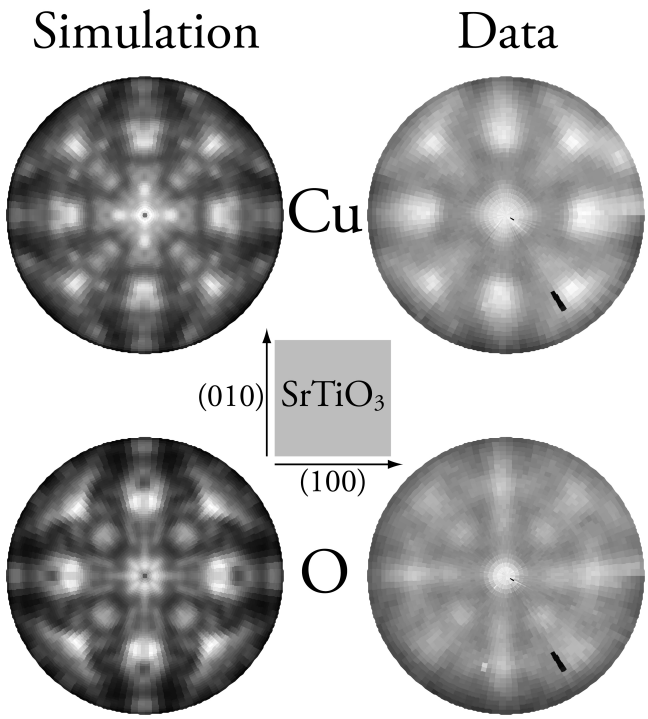

Figure 5.12: *XPD patterns for CuO measured (on the right) at two binding energies: the O 1s and the Cu $2p_{\frac{3}{2}}$ main line. The measurements were performed with the pass energy set at 100 eV and an acceptance angle of 5 degrees, in steps of 2° for θ and 3° for ϕ. Simulations of the CuO in tetragonal form are shown on the left, as calculated with the parameters mentioned in the text. The Cu signal comes solely from the film, whereas the O signal has a significant contribution from the substrate. The Cu pattern shows clear four-fold symmetry, which is not what would be expected from a single domain tenorite film.*

- 20 orders recursive iteration;
- a maximum orbital quantum number of 20;
- a sample temperature of 350 K;
- a Debye temperature of 400 K;
- an emission angle window of 5 degrees.

The values for the electron inelastic mean free path were determined with the aid of the NIST IMFP database.[57] The similarity between the simulations and the measured data is clearly visible, which validates the use of this technique.

The technique was then applied to CuO and two energies were measured: the O $1s$ and the Cu $2p$. For the O signal a mixture of the substrate and the film is to be expected since the escape depth of the electrons is higher than the thickness of

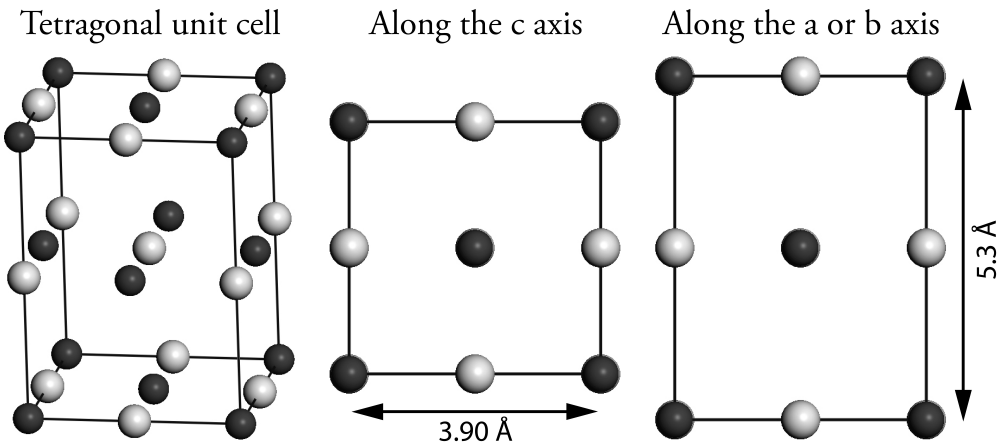

Figure 5.13: *The unit cell of the tetragonal phase of CuO as it is stabilized on $SrTiO_3$. An orthographic representation of the unit cell on the left and views along the c and a or b axes to the right of that. The lattice parameters are given along the respective directions. The Cu atoms are represented by the smaller darker colored spheres and the O atoms by the larger lighter colored ones.*

the CuO layer. The copper signal comes solely from the film because the substrate contains no copper. The copper pattern shows a fourfold symmetry as shown on the right in figure 5.12 on the preceding page, which is indicative of a fourfold symmetric unit cell, such as a rock salt structure. The simulation shown on the left of the figure looks strikingly similar to the measurement, which has been accomplished by using the following parameters:

- a unit cell with $a = b = 3.905$ and $c = 5.320$ Å;
- a rock salt structure with 8 atoms per unit cell;
- a cluster of 1505 atoms;
- incoming linear polarized light parallel to the surface;
- a surface potential of 10.5 eV;
- an electron inelastic mean free path of 10.5 Å for Cu, and 21 Å for O;
- 20 orders recursive iteration;
- a maximum orbital quantum number of 20;
- a sample temperature of 350 K;
- a Debye temperature of 400 K;
- an emission angle window of 5 degrees.

The unit cell dimensions mentioned above results in a unit cell volume of 81.1 $Å^3$ which is the same as for tenorite. Using the XPD data, the out-of-plane lattice parameter

cannot be determined more accurately than this. The shortest Cu–O bond length in this structure is 1.95 Å, which corresponds to the value found in tenorite. Due to the tetragonal structure the number of nearest neighbors for each Cu or O remains 4, whereas there would be 6 in the cubic rock salt structure. The shortest Cu–Cu and O–O bond lengths are 2.76 Å, a value that is in between the values found for the two in tenorite. A schematic drawing of the unit cell is given in figure 5.13 on the preceding page together with the lattice parameters.

5.2.3 Electronic properties

When the structure of CuO is changed from monoclinic to tetragonal we expect a change in the electronic structure of the material. This should influence the core electrons of copper and therefore the shape of the Cu $2p$ lines in XPS. The XPS spectra of the Cu $2p$ lines for both the tenorite as well as the tetragonal structure are presented in figure 5.14 on the following page. For tenorite we find 933.5 eV for the binding energy of the Cu $2p_{\frac{3}{2}}$ and 529.4 eV for the O $1s$, which corresponds well to values found in literature (see table 5.2 on page 83); the energies do not appear to change significantly in spectra of the tetragonal phase. Compared to the tenorite spectrum, the tetragonal CuO spectrum has a larger shoulder on the main peak at higher binding energy, a narrower satellite peak, and the spectral weight of the first satellite peak has shifted to lower binding energy. More precisely, when going from the monoclinic to the tetragonal phase the fwhm of the main peak increases from 3.6 to 4.1 eV, whereas the fwhm of the satellite peak decreases from 4.5 to 4.2 eV.

After exposure to air the top layer of the CuO was found to degrade to tenorite. This has been examined by using angle dependent XPS. In figure 5.15 on the following page, the spectra taken at 90 and 30 degrees (the angle between the detector and the sample surface) are plotted. At 90 degrees more electrons from greater depth reach the detector and the spectrum of the tetragonal phase is clearly visible. At 30 degrees the electrons come more from the top surface layer and a tenorite spectrum is measured. The top layer is therefore mostly tenorite, whereas the layer closest to the interface with $SrTiO_3$ is mostly tetragonal. When the sample is kept under vacuum after growth, the CuO is slowly reduced over a period of days. After four days the intensity of the satellite peaks are reduced to about half their size after deposition.

Now we turn to the valence bands of the tetragonal CuO. The valence bands were measured with He I radiation; the results are presented in figure 5.16 on page 97. The spectrum is very similar to that obtained on tenorite by other groups.[23,24,58,59,60] For example, there are no states at the Fermi level, which is as expected for an insulator. There are some notable differences though. The peak at low binding energy (∼1.9 eV), which is caused by both oxygen and copper,[61] is not as strong in our spectrum as it is in spectra of tenorite. The largest peak, caused mainly by copper, clearly consists of two separate peaks in our spectrum, which has not been observed before for tenorite. Calculations on the tenorite band structure show a splitting of this peak though[23,61] and in some measurements a clear shoulder is visible.[58] The peaks at 5.8 and 7.0 eV are both oxygen peaks and are also predicted by calculations.[61] The double peak feature at higher energy (10–13 eV), which also exists for tenorite, is a copper feature only

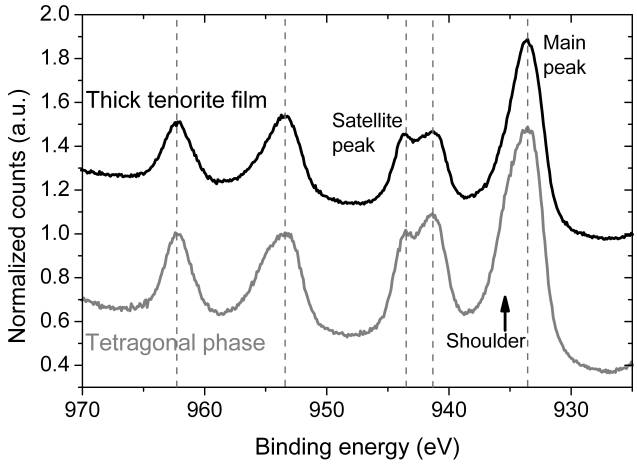

Figure 5.14: *The Cu 2p core level XPS spectrum of the tetragonal CuO looks significantly different from the tenorite spectrum. The most striking differences are the broadening of the main peak, the narrowing of the satellite peak, and the redistribution of weight in the satellite peak. The spectra have been normalized on the $2p_{\frac{1}{2}}$ peak and the tenorite spectrum has been given an offset for clarity.*

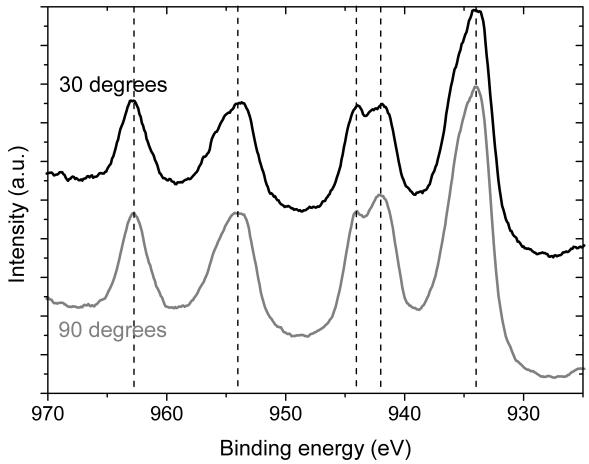

Figure 5.15: *Two Cu 2p core level XPS spectra taken on the same sample at two different angles with respect to the analyzer after exposure to air. At 90 degrees the sample normal faces directly towards the electron analyzer, whereas at 30 degrees there is a 60 degree angle between the surface normal and the electron analyzer. The spectrum taken at 30 degrees looks more like the tenorite spectrum from figure 5.14, although the width of the peaks is still different from those of tenorite. The two spectra are normalized to the intensity of the main peak and the spectrum taken at 30 degrees has been given an offset for clarity.*

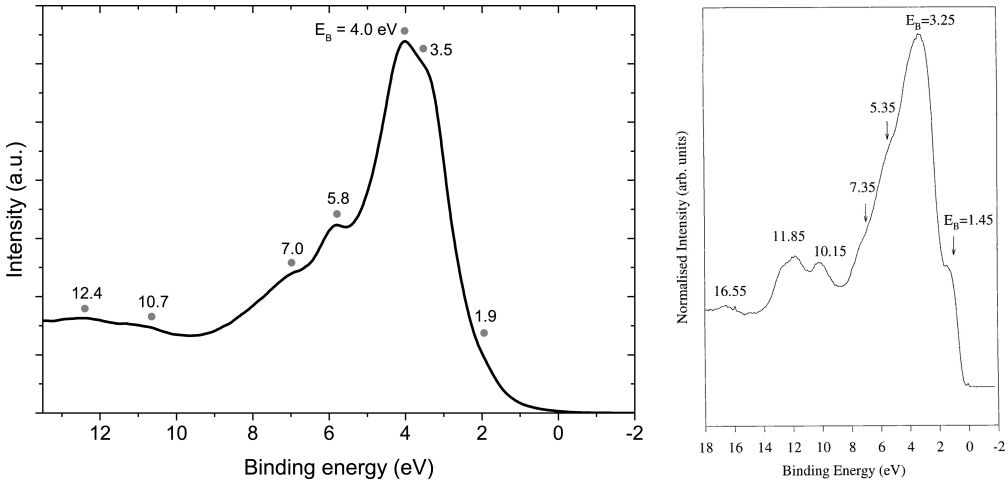

Figure 5.16: *The tetragonal CuO valence band spectrum, on the left, measured with HeI radiation. The Nb doped $SrTiO_3$ substrate contributes to the spectrum for such thin films, but its contribution is expected to be very small. On the right is a typical tenorite spectrum taken at 70 eV radiation and the peak positions, by Warren et al.* [60]

predicted by the most advanced calculations.[59,61,62] All calculations predict the peaks to be at lower binding energies than measured here. Compared to most calculations on tenorite the spectrum presented here is shifted up by as much as 2 eV. Compared to experiments performed on tenorite, the spectrum for the tetragonal phase is shifted to higher binding energies by about 0.5 eV. For a film of this thickness a contribution of the substrate to the spectrum is expected and some states present at the Fermi level seem to confirm this. $SrTiO_3$ has two large peaks at higher energies (4.4 and 6.6 eV), but no clear correlation between these peaks and the measured spectrum has been found.

5.2.4 Magnetic properties of tetragonal CuO

In order to determine the magnetic properties of the CuO films the exchange bias effect of CuO films grown on thin $SrRuO_3$ on $SrTiO_3$ was measured. $SrRuO_3$ was chosen because of its close lattice match with $SrTiO_3$ and the ability to single-terminate the surface. $SrRuO_3$ changes its termination on $SrTiO_3$ by first growing 1.5 unit cells of material and subsequently single unit cells. The CuO was found to grow equally well on the A site (Sr) terminated surface. $SrRuO_3$ is by no means the ideal ferromagnet with which to measure an exchange bias effect. As mentioned in section 5.1.3 on page 84, to apply the exchange bias theory it is ideal when cooling the sample in a magnetic field if the Curie temperature is higher than the Néel temperature so that all the spins in the ferromagnet are aligned first along a known direction. The antiferromagnet is then influenced by the ferromagnet when cooling down through the Néel temperature and aligns preferentially. In the case of $SrRuO_3$ the Curie temperature is only 160

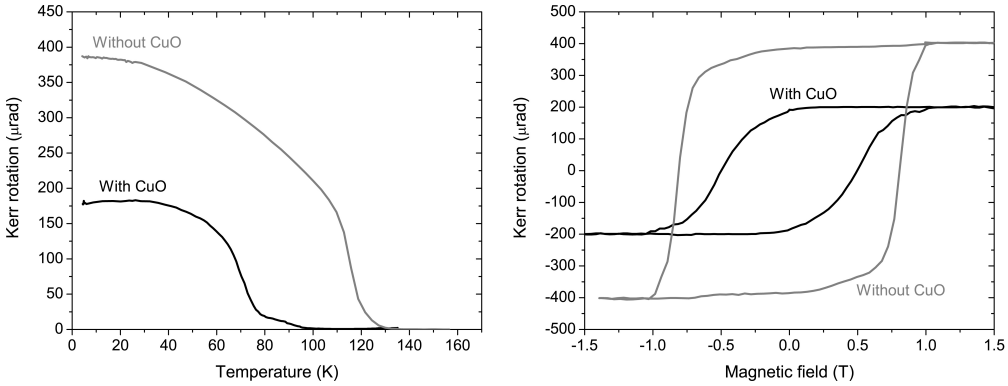

Figure 5.17: *Kerr rotation as a function of temperature on the left for 6.5 ML of $SrRuO_3$ sample, with (black lines) and without (gray lines) 300 pls CuO, which shows a reduction in the magnetic signal after the deposition of CuO. On the right the hysteresis loop taken at 4 K for the same sample. Besides a reduction in Kerr rotation the coercive field is reduced as well for part of the spins, whereas the total coercive field remains more or less the same.*

K, which means the ideal scenario is only valid when the Néel temperature of CuO is below this. If the Néel temperature for the tetragonal phase is close to that of tenorite we would expect, due to the thickness effect, that measuring an exchange bias effect is possible. If the tetragonal phase has a T_N which follows the trend based on the other rock-salt structure transition metal monoxides, as was shown in figure 5.6 on page 85, we would expect T_N to be much higher than 160 K. No straightforward measurement of the exchange bias would be possible even after taking any thickness effect into account.

Due to time restraints, only two samples were measured with the Sagnac setup that was described in section 2.4.2 on page 23. The first had 6.5 ML of $SrRuO_3$ and the second one 9.5 ML. Both of the samples had 300 pls of CuO deposited on them. The results for the 6.5 ML sample are shown in figure 5.17, where on the left side the warm up curves for the sample with and without CuO are given. Two differences are immediately obvious: the maximum Kerr signal is much lower after CuO has been deposited (182 μrad after against 387 μrad before CuO) and the Curie temperature has been reduced as well from 130 K to 96 K. No shift in the hysteresis loop (figure 5.17 right side) and no enhancement in the coercive field are observed either. The opposite is happening, some spins are more easily flipped in the opposite direction, whereas the field that is required to flip all the spins remains unchanged.

An unexpected result was the 9.5 ML sample did not show any ferromagnetic signal after the deposition of CuO and no hysteresis loop was observed, although before deposition it showed a 650 μrad signal at 4 K and a Curie temperature of 128 K.

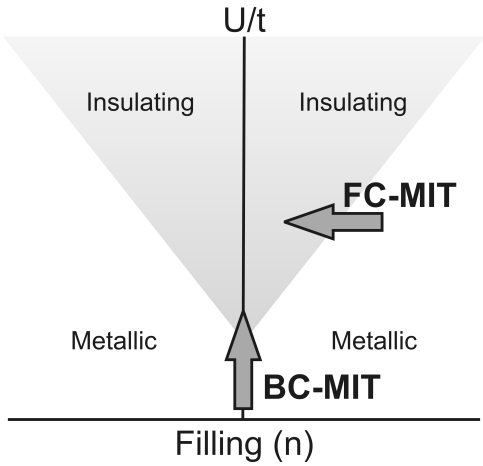

Figure 5.18: *A schematic phase diagram of a Mott insulator, taken from Imada, Fujimori, and Tokura,*[17] *showing a metal-insulator transition can be accomplished by bandwidth control (U/t) or by filling control (n). Note that this diagram is only valid when disorder plays no role.*

5.3 Doping of tetragonal CuO

Doping a Mott insulator restores the electrical conductivity because empty sites are created to which electrons can jump without having to incur a cost in Coulomb energy.

If the filling of the sites or the Coulomb interaction between the sites can be controlled, the transport properties of the material can be changed. The material could be brought from an insulating to a metallic state; this is one form of a Metal-Insulator Transition, or MIT. A model with which to describe such transitions is the Hubbard model.[63,64,65] The two important parameters in the Hubbard model are the electron correlation strength U/t and the band filling n. A schematic metal-insulator phase diagram is given in figure 5.18. The $n = 0$ and $n = 2$ fillings correspond to the band insulator state. At half filling ($n = 1$), represented by the black line in the center of the figure, the transition from the insulating to the metallic state can be driven by changing U/t. This type of transition is called a bandwidth controlled (BC) MIT. To accomplish the transition the electron correlation strength is controlled by modifying the lattice parameters or the chemical composition while essentially maintaining the original lattice structure. The onsite (U) or intersite Coulomb interacting is kept almost unchanged during the above procedure and control of electron correlation is achieved by control of the transfer interaction (t), which is also known as the one-electron bandwidth. The one-electron bandwidth in $3d$ transition metal systems is known to be quite narrow. In the ABO_3 perovskite systems the bandwidth is reduced by the buckling B—O—B bond, since the effective $3d$-electron transfer interaction between the neighboring B sites is governed by the supertransfer process via the O $2p$ state. For CuO the $3d$-electron bandwidth is still narrow, but no buckling will occur

in the rock salt structure. According to Imada, Fujimori, and Tokura[17] there are three methods of bandwidth control:

1. applying pressure to the material;
2. modifying the chemical composition using the solid solution or the mixed-crystal effect, a good example of which is the substitution of S with Se in NiS_2;
3. modifying the ionic radius of the A site in a perovskite-type compound, i.e. ABO_3.

These options are not easily accessible for our materials system, or cause us to cease measuring rock salt CuO. At the same time we need to remember that by using epitaxy to stabilize the structure, we apply significant pressure to the material. This will influence the bandwidth of the material and might make it easier to dope, it is, however, not a parameter we can easily control. Therefore another route for doping might be more appropriate.

A filling at noninteger n usually leads to the metallic phase. The most interesting phase is the one right next to the $n = 1$ insulating line in figure 5.18 on the previous page which is derived by filling control (FC-MIT) of the parent Mott insulator. The standard method for filling control is to replace an atom with a high valence, with one with a lower valence, or vice versa. A good example is the high-T_c compound $La_{2-x}Sr_xCuO_4$ compound where the trivalent La atoms are replaced with divalent Sr atoms. Using the insulating compound as a reference, the filling is called *hole doping* when the band filling is decreased and *electron* doping when the band filling is increased. Replacing La with Sr in $La_{2-x}Sr_xCuO_4$ is an example of hole doping. Chemical substitution is one way to accomplish different filling, but this can also be done by injecting or depleting charge carriers with an electric field or by using some kind of modulation doping.

Comparing to doping experiments in tenorite could provide good insight on where to start. However, there are few references in literature on the doping of tenorite. The most interesting experiments are those where tenorite is doped by substituting Li for Cu.[45,66] This substitution would result in hole doping, if the oxygen stoichiometry does not change. Those authors find Li only substitutes Cu up to 1.7%. With increased doping the Cu—Cu bond length is increased and the magnetic ordering temperature is decreased due to the weakening of the superexchange coupling along the $(10\bar{1})$. direction. In other related work[67] they show there is evidence for static charge ordering and alignment of charge ordered domains in CuO analogous to the charge stripes in cuprate superconductors. The fact that a simple compound like CuO shows the same electronic behavior as the high temperature superconductors is promising for doping experiments.

5.3.1 Chemical doping through charge transfer

Without breaking vacuum, alkali metals were deposited on top of the tetragonal CuO films in an attempt to transfer charge carriers into the material. The sources used are described in section 2.2.4 on page 11. Alkali metals were chosen because their outer electrons are very loosely bound and these can be transferred into the CuO. This

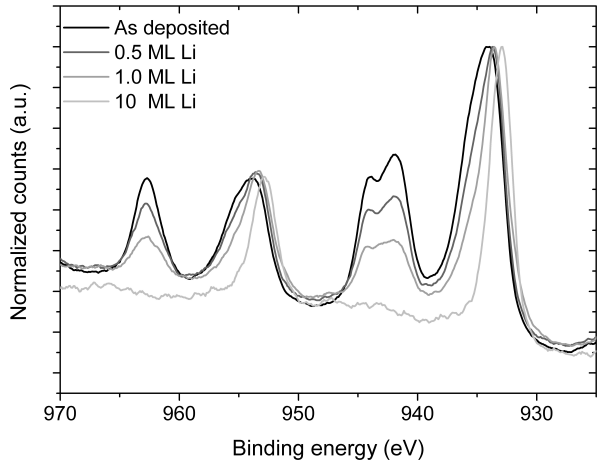

Figure 5.19: *XPS Cu 2p spectrum of an as-deposited tetragonal CuO film and spectra taken after deposition of 0.5, 1.0, and 10 MLs of Li. The spectrum changes systematically towards a Cu^{1+} spectrum, which suggests charge carriers are created.*

property also makes them very reactive and that likely prevents us from analyzing the samples outside of vacuum conditions. Of course, even if charge is transferred the question remains whether the charges will be mobile or localized.

The first alkali metal used was lithium, the lightest of the alkali metals. Deposition was incremental and after each deposition photoemission spectra were taken. Valence band spectra were taken with UPS to see whether the sample was a conductor and core level spectra were taken to monitor the change in chemical environment. In figure 5.19 the Cu $2p$ spectrum is shown as Li is being deposited. After half a monolayer of Li the spectrum changes considerably. The satellite peaks diminish in intensity whereas the main peaks gain. The spectral shift can be explained by doping of the Li electrons into the CuO: in a localized picture this would generate more Cu^{1+} at the expense of Cu^{2+} and make the spectrum look more like Cu_2O. On the other hand a similar effect would be expected to occur if Li removed oxygen from the CuO, which also creates more Cu^{1+}. In both cases the CuO would be electron doped, but UPS measurements showed no Fermi edge, charging was observed during XPS measurements, and when the samples were removed from the system no conductivity was measured. The RHEED spectra for the films with 0.5 and 1.0 ML of Li showed no change with respect to the as-deposited sample, whereas after 10 ML of Li the RHEED spectrum showed a disordered surface as one would expect from an amorphous layer of Li.

The Li was not easy to detect with XPS, which made it hard to verify how much had been deposited. To be better able to detect the deposited amount Li was switched for Cs. Cs has a much higher sensitivity factor for XPS and turned out to be much easier to detect. The Cu $2p$ spectra for the Cs deposition are shown in figure 5.20 on the following page and the systematic change in the spectra is similar to the sample with Li as a dopant. The O $1s$ peak does not change significantly when Cs is deposited.

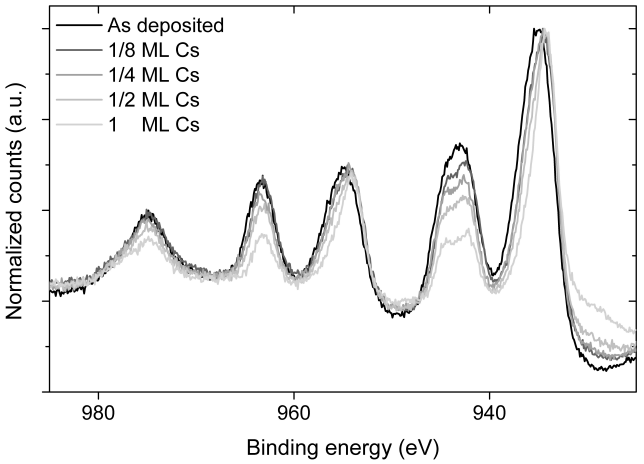

Figure 5.20: *XPS Cu 2p spectrum of an as-deposited tetragonal CuO film and spectra taken after deposition of approximately $\frac{1}{8}$, $\frac{1}{4}$, $\frac{1}{2}$, and 1 MLs of Cs. The spectrum changes systematically towards a Cu^{1+} spectrum, which suggests charge carriers are created.*

The Cs peaks themselves are lower than one would expect for elemental Cs by about 1 eV. CsOH is 1.4 eV lower than Cs metal and the lower binding energy therefore suggests that Cs has donated an electron. For this sample neither a Fermi edge, for any quantity of Cs, nor conductivity outside of vacuum, after 1 ML was deposited (which is most likely overdoping), were observed.

5.4 Discussion and conclusions

We have grown CuO with a higher degree of symmetry by using epitaxial stabilization on a $SrTiO_3$ substrate. The in-plane lattice parameters were determined by RHEED. After taking forbidden reflections into account the CuO was found to grow cube-on-cube on the $SrTiO_3$, which results in an in-plane lattice parameter of 3.905 Å for CuO. The out-of-plane lattice parameter was measured with XPD and decided to be about 5.3 Å after comparing to simulated data. On dual terminated substrates the growth yielded a mixture of tetragonal and monoclinic CuO. The unit cell on $SrTiO_3$ is highly strained and for this reason the tetragonal CuO cannot grow coherently for more than a few nm. Using substrates with larger in-plane lattice parameters, such as $DyScO_3$ and $GdScO_3$, might be able to help relax the strain and stabilize the tetragonal structure for larger thicknesses, while at the same time influence the electron bandwidth. At the moment though there is no reliable method to single-terminate these substrates, resulting in a mixed phase growth of the CuO.

The electronic structure of the tetragonal phase of CuO was found to differ from the monoclinic phase by examining the Cu $2p$ core level structure. The main peak becomes broader and the satellite peak sharper when the tetragonal phase is formed.

The intensity distribution in the satellite peak shifts more to lower binding energies. According to Van Veenendaal and Sawatsky,[34,35] the width of the main peak is related to whether the screening electrons come from the closest ligand atoms or from ligand atoms further away. This would suggest that the screening electrons are more delocalized in the tetragonal structure. Note that while the shortest Cu–O bond lengths in the tetragonal structure are similar to those in tenorite, there are also much longer bond lengths in the tetragonal structure, which might have an influence on the nature of the electrons. The structure of the satellite peak is harder to understand. The similarity with $CuCl_2$ spectra from literature is striking though.[32] Okada *et al.*[36] have performed extensive modeling of the satellite peak. They argue that the shape of the satellite peak is mostly determined by the coupling-strength ratio between the σ and π bondings and the amount of hybridization of these states. Following their model suggests that the degree of hybridization is weaker in the tetragonal structure than in tenorite. In other words, the ionicity is stronger in the tetragonal structure.

The tetragonal structure is more stable close to the interface as is evident from angle dependent measurements. For the best samples exposure to air does not degrade the quality of the film at the interface. The tetragonal CuO is not stable under vacuum conditions over long periods of time resulting in a reduction of the films, an effect observed previously on tenorite.[24]

The UPS spectrum of tetragonal CuO is very similar to that measured for tenorite. Some notable differences include the intensity of the low energy peak, the splitting of the main peak, and a general shift of the spectrum to higher binding energies of about half an eV. Delocalized band calculations (local density approximation) performed for tenorite do not reproduce measurements. Neglecting electron correlation effects results in an incomplete DOS spectrum and a conducting ground state. The best predictions come from cluster calculations (configuration interaction (CI) calculations), which predict the entire spectrum accurately, but shifted to slightly lower binding energy. Eskes *et al.*[62] have investigated the nature of the first ionization state of CuO, which has either a triplet or a singlet character. The singlet state peak is the one closest to the Fermi level (1.9 eV in our spectrum) and the triplet state is the next one up (3.6 eV for this work). The energy difference between these peaks is closely related to the Cu–O distances, specifically the ratio between the Cu–O distance out-of-plane and in-plane, which is about 1.4 for the tetragonal unit cell. Based on their model we would expect to see an energy difference of 0.85 eV between the two peaks. The measured distance is much larger for reasons that are not well understood.

The magnetic properties were studied by measuring the exchange bias effect on a very limited number of samples with an interface of CuO and $SrRuO_3$. Instead of increased coercivity and a shifted hysteresis loop, we observed a decrease in coercivity for part of the spins, no shift in the hysteresis loop, and a reduction in Kerr signal in general after deposition of the CuO. Thus far, no explanation has been found for these behaviors and more samples should be measured before any conclusions can be drawn.

We have attempted to dope the CuO by depositing alkali metals on top, which might donate an electron to the CuO. Li and Cs were tried and showed similar results. In both cases the Cu $2p$ XPS spectrum changed from Cu^{2+} to Cu^{1+}, suggesting either a direct doping of electrons by the alkali metal or oxygen reduction in the CuO due to

the metal. In both cases the CuO would be electron doped.

Bibliography

1. E. V. Parini, V. G. Tsirel'son, and R. P. Ozerov, Soviet Physics Crystallography **33**, 175 (1988).
2. A. Kirfel and K. Eichhorn, Acta Crystallographica A **46**, 271 (1990).
3. S. Åsbrink and L.-J. Norrby, Acta Crystallographica Section B **26**, 8 (1970).
4. N. Datta and J. W. Jeffery, Acta Crystallographica B **34**, 22 (1978).
5. M. O'Keeffe and J.-O. Bovin, American Mineralogist **63**, 180 (1978).
6. P. E. D. Morgan, D. E. Partin, B. L. Chamberland, and M. O'Keeffe, Journal of Solid State Chemistry **121**, 33 (1996).
7. J. R. Schrieffer and J. S. Brooks, eds., *Handbook of High Temperature Superconductivity: Theory and Experiment* (Springer, 2007).
8. F. A. Cotton and G. Wilkinson, *Advanced Inorganic Chemistry* (Wiley Interscience, 1988), 5th ed.
9. J. F. Pierson, A. Thobor-Keck, and A. Billard, Applied Surface Science **210**, 359 (2003).
10. L. Kleinman and K. Mednick, Physical Review B **21**, 1549 (1980).
11. J. Robertson, Physical Review B **28**, 3378 (1983).
12. E. Ruiz, S. Alvarez, P. Alemany, and R. A. Evarestov, Physical Review B **56**, 7189 (1997).
13. Y. L. Liu, Y. C. Liu, R. Mu, H. Yang, C. L. Shao, J. Y. Zhang, Y. M. Lu, D. Z. Shen, and X. W. Fan, Semiconductor Science and Technology **20**, 44 (2005).
14. Z. Szotek, W. M. Temmerman, and H. Winter, Physical Review B **47**, 4029 (1993).
15. F. Marabelli, G. B. Parravicini, and F. Salghetti-Drioli, Physical Review B **52**, 1433 (1995).
16. F. P. Koffyberg and F. A. Benko, Journal of Applied Physics **53**, 1173 (1982).
17. M. Imada, A. Fujimori, and Y. Tokura, Reviews of Modern Physics **70**, 1039 (1998).
18. J. Zaanen, G. A. Sawatzky, and J. W. Allen, Physical Review Letters **55**, 418 (1985).
19. N. Ashcroft and N. Mermin, *Solid State Physics* (Harcourt, 1976).
20. N. F. Mott, Proceedings of the Royal Society of London Series A **62**, 416 (1949).
21. J. Orenstein and A. Millis, Science **288**, 468 (2000).
22. S. Huefner, Solid State Communications **49**, 1177 (1984).

23. J. Ghijsen, L. H. Tjeng, J. van Elp, H. Eskes, J. Westerink, G. A. Sawatzky, and M. T. Czyzyk, Physical Review B **38**, 11322 (1988).

24. Z.-X. Shen, R. S. List, D. S. Dessau, F. Parmigiani, A. J. Arko, R. Bartlett, B. O. Wells, I. Lindau, and W. E. Spicer, Physical Review B **42**, 8081 (1990).

25. K. Hirokawa, F. Honda, and M. Oku, Journal of Electron Spectroscopy and Related Phenomena **6**, 333 (1975).

26. J. C. Fuggle and N. Mårtensson, Journal of Electron Spectroscopy and Related Phenomena **21**, 275 (1980).

27. N. Nücker, J. Fink, B. Renker, D. Ewert, C. Politis, P. J. W. Weijs, and J. C. Fuggle, Zeitschrift für Physik B **67**, 9 (1987).

28. N. S. McIntyre and M. G. Cook, Analytical Chemistry **47**, 2208 (1975).

29. T. H. Fleisch, G. W. Zajac, J. O. Schreiner, and G. J. Mains, Applied Surface Science **26**, 488 (1986).

30. T. Robert, M. Bartel, and G. Offergeld, Surface Science **33**, 123 (1972).

31. E. Antonides, E. C. Janse, and G. A. Sawatzky, Physical Review B **15**, 1669 (1977).

32. G. van der Laan, C. Westra, C. Haas, and G. A. Sawatzky, Physical Review B **23**, 4369 (1981).

33. S. Hüfner, G. K. Wertheim, and J. H. Wernick, Solid State Communications **17**, 417 (1975).

34. M. A. van Veenendaal and G. A. Sawatzky, Physical Review Letters **70**, 2459 (1993).

35. M. A. van Veenendaal, H. Eskes, and G. A. Sawatzky, Physical Review B **47**, 11462 (1993).

36. K. Okada and A. Kotani, Journal of the Physical Society of Japan **58**, 2578 (1989).

37. T. Saitoh, A. E. Bocquet, T. Mizokawa, and A. Fujimori, Physical Review B **52**, 7934 (1995).

38. P. W. Anderson, Physical Review **115**, 2 (1959).

39. W. A. Harrison, Physical Review B **76**, 054417 (2007).

40. D. Alders, L. H. Tjeng, F. C. Voogt, T. Hibma, G. A. Sawatzky, C. T. Chen, J. Vogel, M. Sacchi, and S. Iacobucci, Physical Review B **57**, 11623 (1998).

41. J. A. Borchers, M. J. Carey, R. W. Erwin, C. F. Majkrzak, and A. E. Berkowitz, Physical Review Letters **70**, 1878 (1993).

42. R. W. Wang and D. L. Mills, Physical Review B **46**, 11681 (1992).

43. T. Ambrose and C. L. Chien, Physical Review Letters **76**, 1743 (1996).

44. A. S. Carriço and R. E. Camley, Physical Review B **45**, 13117 (1992).

45. K. Saito, S. Ikeuchi, Y. Nakazawa, X. G. Zheng, M. B. Maple, and M. Sorai, Solid State Communications **125**, 23 (2003).

46. W. L. Roth, Physical Review **111**, 772 (1958).

47. J. Stöhr, A. Scholl, T. J. Regan, S. Anders, J. Lüning, M. R. Scheinfein, H. A. Padmore, and R. L. White, Physical Review Letters **83**, 1862 (1999).

48. W. H. Meiklejohn and C. P. Bean, Physical Review **102**, 1413 (1956).

49. R. L. Stamps, Journal of Physics D: Applied Physics **33**, R247 (2000).

50. A. Scholl, J. Stöhr, J. Lüning, J.-P. Locquet, J. Fompeyrine, J. W. Seo, H. Siegwart, F. Nolting, S. Anders, E. Fullerton, et al., Science **287**, 1014 (2000).

51. J. van Driel, F. R. de Boer, K.-M. H. Lenssen, and R. Coehoorn, Journal of Applied Physics **88**, 975 (2000).

52. H. Xi and R. M. White, Physical Review B **61**, 80 (2000).

53. F. Nolting, A. Scholl, J. Stohr, J. Seo, J. Fompeyrine, H. Siegwart, J.-P. Locquet, S. Anders, J. Luning, E. Fullerton, et al., Nature **405**, 767 (2000).

54. D. Mauri, H. C. Siegmann, P. S. Bagus, and E. Kay, Journal of Applied Physics **62**, 3047 (1987).

55. X. Y. Lang, W. T. Zheng, and Q. Jiang, Nanotechnology **18**, 155701 (2007).

56. F. J. García de Abajo, M. A. Van Hove, and C. S. Fadley, Physical Review B **63**, 075404 (2001).

57. C. J. Powell and A. Jablonski, *NIST Electron Inelastic-Mean-Free-Path Database* (National Institute of Standards and Technology, Gaithersburg, MD, 2000), 1st ed.

58. W. Y. Ching, Y.-N. Xu, and K. W. Wong, Physical Review B **40**, 7684 (1989).

59. J. Ghijsen, L. H. Tjeng, H. Eskes, G. A. Sawatzky, and R. L. Johnson, Physical Review B **42**, 2268 (1990).

60. S. Warren, W. R. Flavell, A. G. Thomas, J. Hollingworth, P. L. Wincott, A. F. Prime, S. Downes, and C. Chen, Journal of Physics: Condensed Matter **11**, 5021 (1999).

61. M. Takahashi and J.-I. Igarashi, Physical Review B **56**, 12818 (1997).

62. H. Eskes, L. H. Tjeng, and G. A. Sawatzky, Physical Review B **41**, 288 (1990).

63. J. Hubbard, Proceedings of the Royal Society of London Series A **276**, 238 (1963).

64. J. Hubbard, Proceedings of the Royal Society of London Series A **277**, 237 (1964).

65. J. Hubbard, Proceedings of the Royal Society of London Series A **281**, 401 (1964).

66. X. G. Zheng, H. Yamada, D. J. Scanderbeg, M. B. Maple, and C. N. Xu, Physical Review B **67**, 214516 (2003).

67. X. G. Zheng, C. N. Xu, E. Tanaka, Y. Tomokiyo, H. Yamada, Y. Soejima, Y. Yamamura, and T. Tsuji, Journal of the Physical Society of Japan **70**, 1054 (2001).